Spring 5-13-2016

A Numerical Study of Compressible Lid Driven Cavity Flow with a Moving Boundary

Amer Hussain
UNIVERSITY OF NEW ORLEANS, ahussai1@uno.edu

A Numerical Study of Compressible Lid Driven Cavity Flow with a Moving Boundary

A Thesis

Submitted to the Graduate Faculty of the
University of New Orleans
in partial fulfillment of the
requirements for the degree of

Master of Science
in
Engineering
Mechanical

by

Amer Hussain

B.Tech., Jawaharlal Nehru Technological University, 2014

May, 2016

DEDICATION

To

My Parents

who brought me in this world and taught me never to lose hope and always try to the end without expecting anything for earning an honest living

and

My Brother

who always encourages me to listen to my mind to do things as I think is good and always keeps faith in me

ACKNOWLEDGMENT

First of all, I would like to express my sincere gratitude to my advisor, Dr. Kazim M Akyuzlu for the continuous support of my Master's study and research, for his patience, motivation, enthusiasm, and immense knowledge. I am thankful for his guidance on fostering my professional problem-analyzing, problem-solving, and reporting skills. His advice helped me a lot to complete this work.

Besides my advisor, I would like to thank the rest of my thesis committee; Dr. Ting Wang and Dr. Martin J Guillot for their encouragement and insightful comments.

I thank my fellow lab mates M Shafiqur Rahman, Anvesh Nallaballi, Mine Kaya, Jose E. Rubio, Seda Aslan, and Pratik Sarker at the University of New Orleans for the stimulating discussions, sleepless nights we worked together before deadlines, and for all the fun we have had in the last two years.

Last but not the least, I would like to thank my family, my father Hussain Rafi Ullah and my mother Shameem Akhtar for bringing forth me in this world and supporting me unanimously throughout my life.

ABSTRACT

A two-dimensional (2-D), mathematical model is adopted to investigate the development of circulation patterns for compressible, laminar, and shear driven flow inside a rectangular cavity. The bottom of the cavity is free to move at a specified speed and the aspect ratio of the cavity is changed from 1.0 to 1.5. The vertical sides and the bottom of the cavity are assumed insulated. The cavity is filled with a compressible fluid with Prandtl number, $Pr = 1$. The governing equations are solved numerically using the commercial Computational Fluid Dynamics (CFD) package ANSYS FLUENT 2015 and compared with the results for the primitive variables of the problem obtained using in house CFD code based on Coupled Modified Strongly Implicit Procedure (CMSIP). The simulations are carried out for the unsteady, lid driven cavity flow problem with moving boundary (bottom) for different Reynolds number, Mach numbers, bottom velocities and high initial pressure and temperature.

Keywords: Lid Driven Cavity Flow, Compressible, Unsteady, Laminar, CFD models, Moving Boundaries, Adiabatic.

Table of Contents

NOMENCLATURE

Symbols

AR	Aspect Ratio, H/L
c_p	Specific Heat
H	Height of the cavity
k	Thermal conductivity
L	Width of the cavity
M	Mach number
Pr	Prandtl number
p	Pressure
R	Gas Constant
Re	Reynolds number
T	Temperature
t	Time
u	Velocity in x direction
v	Velocity in y direction
x	Horizontal distance
y	Vertical distance

Greek Symbols

γ	Isentropic constant
μ	Viscosity
ρ	Density
ϕ	Viscous dissipation
ξ	Transformed x coordinate
σ	Transformed y coordinate

Superscripts

ref	Reference

List of Figures

List of Table

1. Introduction

Lid Driven cavity flow has been used extensively in the past as a benchmark case for the study of computational methods to solve Navier-Stokes equations. In this problem the side and bottom walls (boundaries) surrounding the cavity are fixed but the upper surface (lid) of the cavity is moved at a uniform velocity. Many investigators [1-8] have solved this problem assuming an incompressible fluid at low Mach numbers inside a cavity. This incompressible flow version of the driven cavity problem seems to be the benchmark case which is widely used by other investigators who study compressible flow inside cavities or channels. Some researchers [9] have used this classical problem to benchmark their solutions to unsteady compressible Navier-Stokes equations for low and high Mach number laminar flows. (Experimental data is also available for this problem. See references [10-12].)

Other benchmarking cases include flow in a channel, flow though an expansion, and external flows over various types of solid surfaces. All of these cases, including the driven cavity problem, represent examples of fixed boundary problems where steady state solutions to incompressible (and compressible) Navier-Stokes equations are of concern. No attempt has been made yet to establish a benchmark case to study various solution techniques for moving boundary problems.

So far there is no available benchmarking solutions to unsteady, compressible Navier-Stokes equations where the flow domain is not enclosed by fixed boundaries. An example of such type of problems is the case of natural convection inside the ullage of a cryogenic storage tank where the ullage volume increases with the discharge of the liquid propellant [13]. Another example of moving boundary problems is the flow of combustion gases inside the combustion chamber of a hybrid rocket motor where the chamber boundaries move (enlarge) with the continuous ablation of the solid fuel surface [14]. Both of these problems require the solution of the unsteady, compressible Navier-Stokes equations and the coupled energy equation to predict, accurately, the velocity field as well as the temperature and pressure distributions inside the flow domain.

An attempt has been made to simulate a lid driven cavity flow at aspect ratio 1.0 with a moving boundary using Coupled Modified Strongly implicit Method (CMSIP) by Akyuzlu *et. al* [15], where the bottom of the cavity is assumed to move at a constant speed until the aspect ratio of 1.5 is reached.

Here a commercial CFD package ANSYS FLUENT is used to simulate the similar case [15] and compare the results, to illustrate the accuracy of the simulation for better characterizations of the primitive variables.

2. Literature Survey

Assuming incompressible flow inside the cavity, numerous investigations have been done [1−7] with low *M* and variable *Re* values to solve the problem. This study of incompressible flow has been the benchmark for years with widespread applications for the researchers including the study of channel flows, cavity flows, low and high Mach number laminar compressible flows [8−10]. Ghia *et al*. used the vorticity-stream function formulation of the two-dimensional incompressible Navier- Stokes equations to study the effectiveness of the coupled strongly implicit multigrid (CSI-MG) method in the determination of high-*Re* fine-mesh flow solutions. This work has been considered as a benchmark research to be studied by many fellow researchers in the last few decades [2−8].

Chen and Pletcher [9] used the classical problem to benchmark their solutions to unsteady compressible Navier-Stokes equations for low and high Mach number laminar flows. Other benchmarking cases include flow in a channel, flow through an expansion, and external flows over various types of solid surfaces. All of these cases, including the driven cavity problem, represent examples of fixed boundary problems where steady state solutions to incompressible (and compressible) Navier-Stokes equations are of concern. There is a need for benchmarking solutions to unsteady, compressible Navier-Stokes equations where the flow domain is not enclosed by fixed boundaries. An example of such type of problems is the case of natural convection inside the ullage of a cryogenic storage tank where the ullage volume increases with the discharge of the liquid propellant [13]. Another example of moving boundary problems is the flow of combustion gases inside the combustion chamber of a hybrid rocket motor where the chamber boundaries move (enlarge) with the continuous ablation of the solid fuel surface [14]. Both of these problems require the solution of the unsteady, compressible Navier-Stokes equations and the coupled energy equation to predict, accurately, the velocity field as well as the temperature and pressure distributions inside the flow domain.

A study with moving bottom boundary for compressible flow has also been conducted by Akyuzlu *et al*, [11] where the change of aspect ratio of the driven cavity due to the moving bottom wall has been analyzed. In that study, the set of algebraic equations corresponding to the problem have been solved by using the Coupled Modified Strongly Implicit Procedure (CMSIP) for the unknown primitive variables. Again, other mentionable attempts relating to this field are the numerical study of natural convection of compressible fluid inside an enclosed cavity [12], study of unsteady cavity flow using PIV [13] and so on.

3. Description of The Physical Model

In the present study, a square cavity of aspect ratio 1.0 filled with compressible fluid at Pr = 1.0 is used as working fluid at standard temperature and pressure (STP). The top, left, right, and bottom walls of the cavity are considered to be adiabatic walls with no slip condition. Initially, everything is stationary inside the square cavity. The flow becomes steady at time (t_1), then the bottom boundary is moved with a constant velocity (v_b) in negative y direction which stops at time (t_2) when the square cavity reaches the aspect ratio of 1.5 and becomes steady again at time (t_3). Evaluating the values M and Re, the flow inside the cavity can be categorized as laminar and subsonic. The physical model of the square cavity is shown in Figure 1.

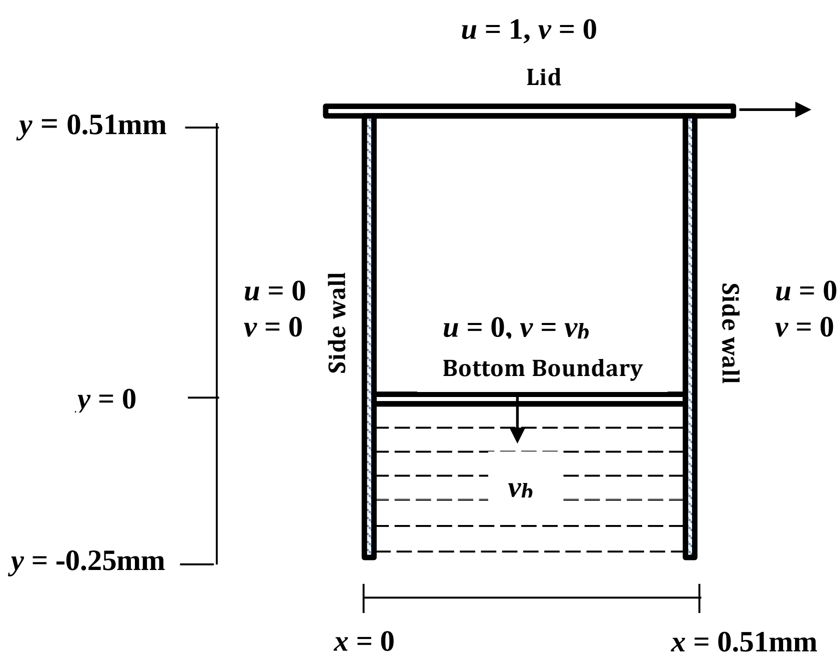

Figure 1 – Schematic of a square cavity with a moving bottom

No slip boundary conditions are assumed on the walls of the cavity and also considered to be impermeable. There is no heat transfer through the walls since they are adiabatic. With constant temperature (T), pressure (P), density (ρ) of the fluid is calculated at each time interval as the bottom wall moves from time t_1 to t_2.

4. Description of a Mathematical Model

The mathematical formulation of the driven cavity including the conservation equations together with the initial and boundary conditions in second order accurate in time models is given in this chapter. The dimensional governing equations used is derived from the respective vector form of continuity, momentum, and energy equations (refer to Appendix I). The initial and boundary conditions are then applied to well pose the mathematical formulation.

4.1 2-D Mathematical Model (FLUENT)

4.1.1 Assumption of 2-D Mathematical Model

The following assumptions were made for the present study.

1. The physical domain is Two-dimensional and the equations are in Cartesian Coordinates.
2. The working fluid forms a continuum.
3. The flow is subsonic, unsteady, laminar, and viscous.
4. The working fluid is compressible with $Pr = 1$ (the density of the fluid is a function of temperature and pressure) and can be treated as an ideal gas.
5. The working fluid behaves like a Newtonian fluid with stokes assumptions.
6. The kinetic and potential energy terms in the energy equations are very small and can be neglected except viscous dissipation term.
7. Radiation heat transfer is ignored.
8. There are no internal heat sources.
9. The physical and transport properties of the fluid are assumed to be constant
10. No effect of gravity is assumed on the enclosed fluid

4.1.2 Mathematical Formulation for 2-D Model

i. Governing Differential Equations

The conservation equations for 2-D, unsteady, viscous, compressible, subsonic, and laminar flow can be written in terms of primitive variables *ρ, u, T*, and *P* as follows:

For 2-D Cartesian, unsteady, compressible fluid, the conservative form of these equations are given as follows:

The continuity equation is given by:

$$\frac{\partial \rho}{\partial t} + \frac{\partial}{\partial x}(\rho u) + \frac{\partial}{\partial y}(\rho v) = 0 \tag{4.1}$$

The momentum equation in the *x*-direction is given by:

$$\frac{\partial}{\partial t}(\rho u) + \frac{\partial}{\partial x}(\rho u^2) + \frac{\partial}{\partial y}(\rho uv) = -\frac{\partial p}{\partial x} + \frac{\partial}{\partial x}\left[\frac{2}{3}\mu\ (2\frac{\partial u}{\partial x} - \frac{\partial v}{\partial y})\right] + \frac{\partial}{\partial y}\left[\mu\ (\frac{\partial u}{\partial y} + \frac{\partial v}{\partial x})\right] \tag{4.2}$$

The momentum equation in the *y*-direction (normal to fuel surface) is given by:

$$\frac{\partial}{\partial t}(\rho v) + \frac{\partial}{\partial x}(\rho uv) + \frac{\partial}{\partial y}(\rho v^2) + \frac{\partial p}{\partial y} = -\frac{\partial p}{\partial y} + \frac{\partial}{\partial x}\left[\mu\ (\frac{\partial u}{\partial y} + \frac{\partial v}{\partial x})\right] + \frac{\partial}{\partial y}\left[\frac{2}{3}\mu\ (2\frac{\partial v}{\partial y} - \frac{\partial u}{\partial x})\right] \tag{4.3}$$

The energy equation is given by:

$$\frac{\partial}{\partial t}\left[(c_p - R)\rho T\right] + \frac{\partial}{\partial x}(c_p \rho u T) + \frac{\partial}{\partial y}(c_p \rho v T) = \frac{\partial}{\partial x}(k\frac{\partial T}{\partial x}) - \frac{\partial}{\partial y}(k\ \frac{\partial T}{\partial y}) + \mu[2(\frac{\partial u}{\partial x})^2 + 2(\frac{\partial v}{\partial x})^2 + (\frac{\partial v}{\partial x} + \frac{\partial u}{\partial y})^2 - \frac{2}{3}(\frac{\partial u}{\partial x} + \frac{\partial v}{\partial y})^2] \tag{4.4}$$

The equation of state is given by

$$p = \rho R T \tag{4.5}$$

ii. Initial Conditions

$$u = 0, \quad v = 0, \quad at \quad t = 0 \quad and \quad 0 \le x \le 1, \quad 0 \le y \le 1$$

$$\left.\begin{aligned} T_i &= T_o, \\ \rho_i &= \rho_o \\ P_i &= P_o \end{aligned}\right\} at \quad t = 0 \quad and \quad 0 \le x \le 1, \quad 0 \le y \le 1$$

iii. Boundary conditions

$$u = 0, \quad v = 0, \quad \frac{\partial T}{\partial y} = 0 \quad at \quad y = 0 \quad and \quad 0 \le x \le 1 \quad for \quad t > 0$$

$$u = 1, \quad v = 0, \quad \frac{\partial T}{\partial y} = 0 \quad at \quad y = 1 \quad and \quad 0 \le x \le 1 \quad for \quad t > 0$$

$$u = 0, \quad v = 0, \quad \frac{\partial T}{\partial \overline{x}} = 0 \quad at \quad x = 0 \quad and \quad 0 \le y \le 1 \quad for \quad t > 0$$

$$u = 0, \quad v = 0, \quad \frac{\partial T}{\partial x} = 0 \quad at \quad x = 1 \quad and \quad 0 \le y \le 1 \quad for \quad t > 0$$

Therefore, the governing equations are Non-Linear, second order and coupled.

4.2 2-D Mathematical model (CMSIP)

4.2.1 Assumption of 2-D Mathematical Model

The following assumptions were made for this mathematical model.

1. The physical domain is Two-dimensional and the equations are in Cartesian Coordinates.
2. The working fluid forms a continuum.
3. The flow is subsonic, unsteady, laminar, and viscous.

4. The working fluid is compressible with Pr = 1 (the density of the fluid is a function of temperature and pressure) and can be treated as an ideal gas.
5. The working fluid behaves like a Newtonian fluid with stokes assumptions.
6. The kinetic and potential energy changes of the fluid, viscous dissipation, and the work done by the pressure changes are small. (The terms representing these changes are ignored in the energy equation.) These assumptions are valid for low Mach number flows ($M< 0.1$).
7. There are no internal heat sources.
8. The physical and transport properties of the fluid are assumed to be constant
9. No effect of gravity is assumed on the enclosed fluid.

4.2.2 Mathematical Formulation for 2-D Model

i. Governing Differential Equations

The non-dimensional conservation equations for a two-dimensional, unsteady, viscous, compressible flow for low Mach numbers can be written in terms of non-dimensional form of the primitive variables $\bar{u}$, $\bar{v}$, $\bar{p}$ and $\bar{T}$ by replacing density by pressure and temperature using the equation of state ($\rho = p/RT$) for ideal gases as follows:

The continuity equation is given by:

$$\frac{\partial}{\partial \bar{t}}\left(\frac{\bar{p}}{\bar{T}}\right)+\frac{\partial}{\partial \bar{x}}\left(\frac{\bar{p}\bar{u}}{\bar{T}}\right)+\frac{\partial}{\partial \bar{y}}\left(\frac{\bar{p}\bar{v}}{\bar{T}}\right)=0 \tag{4.6}$$

The momentum equation in the x-direction is given by:

$$\frac{\partial}{\partial \bar{t}}\left(\frac{\bar{p}\bar{u}}{\bar{T}}\right)+\frac{\partial}{\partial \bar{x}}\left(\frac{\bar{p}\bar{u}^2}{\bar{T}}\right)+\frac{\partial}{\partial \bar{y}}\left(\frac{\bar{p}\bar{u}\bar{v}}{\bar{T}}\right)+\frac{\partial}{\partial \bar{x}}\left(\bar{R}\bar{p}\right)-\frac{\bar{R}\bar{\mu}}{Re}\frac{\partial}{\partial \bar{x}}\left[\frac{2}{3}\left(2\frac{\partial \bar{u}}{\partial \bar{x}}-\frac{\partial \bar{v}}{\partial \bar{y}}\right)\right]-\frac{\bar{R}\bar{\mu}}{Re}\frac{\partial}{\partial \bar{y}}\left[\left(\frac{\partial \bar{u}}{\partial \bar{y}}+\frac{\partial \bar{v}}{\partial \bar{x}}\right)\right]=0 \tag{4.7}$$

The momentum equation in the *y*-direction is given by:

$$\frac{\partial}{\partial \bar{t}}\left(\frac{\bar{p}\bar{v}}{\bar{T}}\right)+\frac{\partial}{\partial \bar{x}}\left(\frac{\bar{p}\bar{u}\bar{v}}{\bar{T}}\right)+\frac{\partial}{\partial \bar{y}}\left(\frac{\bar{p}\bar{v}^2}{\bar{T}}\right)+\frac{\partial}{\partial \bar{y}}\left(\bar{R}\bar{p}\right)-\frac{\bar{R}\bar{\mu}}{Re}\frac{\partial}{\partial \bar{x}}\left[\left(\frac{\partial \bar{u}}{\partial \bar{y}}+\frac{\partial \bar{v}}{\partial \bar{x}}\right)\right]-\frac{\bar{R}\bar{\mu}}{Re}\frac{\partial}{\partial \bar{y}}\left[\frac{2}{3}\left(2\frac{\partial \bar{u}}{\partial \bar{x}}-\frac{\partial \bar{v}}{\partial \bar{y}}\right)\right]=0$$

(4.8)

The energy equation is given by:

$$\frac{\partial}{\partial \bar{t}}\left[\bar{p}\left(\bar{C}_p-\bar{R}\right)\right]+\frac{\partial}{\partial \bar{x}}\left(\bar{p}\bar{u}\bar{c}_p\right)+\frac{\partial}{\partial \bar{y}}\left(\bar{p}\bar{v}\bar{c}_p\right)-\frac{\bar{R}\bar{c}_p\bar{\mu}}{Re\,Pr}\frac{\partial}{\partial \bar{x}}\left(\frac{\partial \bar{T}}{\partial \bar{x}}\right)-\frac{\bar{R}\bar{c}_p\bar{\mu}}{Re\,Pr}\frac{\partial}{\partial \bar{y}}\left(\frac{\partial \bar{T}}{\partial \bar{y}}\right)=0 \quad (4.9)$$

ii. Initial conditions

The governing equations of the present problem are solved for the initial conditions at which the fluid inside the cavity is assumed stagnant and isothermal (at atmospheric conditions). The initial pressure distribution inside the cavity is determined from solution of the hydrostatic equation.

iii. Boundary conditions

The mathematical formulation is closed by the following boundary conditions for time t > 0:

$$\bar{u}=0,\quad \bar{v}=0,\quad \frac{\partial \bar{T}}{\partial \bar{y}}=0 \quad at \quad \bar{y}=0 \quad and \quad 0\le \bar{x}\le 1$$

$$\bar{u}=1,\quad \bar{v}=0,\quad \frac{\partial \bar{T}}{\partial \bar{y}}=0 \quad at \quad \bar{y}=1 \quad and \quad 0\le \bar{x}\le 1$$

$$\bar{u}=0,\quad \bar{v}=0,\quad \frac{\partial \bar{T}}{\partial \bar{x}}=0 \quad at \quad \bar{x}=0 \quad and \quad 0\le \bar{y}\le 1$$

$$\bar{u}=0,\quad \bar{v}=0,\quad \frac{\partial \bar{T}}{\partial \bar{x}}=0 \quad at \quad \bar{x}=1 \quad and \quad 0\le \bar{y}\le 1$$

The non-dimensional variables used in the above formulation are defined as follows:

$$\bar{t} = \frac{t}{L_{ref}/u_{ref}}, \quad \bar{x} = \frac{x}{L_{ref}}, \quad \bar{y} = \frac{y}{L_{ref}}, \quad \bar{u} = \frac{u}{u_{ref}},$$

$$\bar{v} = \frac{v}{u_{ref}}, \quad \bar{p} = \frac{p}{\rho_{ref} u_{ref}^2}, \quad \bar{T} = \frac{T}{T_{ref}}, \quad \bar{\rho} = \frac{\rho}{\rho_{ref}},$$

$$\bar{\mu} = \frac{\mu}{\mu_{ref}}, \quad \bar{R} = \frac{R}{u_{ref}^2/T_{ref}}, \quad \bar{c}_p = \frac{c_p}{u_{ref}^2/T_{ref}},$$

$$Pr = \frac{c_p \mu}{k}, \quad M = \frac{u_{ref}}{\sqrt{\gamma R T_{ref}}}, \quad Re = \frac{\rho_{ref} u_{ref} L_{ref}}{\mu_{ref}}$$

Here, L_{ref} is the height (H) of the cavity; u_{ref} is the driven lid velocity; and all the transport and physical properties are evaluated at the reference temperature (T_{ref}) and pressure (p_{ref}) which are assumed to be that of atmospheric conditions.

5. Numerical Formulation and Solution Procedures

In this study, a 2-D model is simulated using ANSYS FLUENT 2015 under the given boundary conditions. The working fluid in the cavity is at STP with $M = 0.05$ and $Pr = 1$.

5.1 The Pressure-Based Coupled Algorithm

5.1.1 Discretization

ANSYS FLUENT uses a control-volume-based technique to convert the governing equations to algebraic equations that can be solved numerically by integrating the governing equations about each control volume, yielding discrete equations that conserve each quantity on a control-volume basis. The governing equations are discretized for the mesh (29 x 29) as shown in the figure 2.

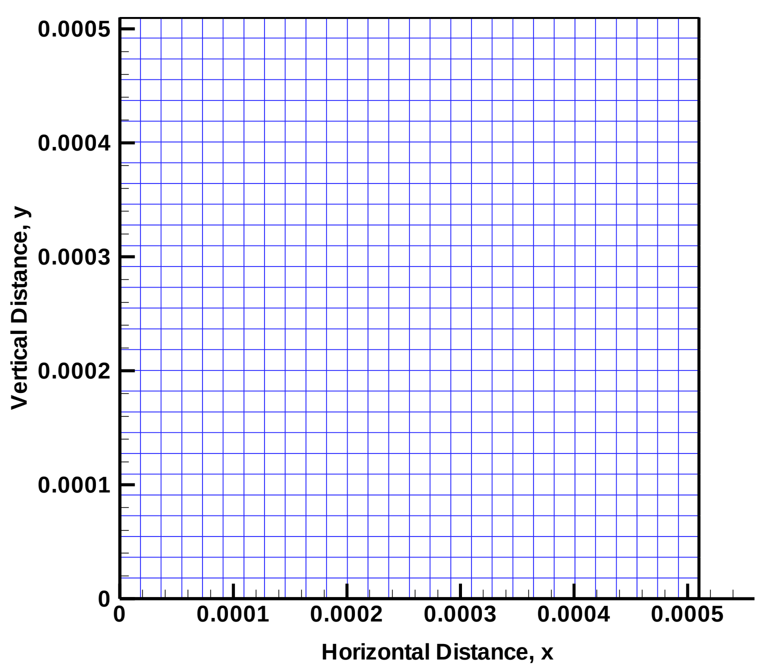

Figure 2 – Mesh of the computational domain

5.1.2 Solutions Technique

The discretized governing equations are solved using Pressure-Based solver [17] as the governing equations are non-linear and coupled. Therefore, the solution is carried out iteratively in order to obtain a converged numerical solution. The Pressure-based solver uses a solution algorithm which can solve the non-linear equations. There are four algorithms available in this technique namely Semi-Implicit Method for Pressure-Linked Equations (SIMPLE), SIMPLE-Consistent (SIMPLEC), Pressure Implicit with Splitting of Operators (PISO), and Coupled. In this Study “Coupled” algorithm was used since the momentum and continuity equations are solved in a closely coupled manner except energy equation which is solved in a decoupled fashion and therefore, the rate of solution convergence significantly improves when compared to the other techniques. Second-order upwind scheme is used for the spatial discretization of governing equation while the Second-order implicit scheme is used for transient formulation. With the Pressure-Based Coupled Algorithm, each iteration consists of the steps illustrated in figure 2. The algorithm is outlined below:

1. Update fluid properties (e.g., density, viscosity, specific heat) based on the current solution.
2. Solve a coupled system of equations comprising the momentum and pressure-based continuity equation. The remaining equations are solved in decoupled fashion.
3. Update mass fluxes, pressure and the velocity field.
4. Solver energy equation.
5. Check for the convergence of the equations.
6. If not converged then repeat the loop till convergence is obtained.

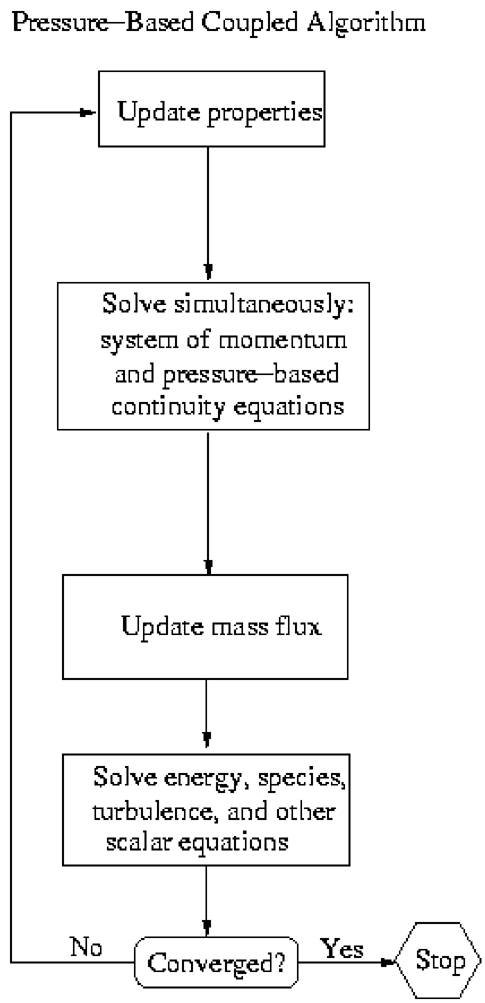

Figure 3 – Overview of pressure-based coupled algorithm

The solver settings used in ANSYS FLUENT are mentioned in table 1

Table 1 – Fluent solver settings

CFD SOLVER SETTINGS	
Description	**Settings**
Problem Setup – Solver	Pressure Based
Viscous	Laminar
Pressure-Velocity Coupling	Coupled
Gradient Discretization	Green Gauss Cell Based
Pressure Discretization	Second Order upwind
Density Discretization	Second Order upwind
Momentum Discretization	Second Order upwind
Energy	Second Order upwind
Transient formulation	Second Order upwind
Residual Criteria	1E-15

5.2 Coupled Modified Strongly Implicit Procedure (CMSIP)

A modified version of the Coupled Strongly Implicit Procedure (CSIP), developed by Akyuzlu *et al*. [15] and details of this procedure the reader should refer to Appendix [II]

It is assumed that the changes in kinetic and potential energy of the fluid, viscous dissipation, and the work done by the pressure changes are small. The density in the governing differential equations (Equations 4.6 to 4.9) were replaced by using ideal gas relation.

5.2.1 Transformation

The $\bar{x}$ and $\bar{y}$ oordinate system used in development of the conservations equations, (Equations 4.6 to 4.9), are transformed to the rigid (non-moving) coordinate $\bar{\xi}$ and $\bar{\sigma}$ system as follows [15]:

$$\bar{\sigma} = \frac{\bar{y}}{\bar{H}}$$

(5.1)

where $\bar{H}$ is defined as (h and r are normalized using L_{ref})

$$\bar{H} = \bar{h} + \bar{r}(\bar{x}, \bar{t}) \tag{5.2}$$

and

$$\bar{\xi} = \bar{x} \tag{5.3}$$

Based on the transformation given above the first order derivatives of any variable are given by:

$$\frac{\partial}{\partial \bar{t}}(\ ) = \frac{\partial}{\partial \bar{t}}(\ ) + \frac{\partial \bar{\sigma}}{\partial \bar{t}} \frac{\partial}{\partial \bar{\sigma}}(\ ) \tag{5.4}$$

where

$$\bar{\sigma}_t = \frac{\partial \bar{\sigma}}{\partial \bar{t}} = -\frac{\bar{\sigma}}{\bar{H}} \frac{\partial \bar{r}(\bar{x}, \bar{t})}{\partial \bar{t}} = -\frac{\bar{\sigma}}{\bar{H}} \dot{\bar{r}} \tag{5.5}$$

and

$$\frac{\partial}{\partial \bar{x}}(\ ) = \frac{\partial}{\partial \bar{\xi}}(\ ) + \frac{\partial \bar{\sigma}}{\partial \bar{x}} \frac{\partial}{\partial \bar{\sigma}}(\ ) \tag{5.6}$$

where

$$\bar{\sigma}_x = \frac{\partial \bar{\sigma}}{\partial \bar{x}} = -\frac{\bar{\sigma}}{\bar{H}} \frac{\partial \bar{r}(\bar{x}, \bar{t})}{\partial \bar{x}} \tag{5.7}$$

and

$$\frac{\partial}{\partial \overline{y}}(\ ) = \frac{\partial \overline{\sigma}}{\partial \overline{y}} \frac{\partial}{\partial \overline{\sigma}}(\ ) \tag{5.8}$$

where

$$\overline{\sigma}_y = \frac{\partial \overline{\sigma}}{\partial \overline{y}} = \frac{1}{\overline{\overline{H}}} \tag{5.9}$$

The second order partial derivative with respect to *x* is given by:

$$\frac{\partial}{\partial \overline{x}}\left(\frac{\partial}{\partial \overline{x}}(\ )\right) = \frac{\partial}{\partial \overline{\xi}}\left(\frac{\partial}{\partial \overline{\xi}}(\ )\right) + \frac{\partial}{\partial \overline{\xi}}\left[\left(-\frac{\overline{\sigma}}{\overline{\overline{H}}} \frac{\partial \overline{r}(\overline{x},\overline{t})}{\partial \overline{x}}\right)\frac{\partial}{\partial \overline{\sigma}}(\ )\right] \tag{5.10}$$

The second order partial derivative with respect to *y* is given by:

$$\frac{\partial}{\partial \overline{y}}\left(\frac{\partial}{\partial \overline{y}}(\ )\right) = \frac{\partial}{\partial \overline{\sigma}}\left(\frac{1}{\overline{\overline{H}}^2}\frac{\partial}{\partial \overline{\sigma}}(\ )\right) \tag{5.11}$$

The final version of the transformed form of the non-dimensional conservation equations is given in the Appendix [III].

5.2.2 Discretization

First, the governing differential equations (in non-dimensionalized and transformed form) are discretized using first order forward differencing for the time derivative terms, central differencing (second order accuracy) for all spatial derivatives (that is convective, viscous, and thermal diffusion terms) and pressure terms. Central differencing of flux (momentum and energy) quantities are evaluated at the face of the computational cell by simply averaging the flux quantities at each opposing side of the computational cell. See [15] for details of the discretization.

5.2.3 Linearization

The discretized non-dimensional conservation equations are linearized by Newton's linearization method. For example, the nonlinear term (*P/T*) in the continuity equation is linearized for the $(n+1)^{th}$ time (where *n* indicates the discretized time level and *k* indicates the iteration index) as follows:

$$\left(\frac{p}{T}\right)^{k+1} = \left(\frac{p}{T}\right)^{k} + \frac{\partial\left(\frac{p}{T}\right)^{k+1}}{\partial p}\left(p^{k+1} - p^{k}\right) + \frac{\partial\left(\frac{p}{T}\right)^{k+1}}{\partial T}\left(T^{k+1} - T^{k}\right) \tag{5.12}$$

After linearization, the conservation equations are put into following form for any nodal point (*i, j*) of the computational domain [15] :

$$\begin{aligned} &A^{6}_{i,j}\, x_{i-1,j-1} + A^{5}_{i,j}\, x_{i,j-1} + A^{4}_{i,j}\, x_{i+1,j-1} + \\ &\quad A^{7}_{i,j}\, x_{i-1,j} + A^{9}_{i,j}\, x_{i,j} + A^{3}_{i,j}\, x_{i+1,j} + \\ &\quad\quad A^{8}_{i,j}\, x_{i-1,j+1} + A^{1}_{i,j}\, x_{i,j+1} + A^{2}_{i,j}\, x_{i+1,j+1} = b_{i,j} \end{aligned} \tag{5.13}$$

Similar equations are generated for the rest of the inner nodal points of the computational domain. The resulting set of algebraic equations (as many as the number of inner nodes) is then put into block matrix form [15]

$$[A]\, x = b \tag{5.14}$$

Where [*A*] is the coefficient matrix with a 4x4 block in each element, *x* is the unknown vector, and *b* is the right hand side (known) vector. Computational molecule for A^1, A^2, A^3, . . ,and A^9 are shown in Figure 4.

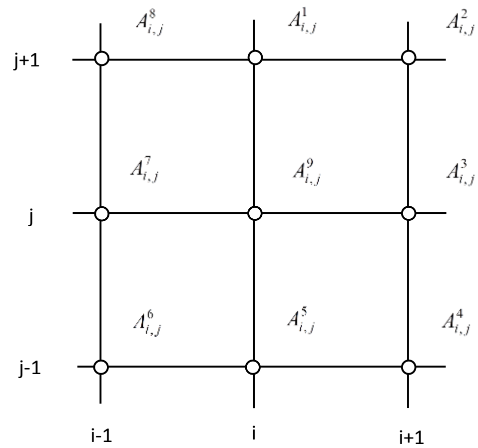

Figure 4 – Computational Molecule for the Elements of *A* Matrix

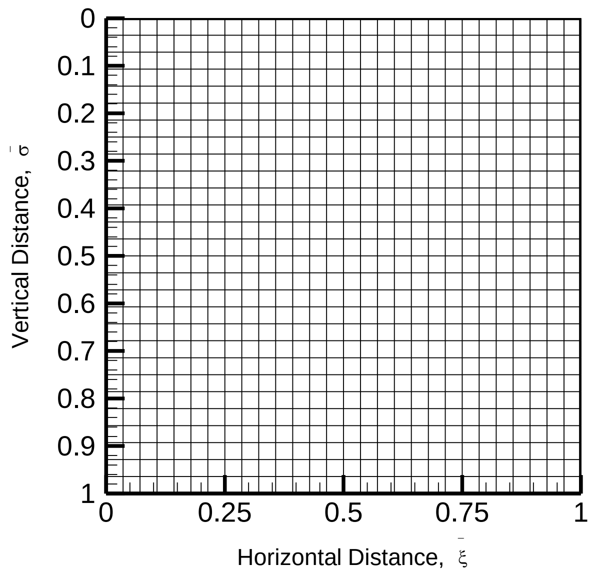

Figure 5 – Computational Mesh for the Transformed ($\bar{\xi}-\bar{\sigma}$) Domain

6. Steady State Lid Driven Cavity Flow – Results for Benchmark Case Study

In this study, numerical studies have been carried out to obtain the steady state solution of compressible lid driven cavity flow for various Reynolds number (100, 400, and 1000). The results obtained using FLUENT and CMSIP are validated by comparing with the benchmark case [1] by Ghia et.al [1] which solves for incompressible flow using vorticity equation and is shown in Figures through 6. Also a grid independence study is done to establish the accuracy of the solution.

6.1 Results for Steady State Lid Driven Cavity Flow Using Fluent.

In this study a compressible fluid at *Ma* = 0.05 and *Pr* = 1 is enclosed in a square cavity of aspect ratio 1.0 (*L* = *H* = 0.00051m in this case) at STP is assumed. The lid of the cavity is given a constant velocity at *Re* = 400 (17.3205m/ in this case) and the steady state solution using grid size of 39 x 39 obtained from FLUENT is shown in Figure 6.1. The parameters used and results for maximum u and v velocities are quantified in Table 2.

Table 2 – Common simulation Parameters for Lid Driven Cavity flow for Re = 400 by FLUENT

Simulation Parameters		
Parameter	**Unit**	**Value**
Length, *L*	[m]	0.00051
Height, *H*	[m]	0.00051
Lid Velocity, u_{lid}	[m/s]	17.3205
Operating Pressure, P_o	[pascals]	101325
Initial Temperature, T_i	[K]	300
Thermal Conductivity, *k*	[W/m-K]	0.02624
Specific Heat, c_p	[j/kg-K]	1004.9
Absolute Viscosity, μ	[N-s/m^2]	0.000026112
Mach Number, *Ma*		0.05
Reynolds Number, *Re*		400

Table 3 – Results for Lid Driven Cavity flow for Re = 400 by FLUENT

Results			
Maximum velocity, $\bar{u}$	**Minimum velocity, $\bar{u}$**	**Maximum velocity, $\bar{v}$**	**Minimum velocity, $\bar{v}$**
17.3205	-5.4190	4.9787	-7.1208

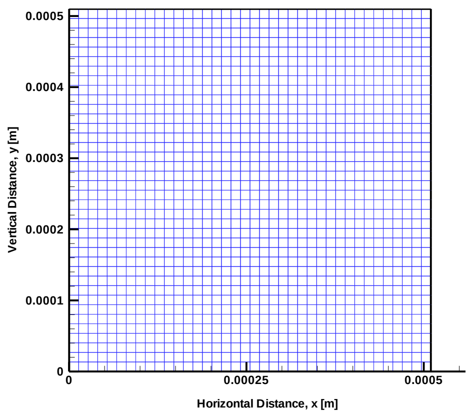

Figure 6 – Computational mesh of the domain

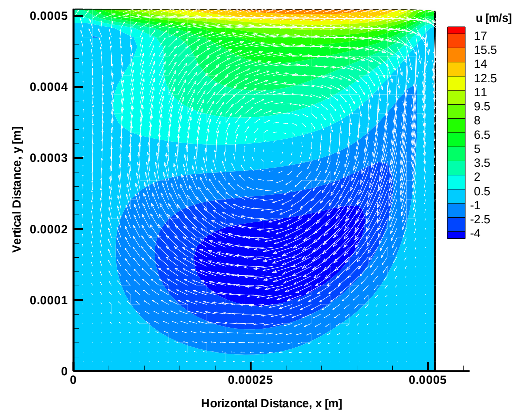

Figure 7 – u velocity contour for Re = 400

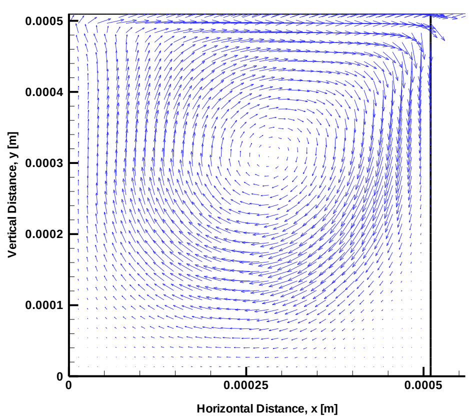

Figure 8 – Vectors of velocity magnitude for Re=400

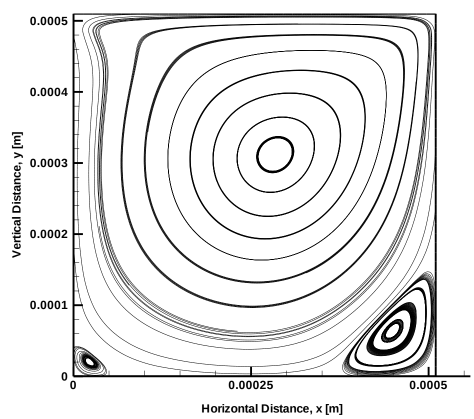

Figure 9 – Streamlines of velocity magnitude for Re=400

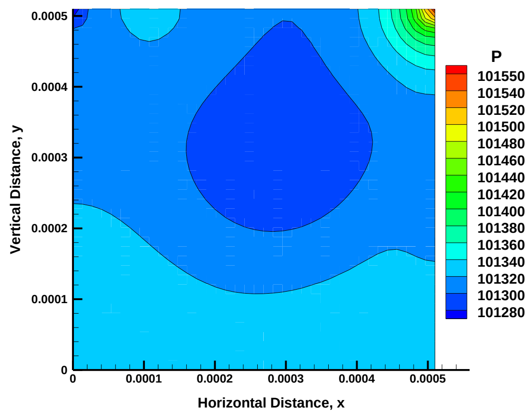

Figure 10 – Contour plot of pressure for Re=400

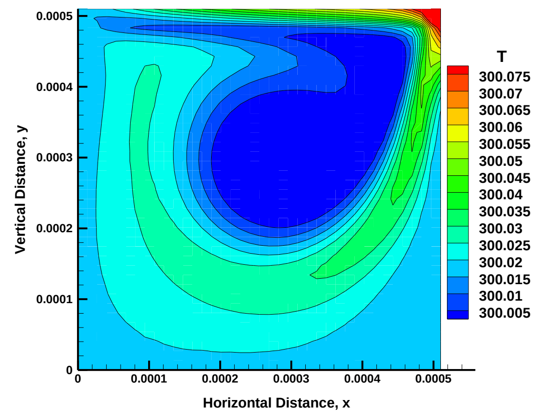

Figure 11 – Contour plot of temperature for Re=400

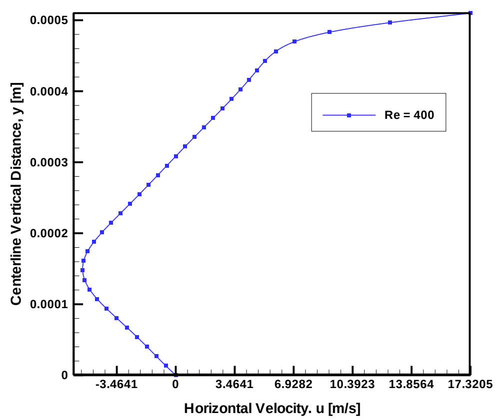

Figure 12 – *u* velocity distribution along vertical centerline for Re=400

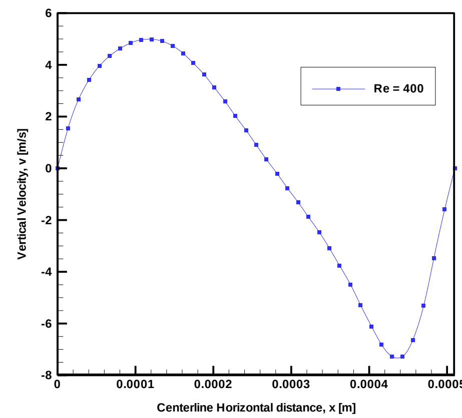

Figure 13 – *v* velocity distribution along horizontal centerline for Re=400

6.2 Comparison of Present Results (FLUENT) with CMSIP and Benchmark Case

The distribution of non-dimensional horizontal velocity ($\bar{u}$) and vertical velocity ($\bar{v}$) are plotted along non-dimensional centerline vertical distance ($\bar{y}$) and centerline horizontal distance ($\bar{x}$) respectively for comparing the results obtained using FLUENT, CMSIP and benchmark case (GHIA) for *Re* 100, 400, and 1000. The results are in good agreement for *Re* = 100 and 400 but there is a little deviation in magnitude of maximum velocities for *Re* = 1000 with the benchmark case as the fluid used is incompressible by Ghia *et al*. [1] and shown in the Figures 14 through 19.

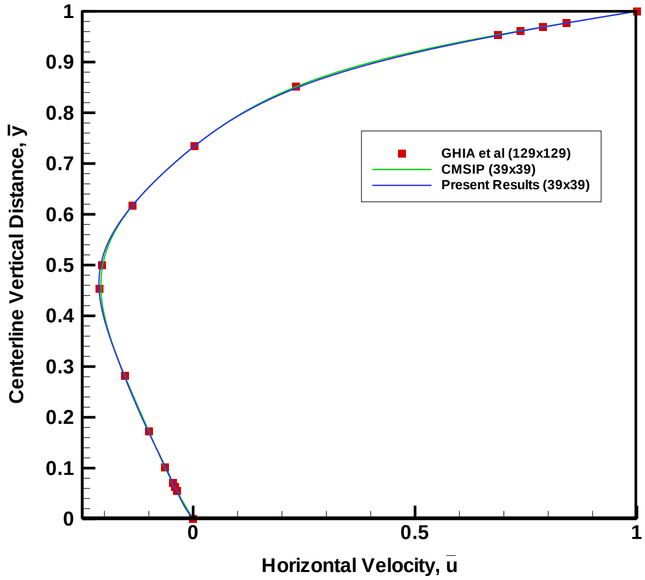

Figure 14 –Distribution of Horizontal Velocity ($\bar{u}$) along Centerline Vertical Distance for *Re* = 100 and *AR* 1.0.

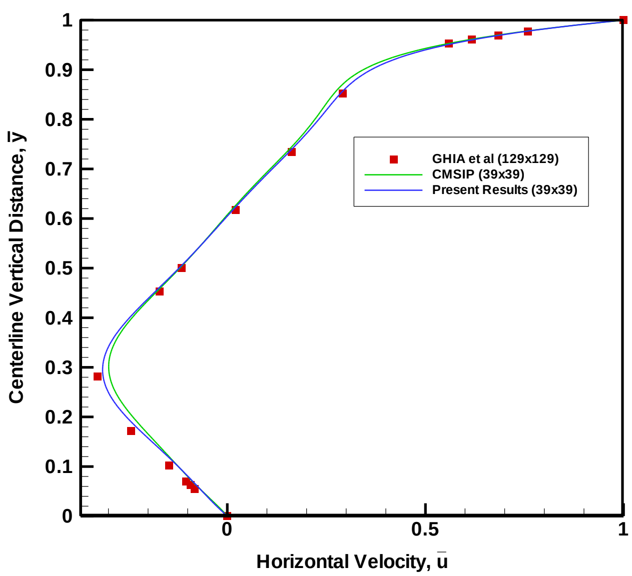

Figure 15 –Distribution of Horizontal Velocity ($\bar{u}$) along Centerline Vertical Distance for *Re* = 400 and *AR* 1.0

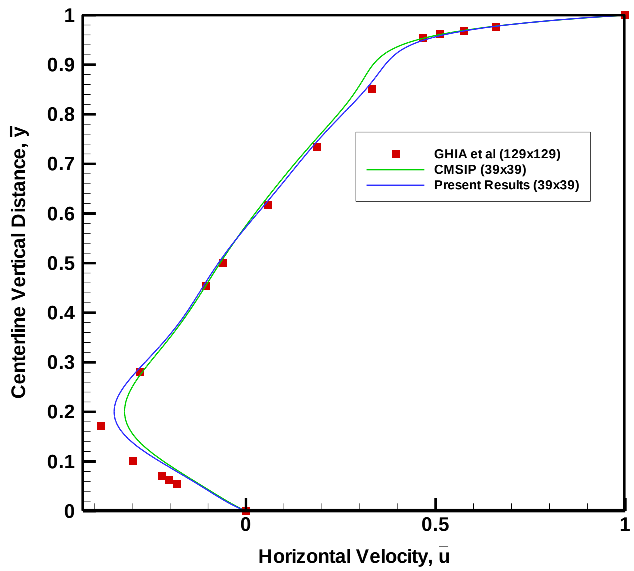

Figure 16 –Distribution of Horizontal Velocity ($\bar{u}$) along Centerline Vertical Distance for *Re* = 1000 and *AR* 1.0

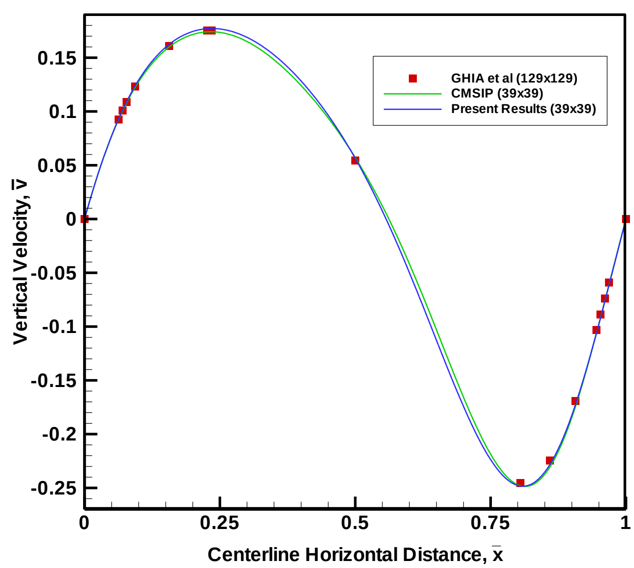

Figure 17 –Distribution of VerticalVelocity ($\bar{v}$) along Centerline Horizontal Distance for *Re* = 100 and A.R 1.0

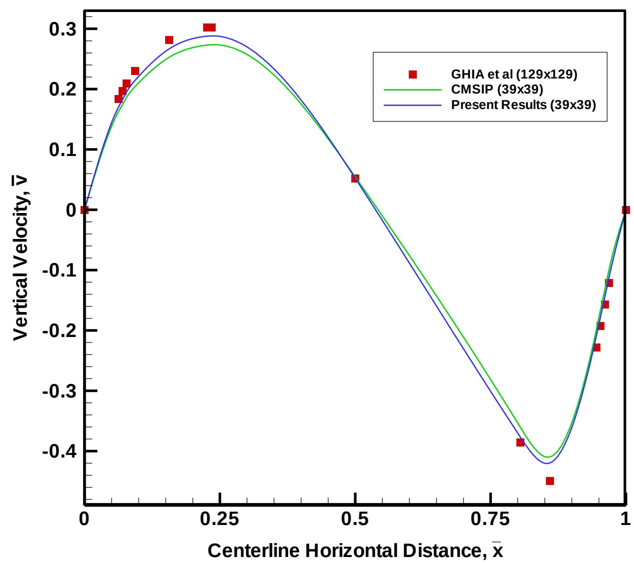

Figure 18 –Distribution of VerticalVelocity ($\bar{v}$) along Centerline Horizontal Distance for *Re* = 400 and A.R 1.0

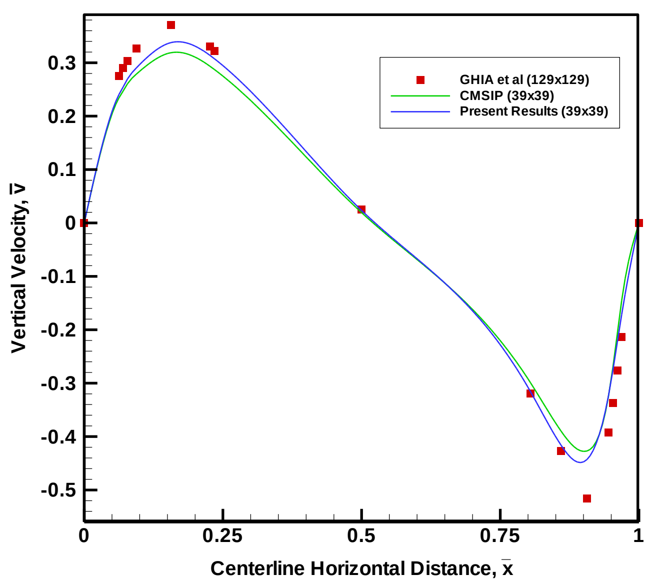

Figure 19 –Distribution of VerticalVelocity ($\bar{v}$) along Centerline Horizontal Distance for *Re* = 1000 and A.R 1.0

Table 4 and 5 show the comparison of the results (maximum and minimum velocities) of present results (FLUENT), CMSIP, and benchmark studies for the values of *Re* 100, 400, and 1000. The computational mesh size used in FLUENT and CMSIP results is 39 x 39 while the benchmark case (GHIA) is 129 x 129.

Table 4 – Comparison of the results for *u* velocities obtained from the benchmark, CMSIP, and FLUENT at different values of *Re*

Re	Value	GHIA $\bar{u}$	CMSIP $\bar{u}$	FLUENT $\bar{u}$	CMSIP % dev	FLUENT % dev
100	max	1.00000	1.00000	1.00000	0.00	0.00
	min	-0.21090	-0.20804	-0.21194	1.35	0.49
400	max	1.00000	1.00000	1.00000	0.00	0.00
	min	-0.32726	-0.29616	-0.31379	9.50	4.11
1000	max	1.00000	1.00000	1.00000	0.00	0.00
	min	-0.38289	-0.31434	-0.33775	17.90	11.79

Table 5 – Comparison of the results for *v* velocities obtained from the benchmark, CMSIP, and FLUENT at different values of *Re*

Re	Value	GHIA $\bar{v}$	CMSIP $\bar{v}$	FLUENT $\bar{v}$	CMSIP % dev	FLUENT % dev
100	Max	0.17527	0.17418	0.17727	0.62	1.14
	Min	-0.24533	-0.24796	-0.24826	1.07	1.19
400	Max	0.30203	0.27292	0.28770	9.64	4.74
	Min	-0.44993	-0.40974	-0.41968	8.93	6.72
1000	Max	0.37095	0.31883	0.33774	14.05	8.95
	Min	-0.51550	-0.42705	-0.44291	17.16	14.08

6.3 Grid Independence Study

The grid independence study is done for different mesh sizes of 19 x 19 (coarse), 29 x 29, 39 x 39 (medium) and 81 x 81 (fine). The distribution of non-dimensional horizontal velocity ($\bar{u}$) and vertical velocity ($\bar{v}$) are plotted along non-dimensional centerline vertical distance ($\bar{y}$) and centerline horizontal distance ($\bar{x}$) respectively for comparing the results obtained using FLUENT for Re 400 shown in figure 20 and 21. The results are quantified in Table 6. The results obtained for mesh size of 39 x 39 and 81 x 81 are very much similar when compared to coarse mesh size of for 19 x 19 and 29 x 29. The geometrical, operational, and physical parameters for this case study are similar to that of the previous case studies.

Table 6 –Results for grid independence study for steady state driven cavity flow

Results			
Maximum velocity, $\bar{u}$	**Minimum velocity, $\bar{u}$**	**Maximum velocity, $\bar{v}$**	**Minimum velocity, $\bar{v}$**
1.00000	-0.26623	0.22964	-0.32868
1.00000	-0.29390	0.27216	-0.38738
1.00000	-0.31287	0.28745	-0.41112
1.00000	-0.32581	0.30045	-0.42937

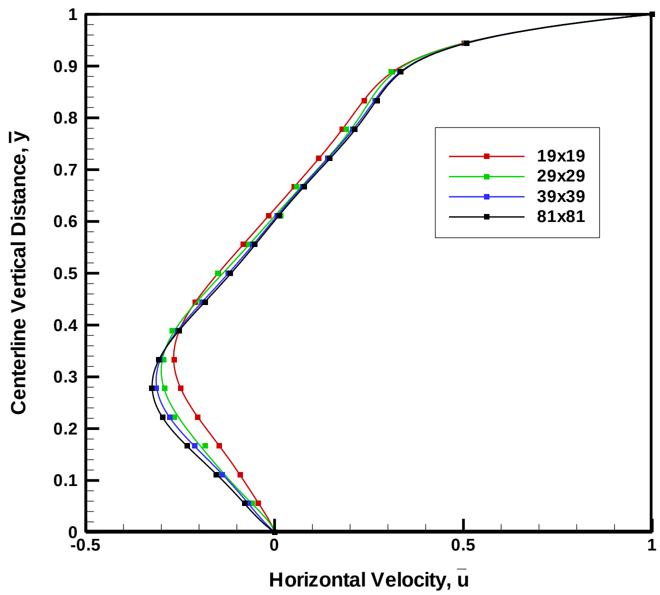

Figure 20 –Distribution of Horizontal Velocity ($\bar{u}$) along Centerline Vertical Distance for *Re* = 400 and A.R 1.0 for different mesh sizes.

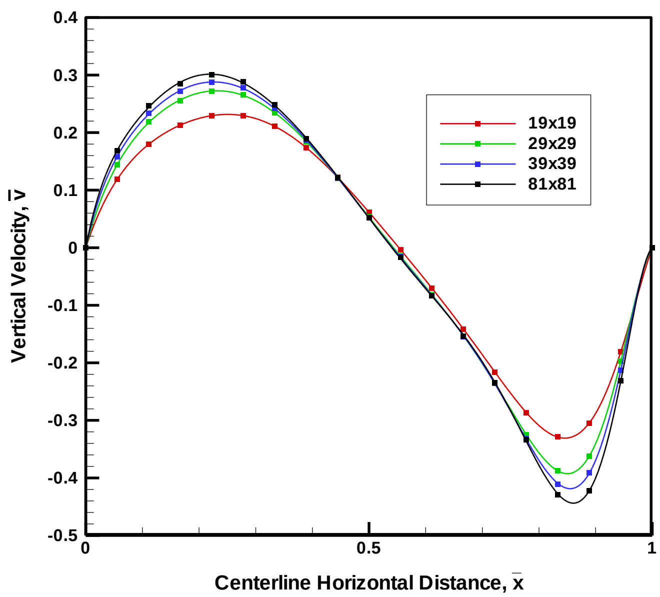

Figure 21 –Distribution of Vertical Velocity ($\bar{v}$) along Centerline Horizontal Distance for *Re* = 400 and A.R 1.0 for different mesh sizes.

6.4 Effects of Different Reynolds Number using FLUENT and CMSIP

A Parametric study is conducted and results are compared between FLUENT and CMSIP to see the effects of flow inside the cavity for different Reynolds numbers 100, 400, and 1000. The Table 6 shows the maximum $\bar{u}$ and $\bar{v}$ velocities for various Reynolds numbers. The distribution of non-dimensional horizontal velocity ($\bar{u}$) and vertical velocity ($\bar{v}$) are plotted along non-dimensional centerline vertical distance ($\bar{y}$) and centerline horizontal distance ($\bar{x}$) respectively are shown Figures 22 through 27 and the results are quantified in Table 7. The geometrical, operational and physical parameters for this case study are similar to that of the previous case studies. The results obtained are in good agreement with each other and the contour plots are generated (Figure 28) to see the distribution of primitive variables in the cavity. It can be seen that the primary circulation (center) moves towards the center of the cavity as Reynolds number increases and the formation of secondary circulation (corner) increases in size with increase in Reynolds number and is shown in the vector and streamline plots as shown in figure 29 and 30.

Table 7 –Results for different Reynolds number Study for Steady State Driven Cavity Flow

		Results					
Reynolds No.	Value	CMSIP $\bar{u}$	FLUENT $\bar{u}$	dev %	CMSIP $\bar{v}$	FLUENT $\bar{v}$	dev %
100	max	1.00000	1.00000	0.00	1.00000	1.00000	0.00
	min	-0.20714	-0.21198	-2.34	-0.24678	-0.24948	-1.09
400	max	1.00000	1.00000	0.00	1.00000	1.00000	0.00
	min	-0.29854	-0.31595	-5.83	-0.41166	-0.41960	-1.93
1000	max	1.00000	1.00000	0.00	1.00000	1.00000	0.00
	min	-0.32510	-0.34894	11.32	-0.43387	-0.45571	-5.03

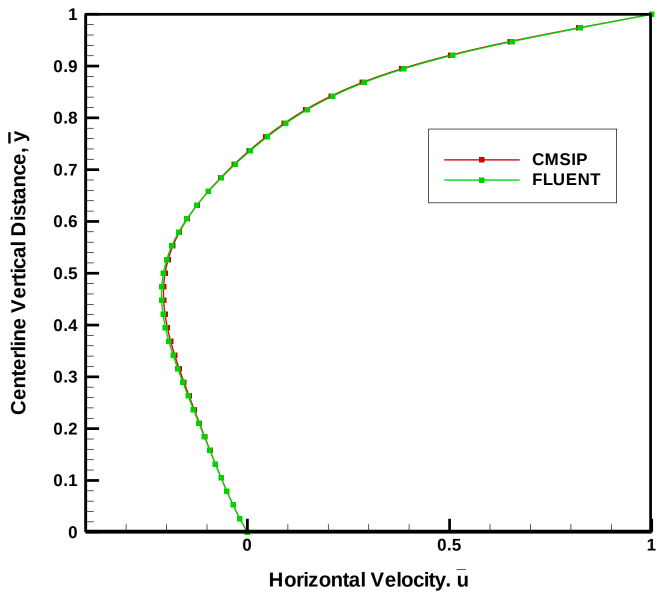

Figure 22 –Distribution of Horizontal Velocity ($\bar{u}$) along Centerline Vertical Distance for *Re* = 100 and *AR* 1.0

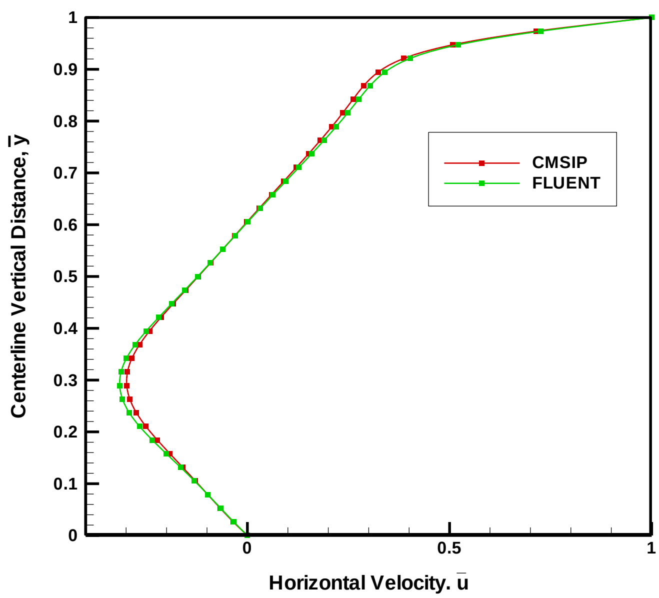

Figure 23 –Distribution of Horizontal Velocity ($\bar{u}$) along Centerline Vertical Distance for *Re* = 400 and *AR* 1.0

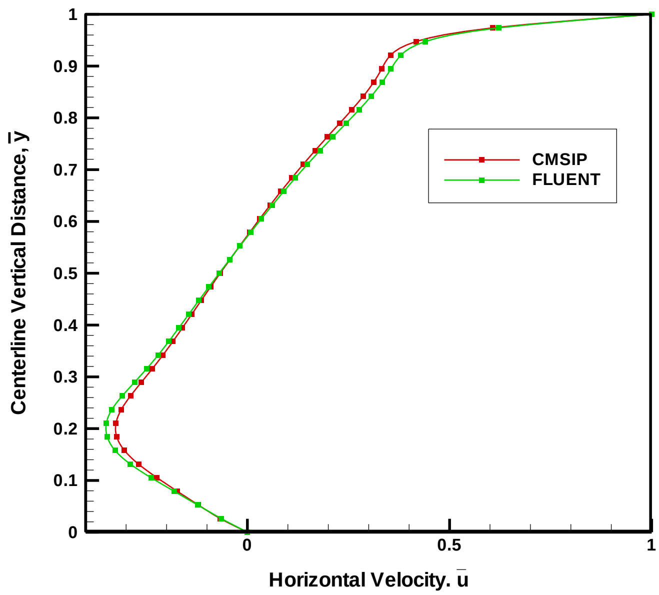

Figure 24 –Distribution of Horizontal Velocity ($\bar{u}$) along Centerline Vertical Distance for *Re* = 1000 and *AR* 1.0

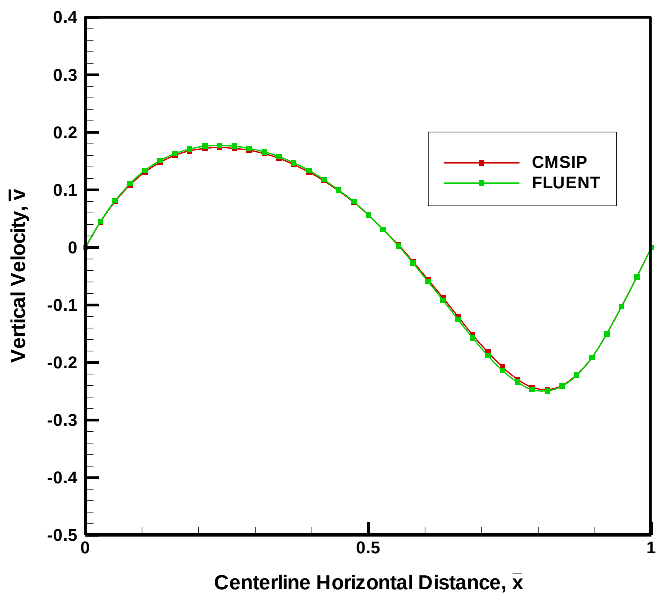

Figure 25 –Distribution of Vertical Velocity ($\bar{v}$) along Centerline Horizontal Distance for *Re* = 100 and *AR* 1.0

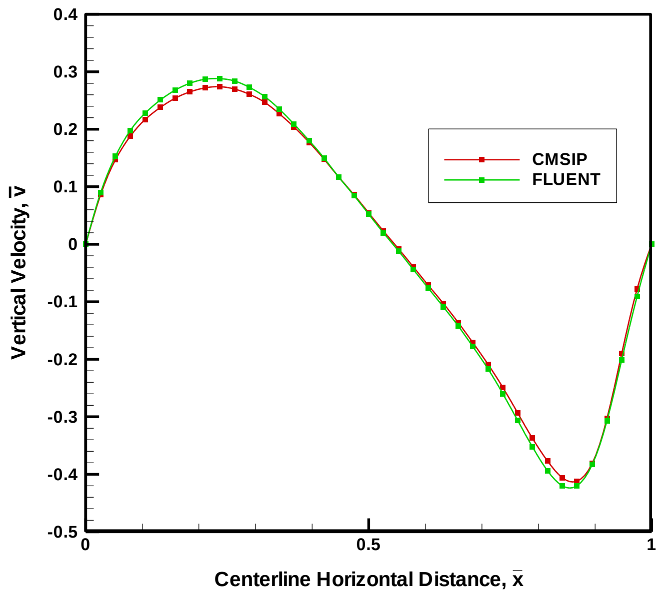

Figure 26 –Distribution of Vertical Velocity ($\bar{v}$) along Centerline Horizontal Distance for *Re* = 400 and *AR* 1.0

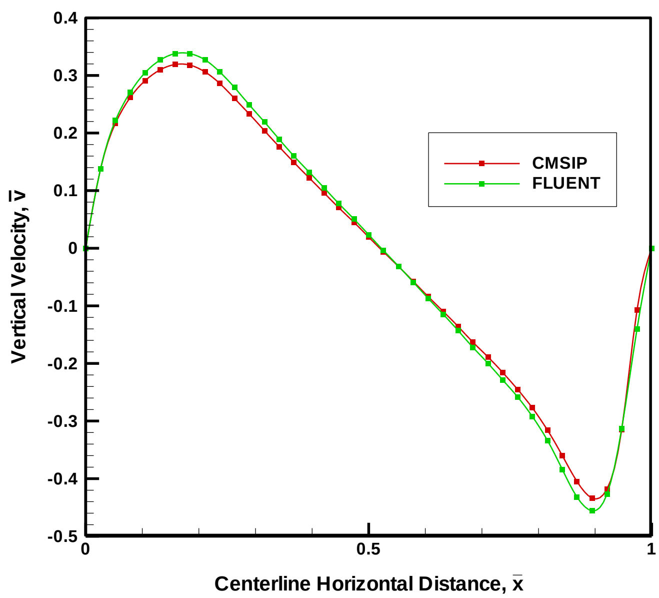

Figure 27 – Distribution of Vertical Velocity ($\bar{v}$) along Centerline Horizontal Distance for *Re* = 1000 and *AR* 1.0

The Figures 28 through 31 show the comparison of contour plots for the pressure and temperature, vector plot and Streamline plot of velocity magnitude.

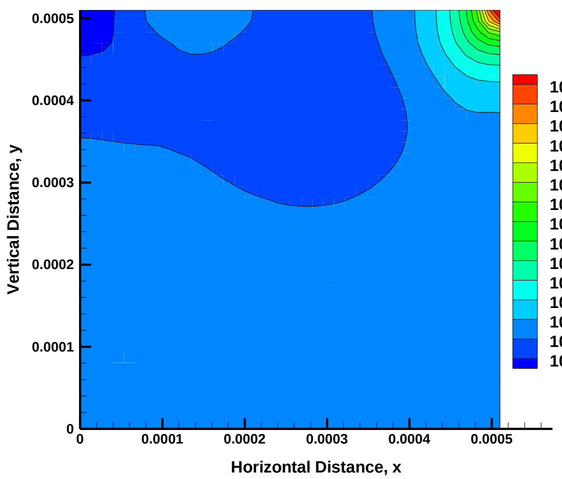

Figure 28 – Pressure contour plot for *Re* = 100 (FLUENT)

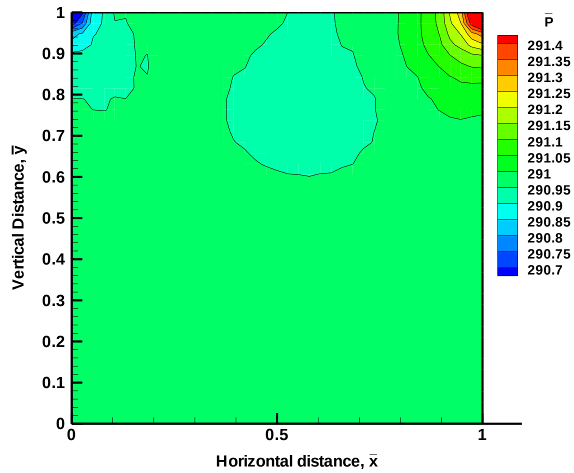

Figure 29 – Pressure contour plot for *Re* = 100 (CMSIP)

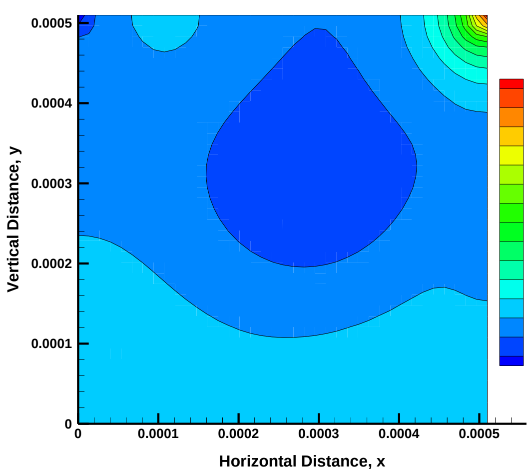

Figure 30 – Pressure contour plot for *Re* = 400 (FLUENT)

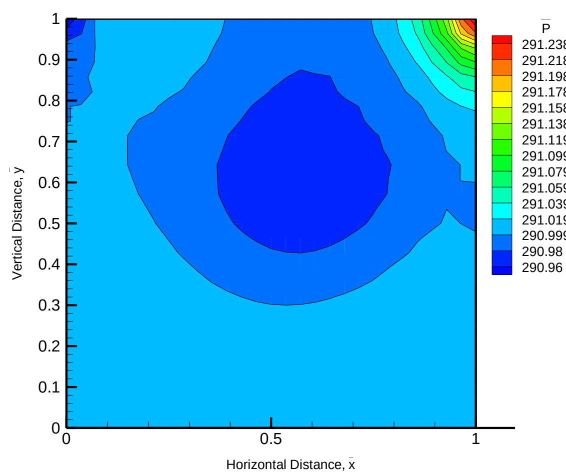

Figure 31 – Pressure contour plot for *Re* = 400 (CMSIP)

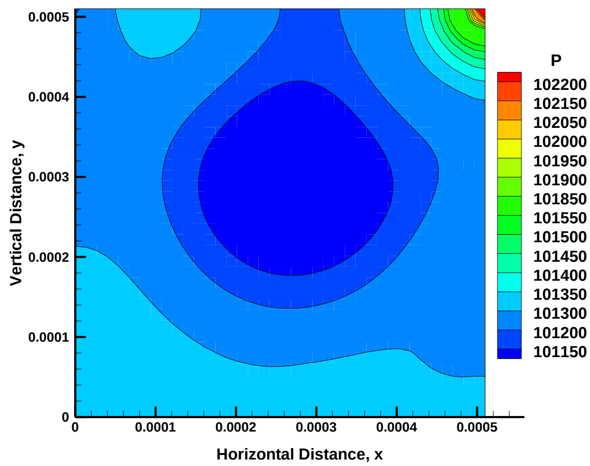

Figure 32 – Pressure contour plot for *Re* = 1000 (FLUENT)

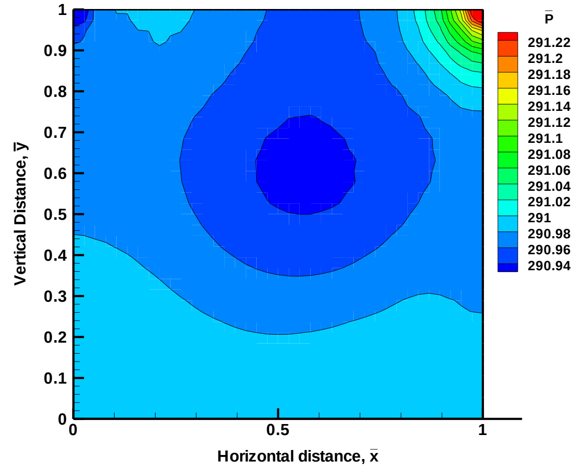

Figure 33 – Pressure contour plot for *Re* = 400 (CMSIP)

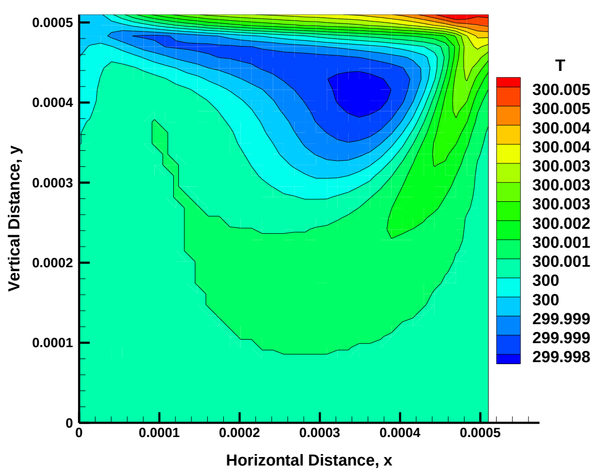

Figure 34 – Temperature contour plot for *Re* = 100 (FLUENT)

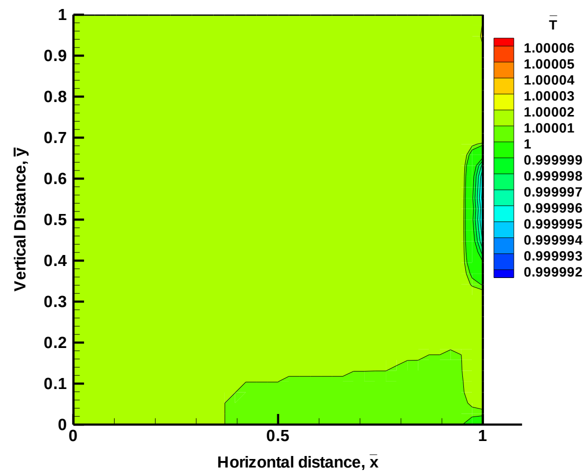

Figure 35 – Temperature contour plot for *Re* = 1000 (CMSIP)

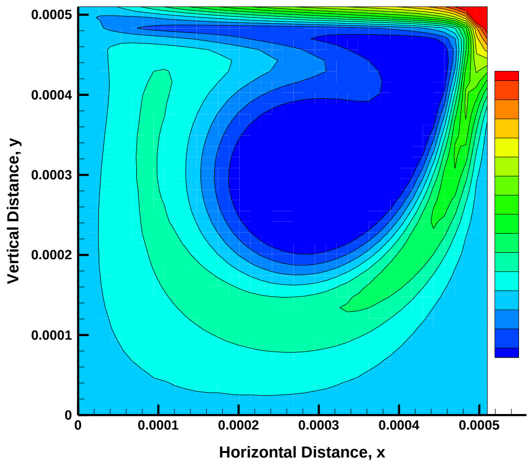

Figure 36 – Temperature contour plot for *Re* = 400 (FLUENT)

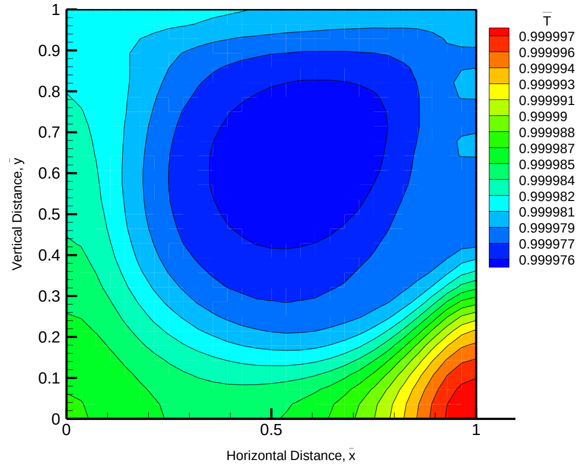

Figure 37 – Temperature contour plot for *Re* = 400 (CMSIP)

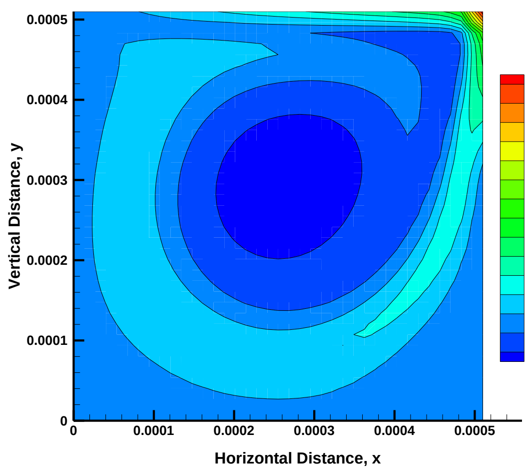

Figure 38 – Temperature contour plot for *Re* = 1000 (FLUENT)

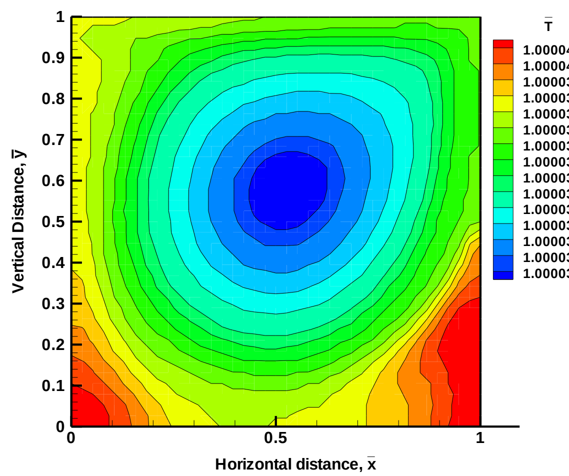

Figure 39 – Temperature contour plot for *Re* = 1000 (CMSIP)

7. Mesh Motion Study for the Moving Bottom Boundary

In this study a rectangular infinite domain enclosed by compressible fluid at *M* = 0.05 and *Pr* = 1 is considered (shown in figure 40) of aspect ratio 3 with a moving bottom boundary. The assumptions and mathematical formulation are same as the square cavity of *AR* 1.0 in previous case except the Lid of the cavity is stationary in this case. The moving bottom boundary is given a constant velocity ($\bar{v}_b$) as a step function which moves in negative *y* direction from non-dimensional time, $\bar{t}$ = 10 to 20. As the cavity increases in length, the computational mesh of the cavity also increases either by adding of new cells or non-uniform and uniform expansion of cells.

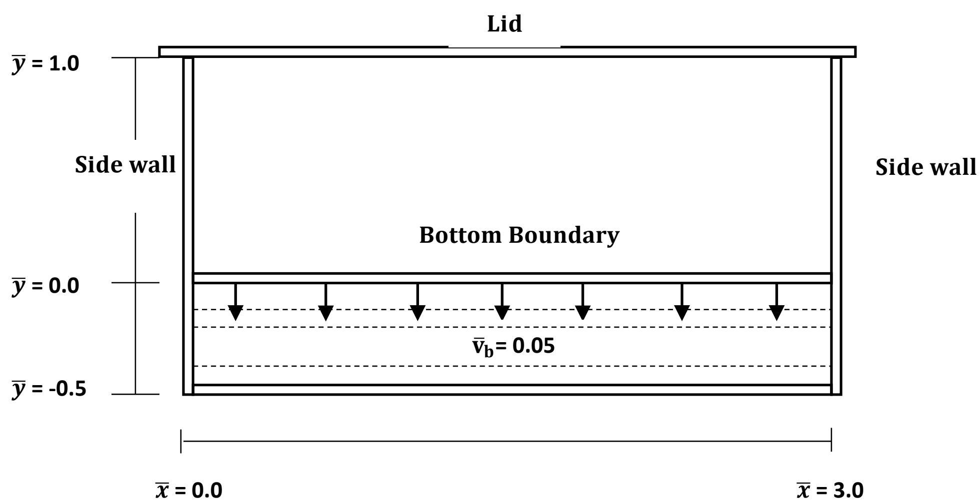

Figure 40 – Schematic of the infinite rectangular cavity of *AR* 3.0

The Fluent solver has three methods to deform the mesh namely Dynamic Layering, Spring-Based Smoothing, and User-Defined Function.

7.1 Mesh Motion using Layering Technique

Dynamic Layering [16] adds or removes layers of cells next to a moving boundary based on the height of the cell layer adjacent to the boundary. This technique requires cell height as an input and so as the bottom wall moves using a profile which is specified in dynamic-mesh settings. The bottom wall uses profile for the motion and dynamic mesh setting deforms the mesh. In Layering it adds cells till the bottom boundary stops.

In prismatic (hexahedral and/or wedge) mesh zones, dynamic layering is used to add or remove layers of cells adjacent to a moving boundary, based on the height of the layer adjacent to the moving surface. The dynamic mesh model in ANSYS Fluent allows to specify an ideal layer height on each moving boundary. The layer of cells adjacent to the moving boundary (layer j in Figure 41 – Dynamic Layering) is split or merged with the layer of cells next to it (layer i in Figure 41 – Dynamic Layering) based on the height (h) of the cells in layer .

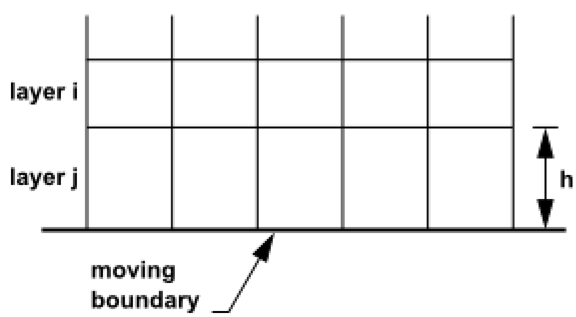

Figure 41 – Dynamic Layering

The computational mesh used in this study consists of 28 cell division in y-direction and 84 cell division in x-direction and shown in the figure 42

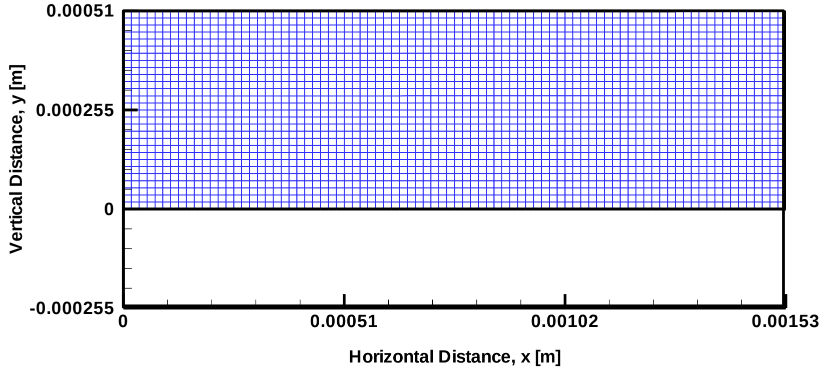

Figure 42 – Computational mesh of the domain before moving of the bottom boundary (A.R 3.0)

7.2 Mesh Motion using Spring-Based Technique

The spring-based smoothing [14] treats the edges between two nodes as springs. The movement of the boundary nodes create a "force" that, using hook's Law, is used to calculate a displacement for all the interior nodes in the deforming boundary. Spring smoothing is applicable to all deforming zones with dynamic boundaries and best used with tetrahedral cells, but can be used for non-tetrahedral cells.

This technique require Spring constant as an input which ranges from 0 to 1.As the bottom wall moves using a profile using dynamic mesh settings. The bottom wall uses profile for the motion and dynamic mesh setting deforms the mesh. In Spring-Based Smoothing it treats the edges between two nodes as springs. The movement of the boundary nodes create a "force" that, using hook's Law, is used to calculate a displacement for all the interior nodes in the deforming boundary. Spring smoothing is applicable to all deforming zones with dynamic boundaries and best used with tetrahedral cells, but can be used for non-tetrahedral cells.

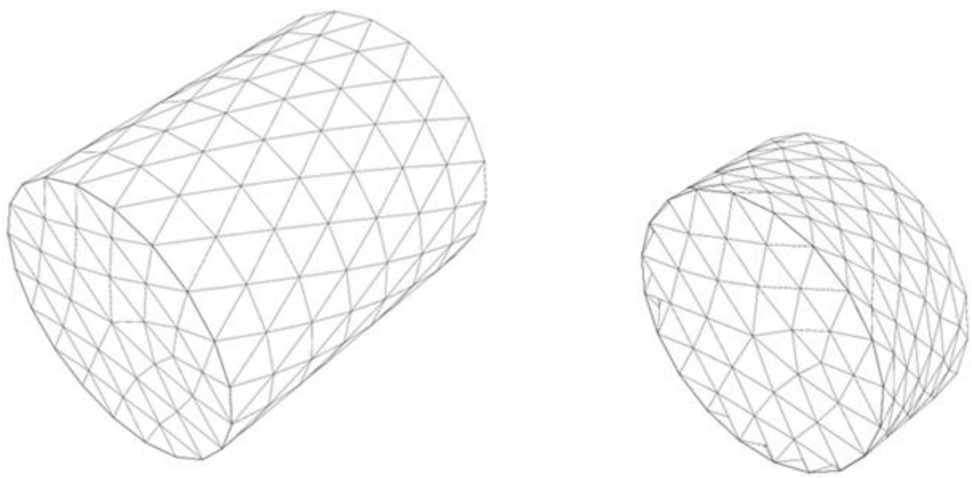

(a) Spring-Based Smoothing on Interior Nodes: Start

(b) Spring-Based Smoothing on Interior nodes: End

Figure 43– Deforming of mesh using Spring-Based Smoothing technique

7.3 Mesh Motion using User-Defined Function (UDF)

Deforming the mesh using user-defined [16] Dynamic Mesh Setting which uses UDF DEFINE_GRID_MOTION is written in C-program and compiled in FLUENT. The DEFINE_GRID_MOTION macro utilizes input from the UDF to move the nodes on the dynamic zone to an updated position for the new time step. All the node positions are updated independently of one another on the dynamic zone, instead acting as a function of the data in the UDF [14].

The Program was developed successfully for the present study and is described in detailed [See Appendix [IV]-. This UDF deforms all the cells uniformly without any addition or distortion of cell.

7.4 Results of Mesh Motion Techniques

The results are obtained using these techniques and compared to determine which technique best suits to our problem. The figure 44 gives the bottom boundary $\bar{v}$ velocity profile which starts from non-dimensional time $\bar{t} = 10$ and stops at $\bar{t} = 20$ when the cavity reaches the *AR* 1.5. The velocity distribution for $\bar{u}$ and $\bar{v}$ is given on centerline distance $\bar{y}$ and centerline distance $\bar{x}$ (between 1.0 to 2.0) respectively. Histograms are plotted at $\bar{x} = 0.5, \bar{y} = 0.68$ for all primitive variables $\bar{u}$, $\bar{v}$, $\bar{P}$, $\bar{T}$ and $\bar{\rho}$. Histogram helps in determining the accuracy and convergence of the program. Some oscillations can be seen for $\bar{u}$ and $\bar{v}$ velocity histograms, there is considerable decrease in magnitude of pressure, temperature and density while the bottom wall is moving and can be seen in figures 48 to 52. Since there is no Lid velocity the magnitude of $\bar{u}$ velocities are zero all the time. $\bar{v}$ velocities are compared when the aspect ratio is A.R 1.1 and 1.2 in figure 55 and 56. It is observed that layering technique is suitable for present study in which the side walls are stationary unlike UDF in which even the side walls move. The spring-Based Technique distorts the *AR* ratio of cell closer to the moving boundary higher than the cells away from boundary (figure 46) and is not preferred in this study. The simulation parameters used in this case study are given in table 8 for *M* = 0.05 and *Pr* = 1

Table 8 – Simulation parameters for infinite rectangular cavity

Parameter	Unit	Value
Length, L	[m]	0.00153
Height, H	[m]	0.00051
Non-Dimensional Bottom Boundary Velocity, $\bar{v}_b$	[m/s]	0.05
Operating Pressure, P_o	[pascals]	101325
Initial Temperature, T_i	[K]	300
Thermal Conductivity, k	[W/m-K]	0.02624
Specific Heat, c_p	[j/kg-K]	1004.9
Absolute Viscosity, μ	[N-s/m^2]	0.000026112

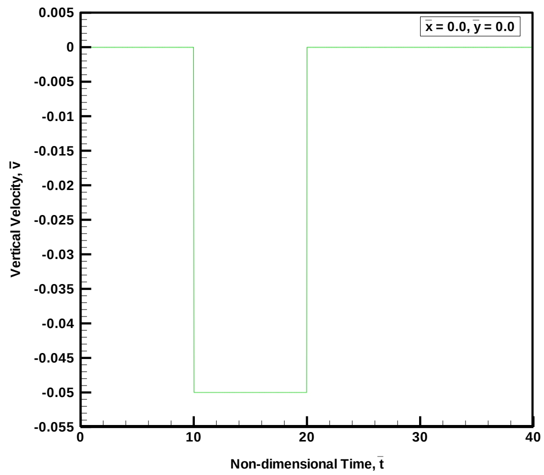

Figure 44 – $\bar{v}$ velocity histogram for the motion of bottom boundary at at node at $\bar{x} = 0.0, \bar{y} = 0.0$ for different mesh motion studies.

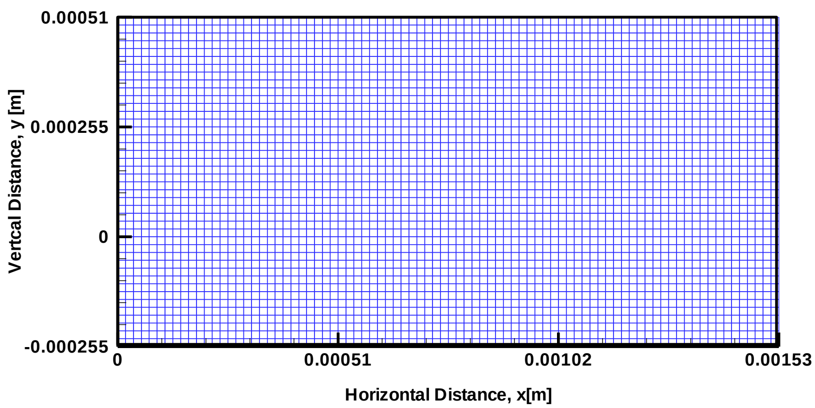

Figure 45 – Computational mesh of the domain after moving of the bottom boundary using Layering technique (*AR* 3.0)

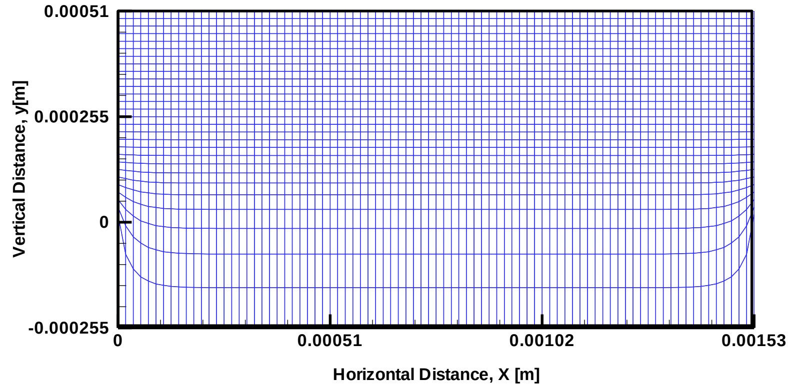

Figure 46 – Computational mesh of the domain after moving of the bottom boundary using Spring-Based technique (*AR* 3.0)

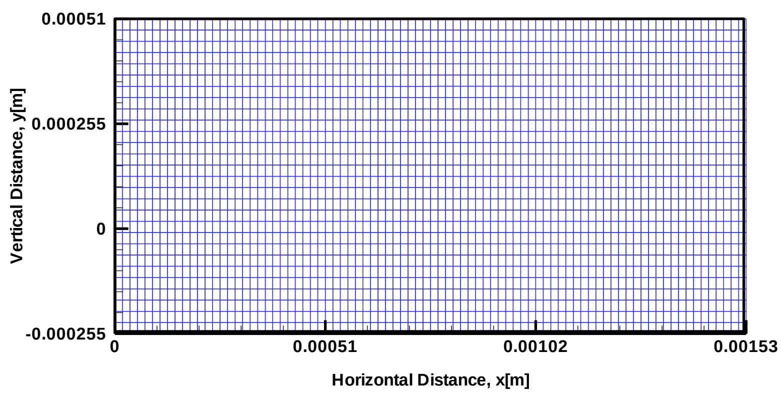

Figure 47 – Computational mesh of the domain after moving of the bottom boundary using User-Defined technique (A.R 1.5)

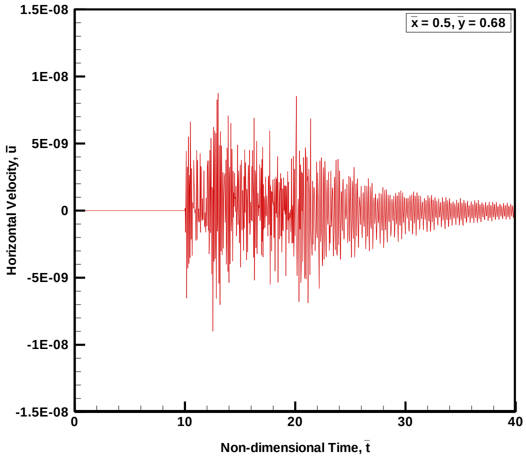

a. Layering

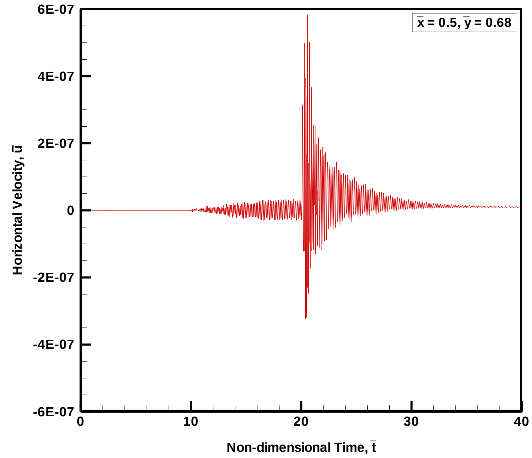

b. Spring-Based

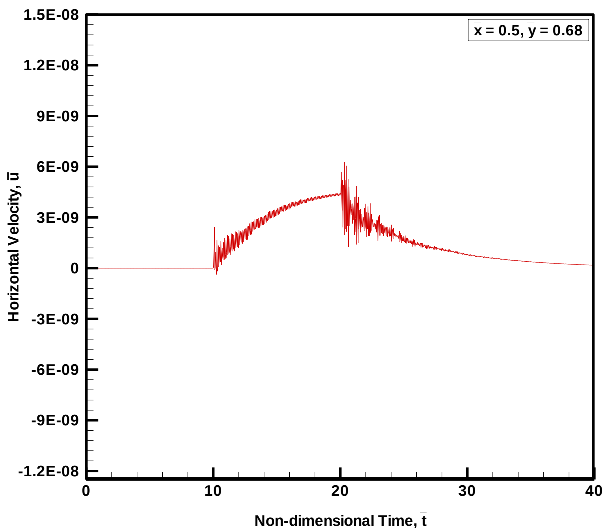

c. User-Defined Function

Figure 48– $\bar{u}$ velocity histogram at node at $\bar{x} = 0.5, \bar{y} = 0.68$ for different mesh motion studies. (a. using Layering, b. Using Spring-Based and c. Using UDF)

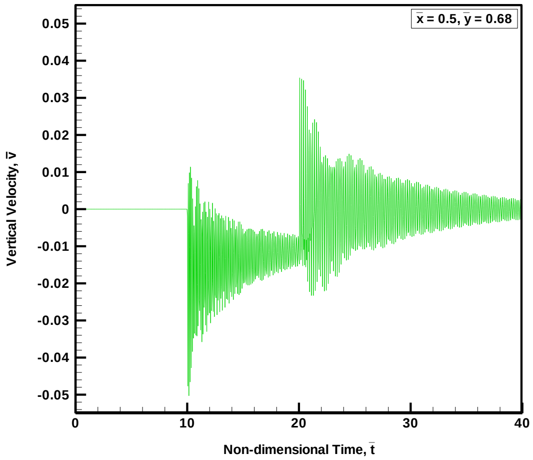

a. Layering

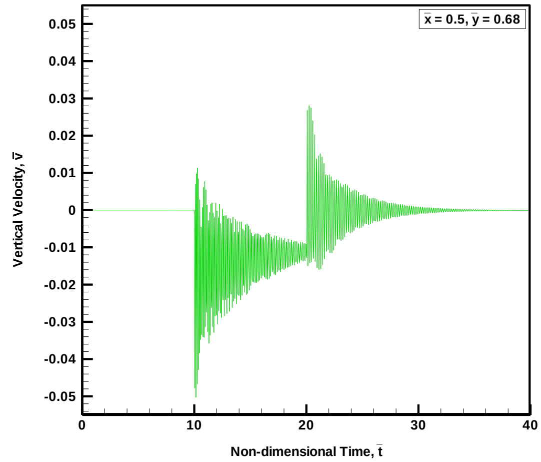

b. Spring-Based

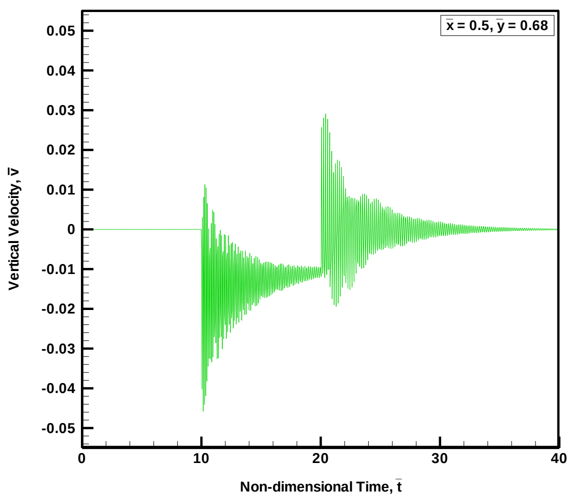

c. User-Defined Function

Figure 49– $\bar{v}$ velocity histogram at node at $\bar{x} = 0.5, \bar{y} = 0.68$ for different mesh motion studies. (a. using Layering, b. Using Spring-Based and c. Using UDF)

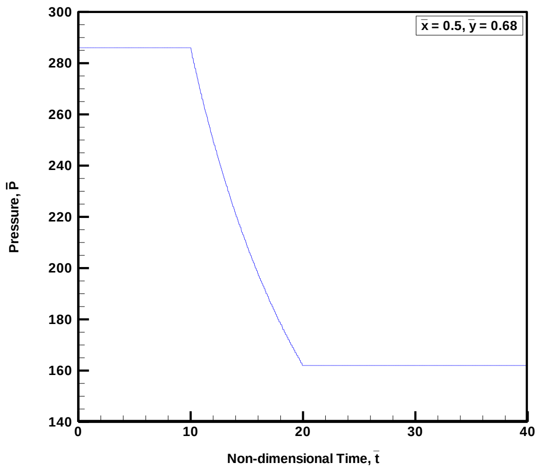

a. Layering

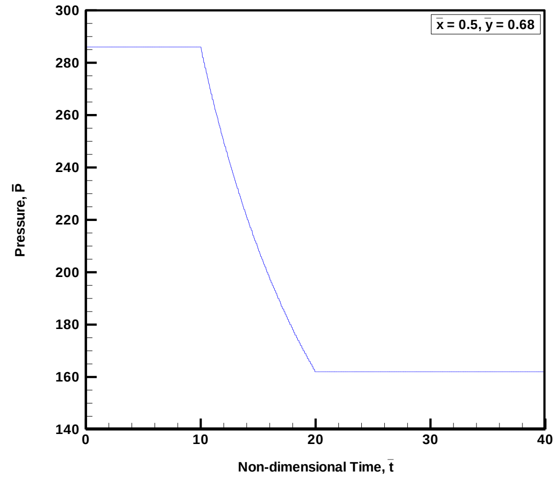

b. Spring-Based

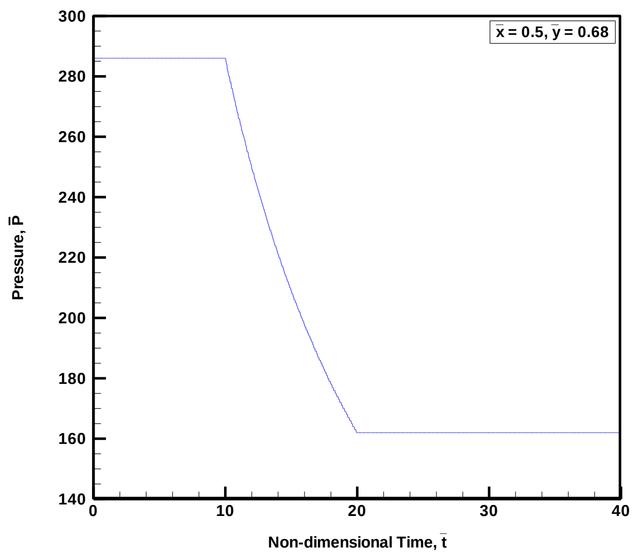

c. User-Defined Function

Figure 50 – $\bar{P}$ pressure histogram at node at $\bar{x} = 0.5, \bar{y} = 0.68$ for different mesh motion studies (a. using Layering, b. Using Spring-Based and c. Using UDF)

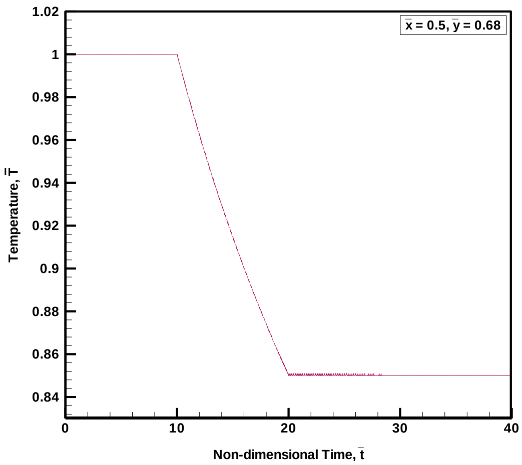

a. Layering

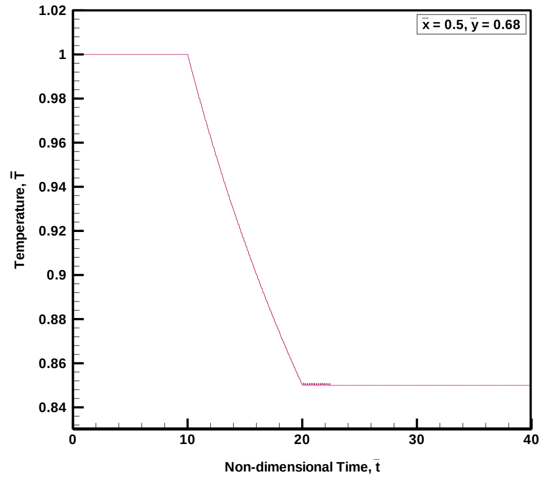

b. Spring-Based

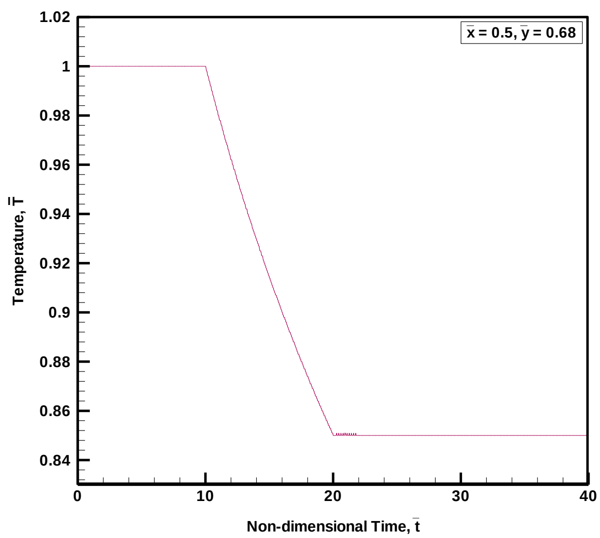

c. User-Defined Function

Figure 51 – $\bar{T}$ Temperature histogram at node at $\bar{x} = 0.5, \bar{y} = 0.68$ for different mesh motion studies. (a. using Layering, b. Using Spring-Based and c. Using UDF)

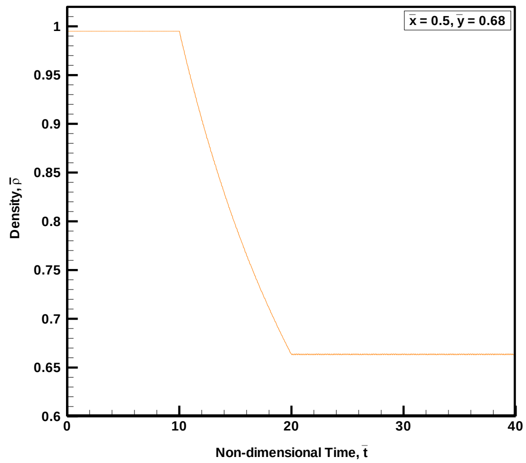

a. Layering

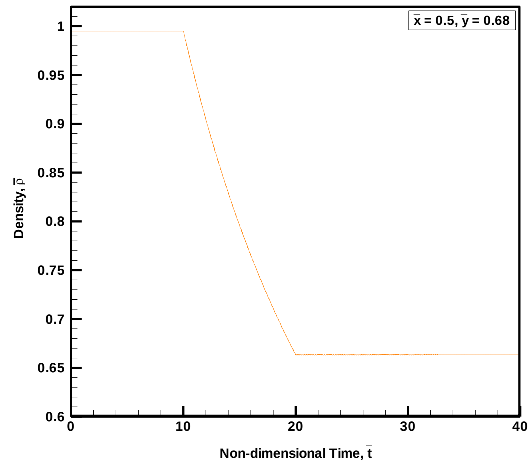

b. Spring-Based

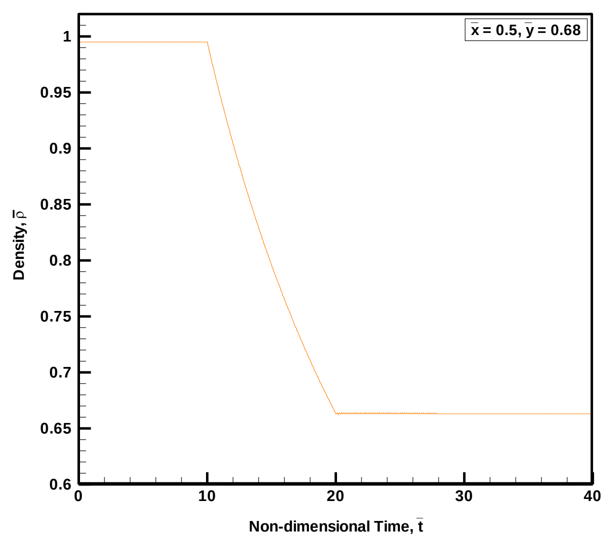

c. User-Defined Function

Figure 52 – $\bar{\rho}$ Density histogram at node at $\bar{x} = 0.5, \bar{y} = 0.68$ for different mesh motion studies (a. using Layering, b. Using Spring-Based and c. Using UDF)

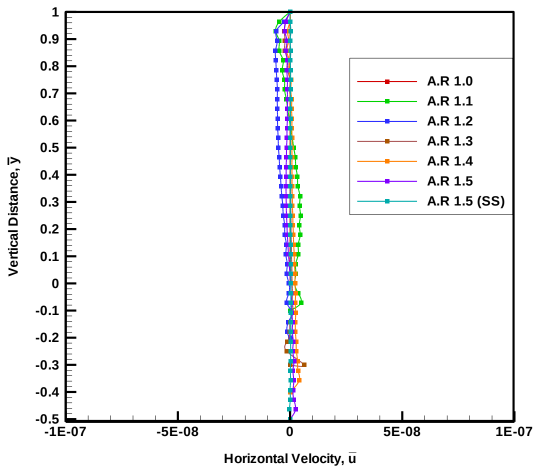

a. Layering

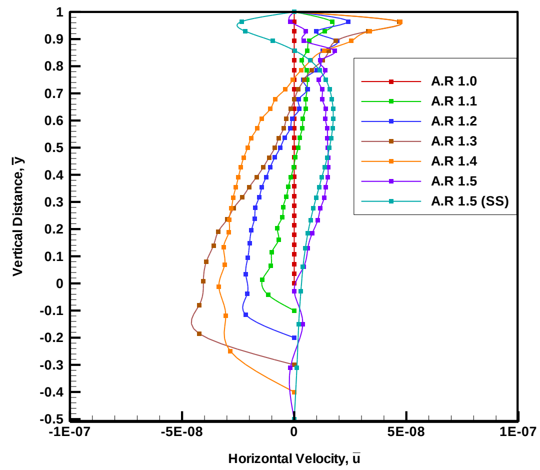

b. Spring-Based

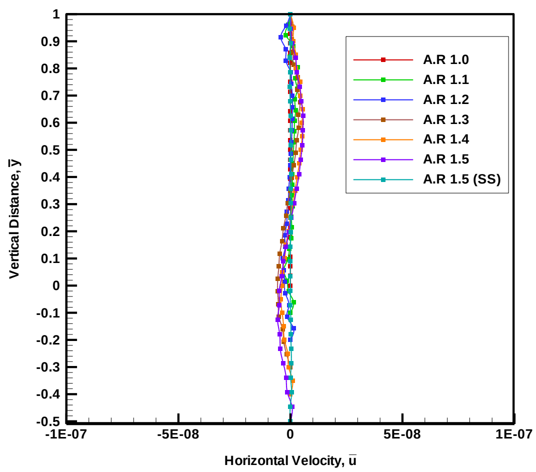

a. User Defined Function

Figure 53 – $\bar{u}$ velocity distribution along centerline vertical distance ($\bar{y} = 0.0$ to 1.0) at $\bar{x}$ = 0.5 for different mesh motion studies. (a. using Layering, b. Using Spring-Based and c. Using UDF)

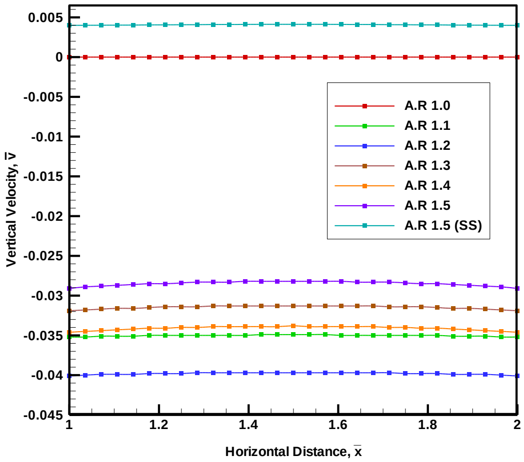

a. Layering

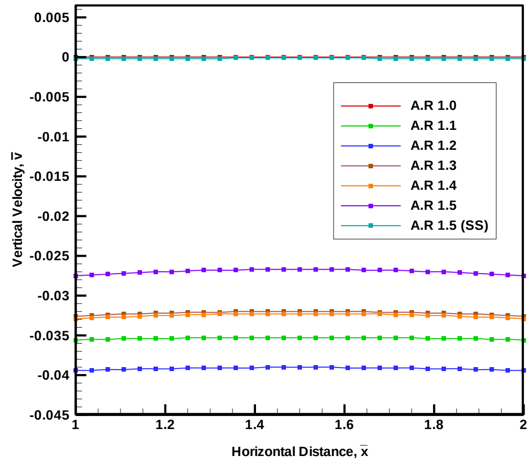

b. Spring-Based

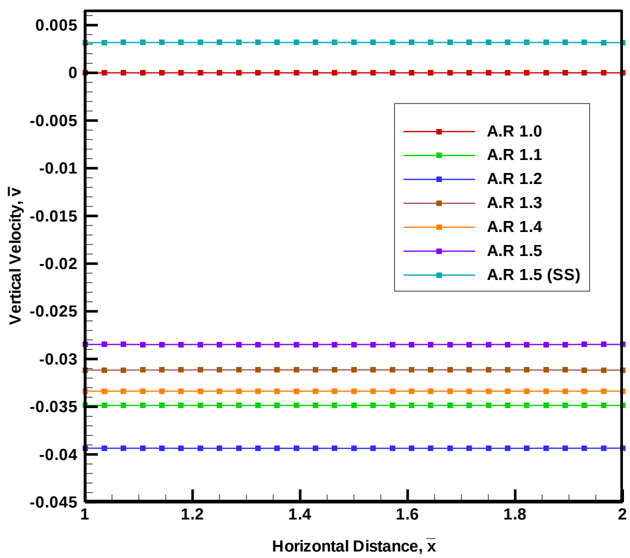

c. User-Defined Function

Figure 54 – $\bar{v}$ velocity distribution along centerline vertical distance ($\bar{x} = 1.0$ to 2.0) at $\bar{x}$ = 0.5 for different mesh motion studies (a. using Layering, b. Using Spring-Based and c. Using UDF)

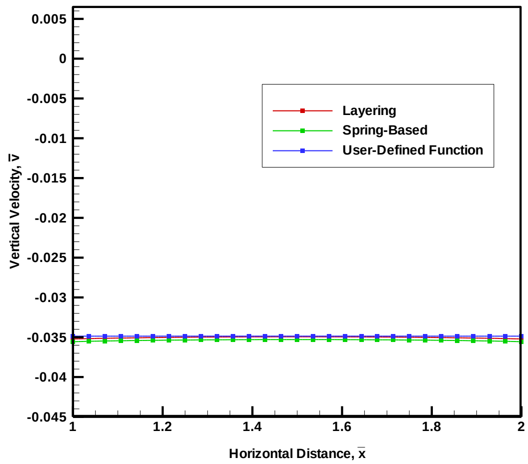

Figure 55 – Comparison of ū velocity distribution along centerline vertical distance for ($\bar{y} = 0.0$ to 1.0) at $\bar{x}$ = 0.5 and time $\bar{t}$ = 12 for different mesh motion studies and A.R 1.1

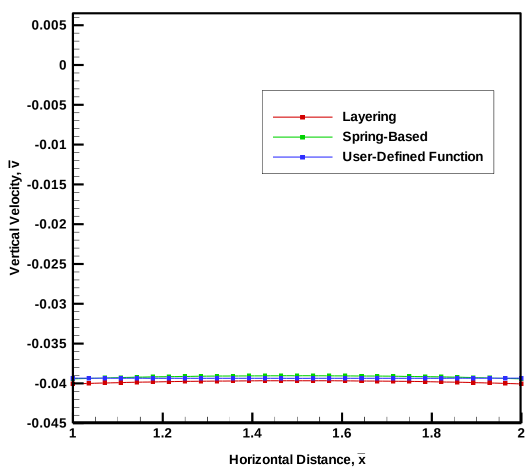

Figure 56 – Comparison of ū velocity distribution along centerline vertical distance for ($\bar{y} = 0.0$ to 1.0) at $\bar{x}$ = 0.5 and time $\bar{t}$ = 14 for different mesh motion studies and A.R 1.2

8. Results of Unsteady Lid Driven Cavity Flow with a Moving Bottom Boundary

In this study a square cavity of *AR* 1.0 is enclosed with a compressible fluid at M = 0.05 and Pr = 1 with adiabatic walls at STP. The side walls of the cavity are stationary at all the times. The lid of the cavity is given a constant velocity u_{lid} = 17.3205 m/s (for Re = 400) and the flow becomes steady state around time t = 0.00106 seconds (in non-dimensional time $\bar{t}$ = 36). Then the bottom boundary of the cavity is moved downwards with a constant speed of v_b = - 0.866 m/s ($\overline{v_b} = -0.05$) from t = 0.00106 seconds to t = 0.001384 seconds (at *AR* 1.5) and the flow becomes steady at time t = 0.0020611 seconds (non-dimensional time $\bar{t}$ = 70) which is also total simulation time. The results indicate that when the lid is moved, the primary circulation center is formed at the upper side of the cavity; then slowly passes through the right corner of the cavity resulting in formation of another secondary circulation cell at the bottom right corner of the cavity. The primary circulation center reaches the center of the cavity and stays there after attaining steady state. When the bottom boundary is moved there is no change in the location of the primary circulation cell but the secondary circulation cell disappears and then appears in small size while the cavity is at *AR* 1.3. The instant the bottom boundary stops moving at *AR* 1.5 the primary circulation moves a little upward from the center of the cavity and the secondary circulation starts growing in size at the bottom of the cavity. After reaching steady state the Primary circulation cell shifts a little towards the right and the secondary circulation cell is formed at the center of the cavity just below the primary circulation.

8.1 Results of Unsteady Lid Driven Cavity Flow using FLUENT

This study is done using commercial CFD package (Fluent) and compared with the results obtained by a numerical method (CMSIP) proposed by AKYUZLU *et.al* [15]. The accuracy of both numerical simulation were verified by comparing the steady state solution of the accepted benchmark case for incompressible flow problems GHIA *et al* [1] that is, the classical problem of driven cavity flow (see section 6.2).

The results obtained using commercial CFD package and CMSIP [15] are in good agreement with each other for AR 1.5 and shown in figures 8.12 through 8.2.2.

A time increment study and grid independence study is done to establish the accuracy of the results for benchmark case using FLUENT and compared with CMSIP results.

A histogram is plotted for u velocity at node x = 0.000255m and y = 0.000346m, shown in figure 57.

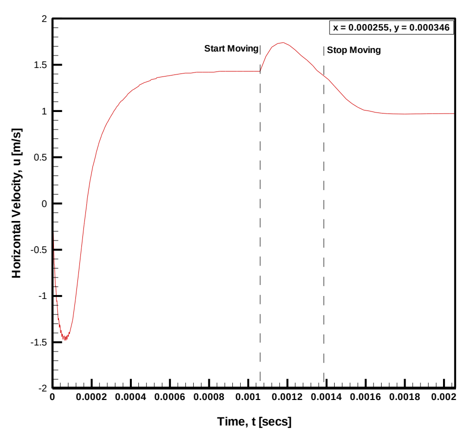

Figure 57.a – Histogram of the Horizontal Velocity (u)

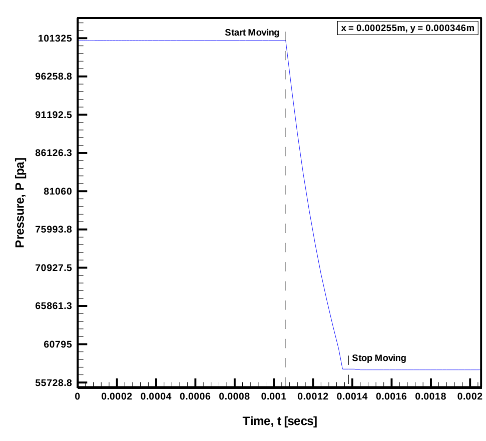

Figure 57.b – Histogram of the Pressure (P)

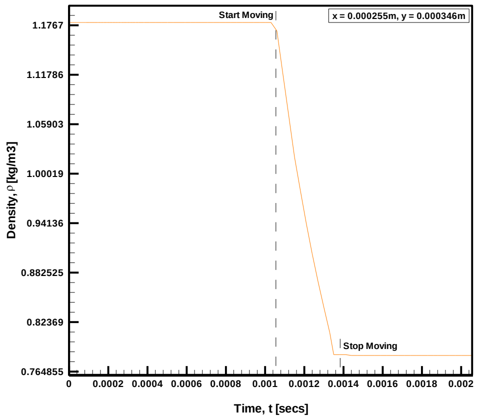

Figure 57.c – Histogram of the Density (ρ)

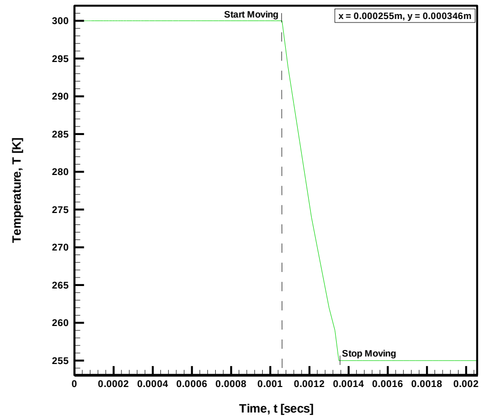

Figure 57.d – Histogram of the Temperature (T)

Figure 57 – Histogram of the primitive variables at $x = 0.000255, y = 0.000346$ before, during, and After the Motion of the Bottom Boundary of the Cavity for AR = 1.5 and Re = 400.

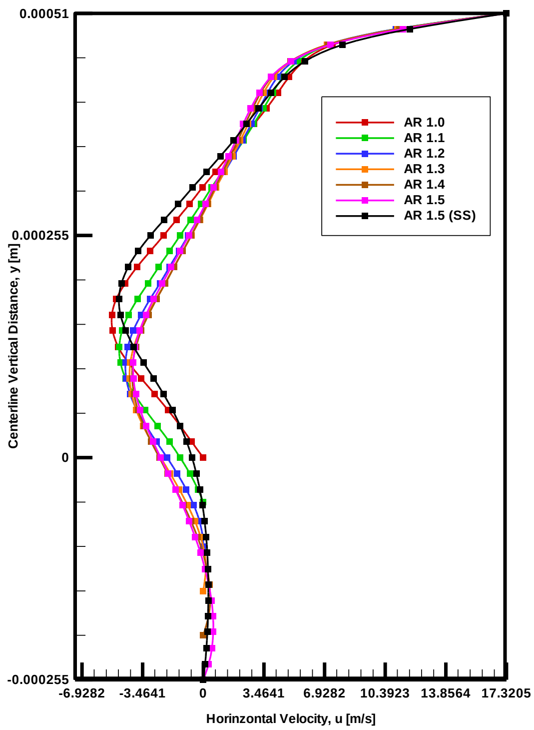

Figure 58 – Horizontal Velocity (u) Distribution along Centerline Vertical Distance (y) for $Re = 400$

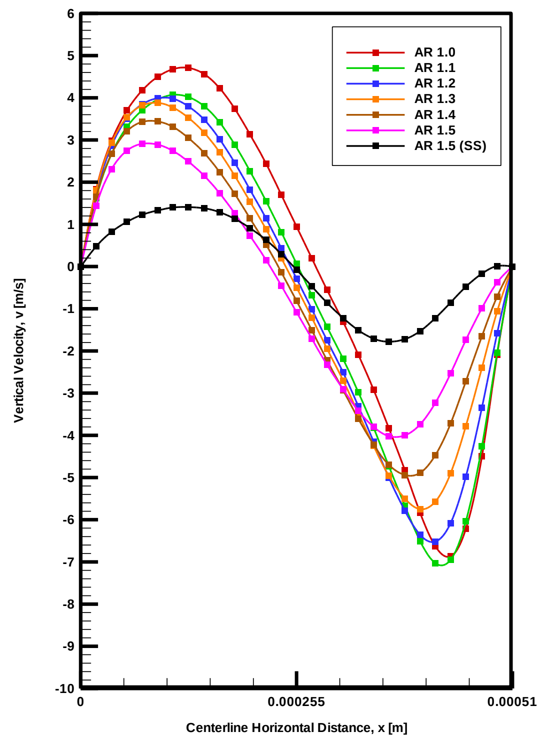

Figure 59 – Vertical Velocity (v) Distribution along Centerline Vertical Distance (x) for $Re = 400$

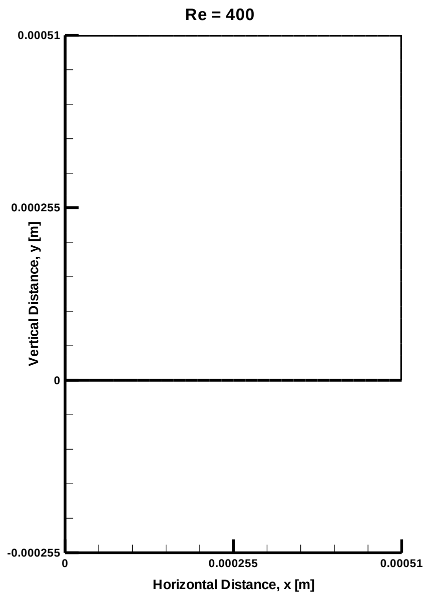

Figure 60 – Vector plot of velocity magnitude at t = 0 sec and *AR* 1.0

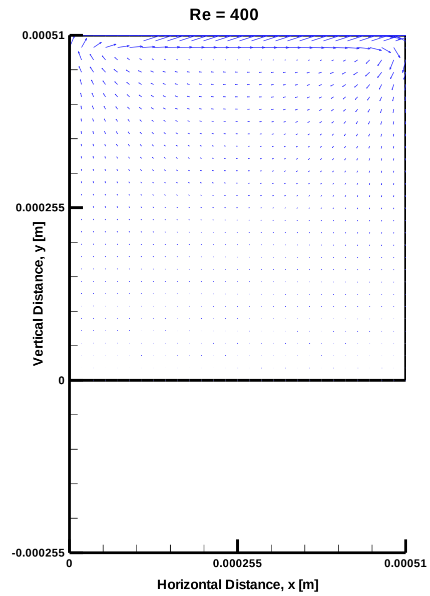

Figure 61 – Vector plot of velocity magnitude at t = 0.0000035 sec and *AR* 1.0

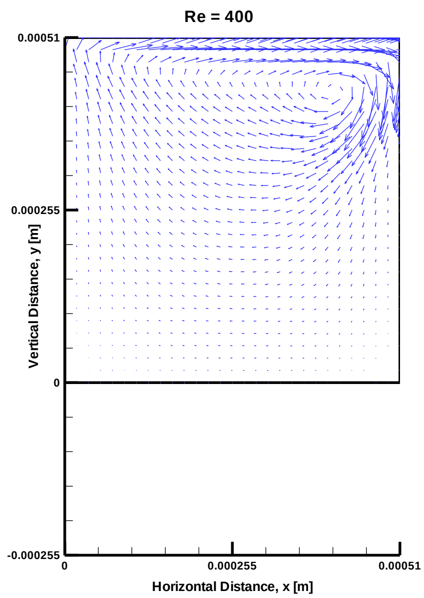

Figure 62 – Vector plot of velocity magnitude at t = 0.0000455 sec and *AR* 1.0

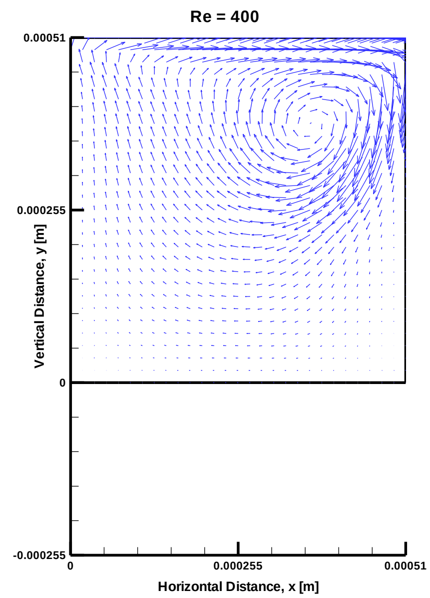

Figure 63 – Vector plot of velocity magnitude at t = 0.000105 sec and *AR* 1.0

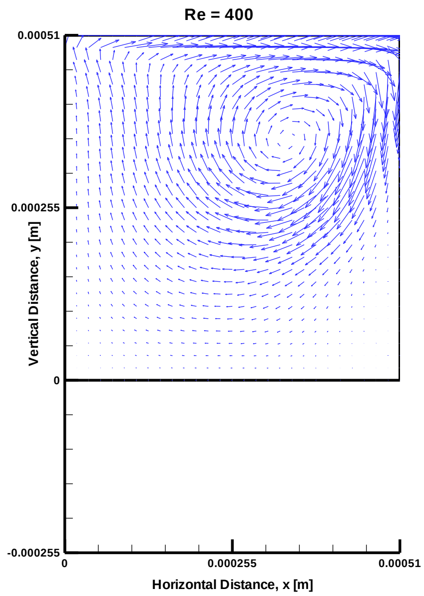

Figure 64 – Vector plot of velocity magnitude at t = 0.000154 sec and *AR* 1.0

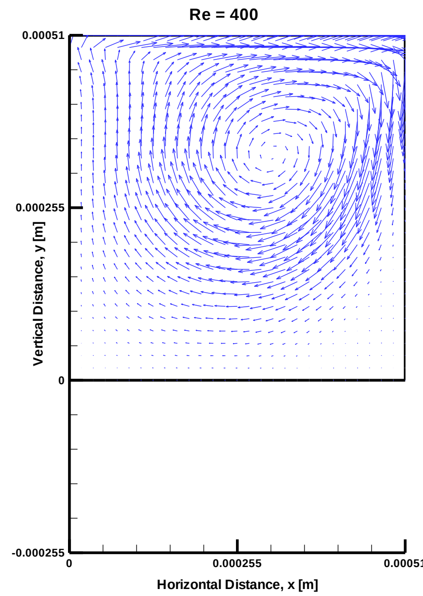

Figure 65 – Vector plot of velocity magnitude at t = 0.0002555 sec and *AR* 1.0

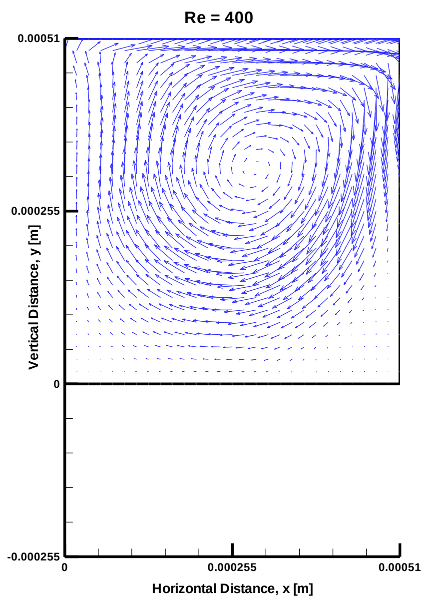

Figure 66 – Vector plot of velocity magnitude at t = 0.0005005 sec and *AR* 1.0

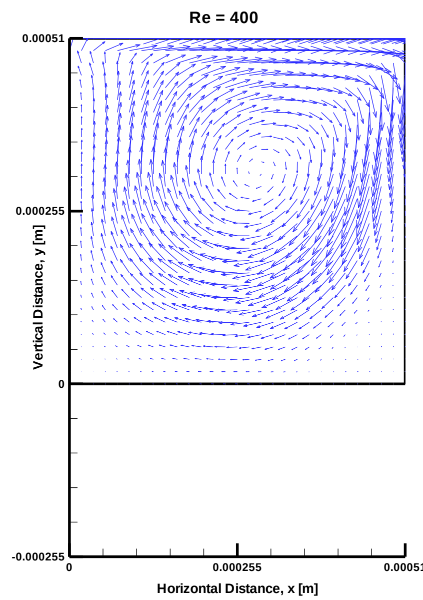

Figure 67 – Vector plot of velocity magnitude at t = 0.00106 sec and *AR* 1.0

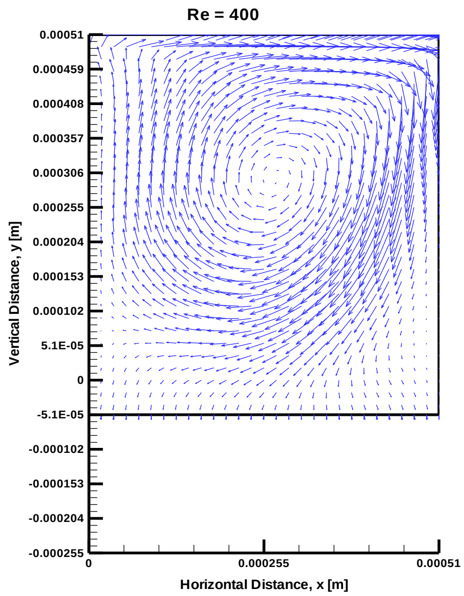

Figure 68 – Vector plot of velocity magnitude at *t* = 0.001119 sec and *AR* 1.1

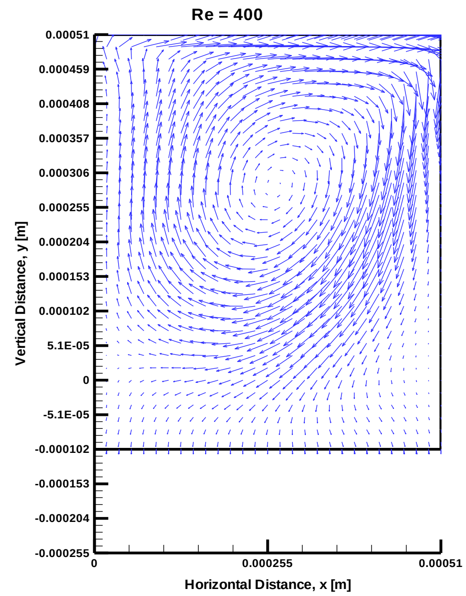

Figure 69 – Vector plot of velocity magnitude at *t* = 0.001178 sec and *AR* 1.2

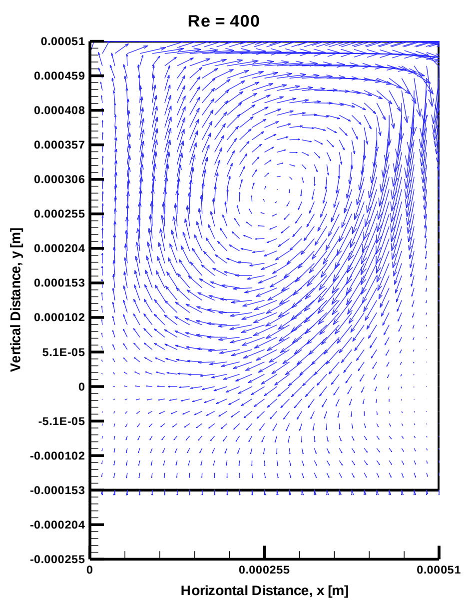

Figure 70 – Vector plot of velocity magnitude at *t* = 0.001237 sec and *AR* 1.3

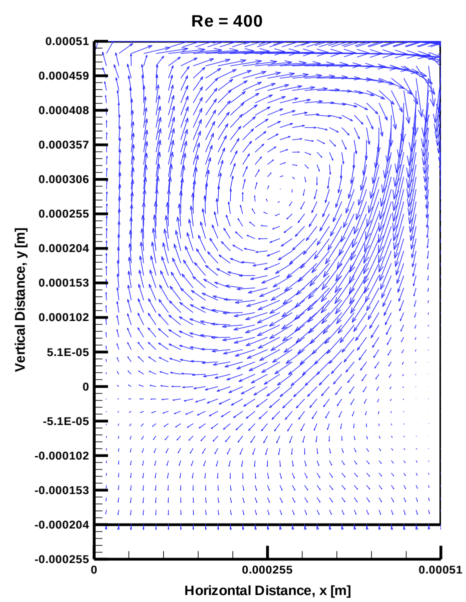

Figure 71 – Vector plot of velocity magnitude at *t* = 0.001295 sec and *AR* 1.4

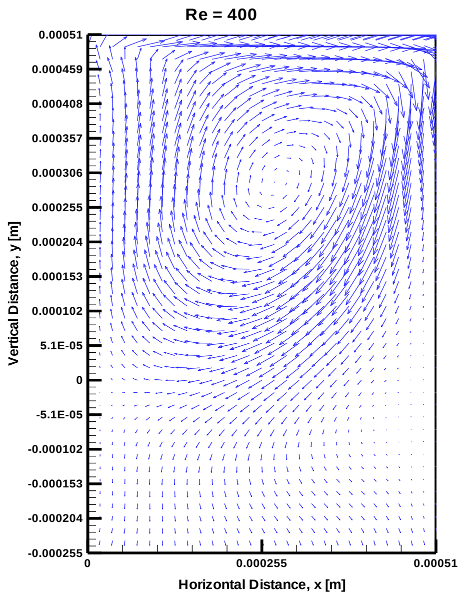

Figure 72 – Vector plot of velocity magnitude at $t = 0.001354$ sec and *AR* 1.5

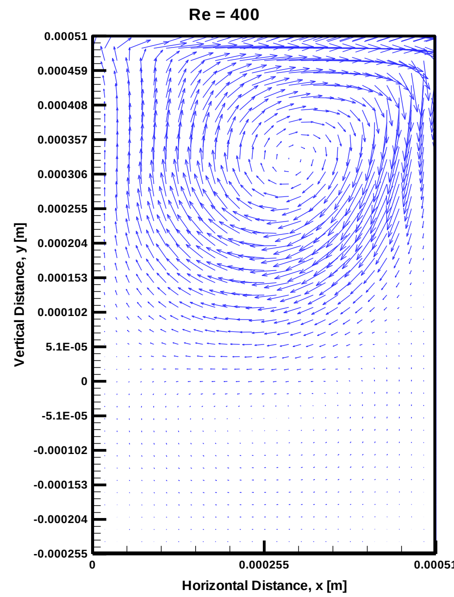

Figure 73 – Vector plot of velocity magnitude at $t = 0.0020611$ sec and *AR* 1.5

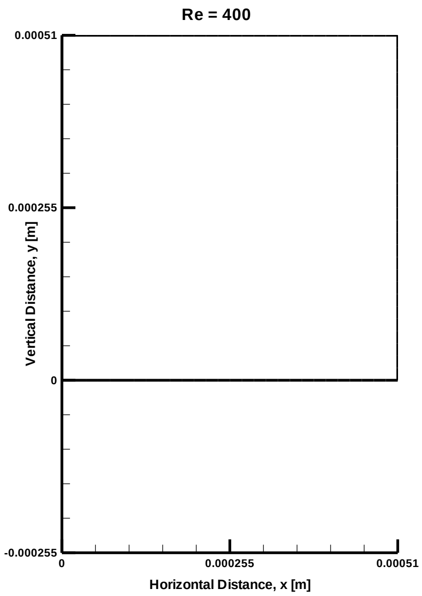

Figure 74 – Streamline plot of velocity magnitude at *t* = 0 sec and *AR* 1.0

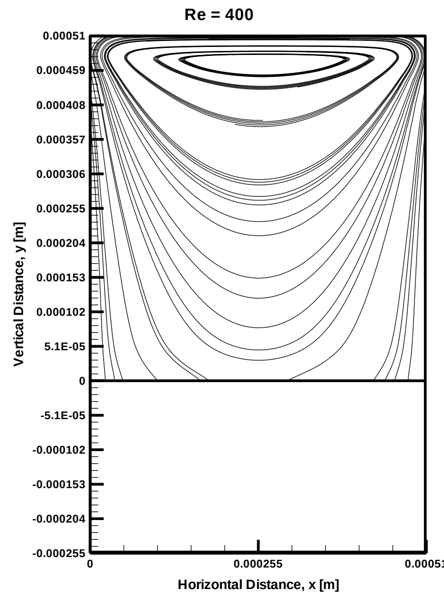

Figure 75 – Streamline plot of velocity magnitude at *t* = 0.0000035 sec and *AR* 1.0

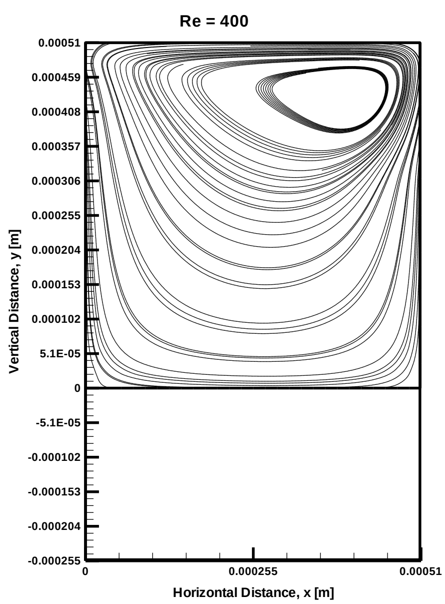

Figure 76 – Streamline plot of velocity magnitude at *t* = 0.0000455 sec and *AR* 1.0

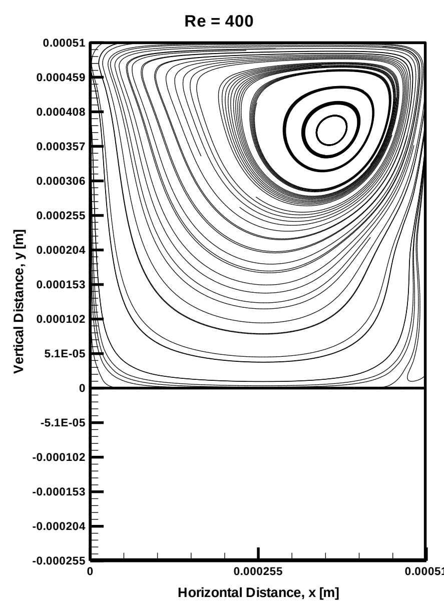

Figure 77 – Streamline plot of velocity magnitude at *t* = 0.000105 sec and *AR* 1.0

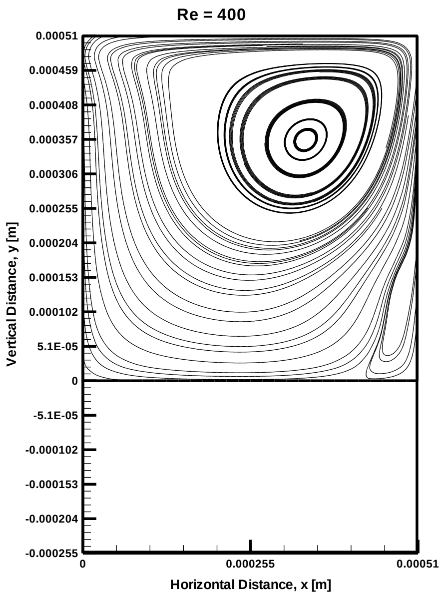

Figure 78 – Streamline plot of velocity magnitude at *t* = 0.000154 sec and *AR* 1.0

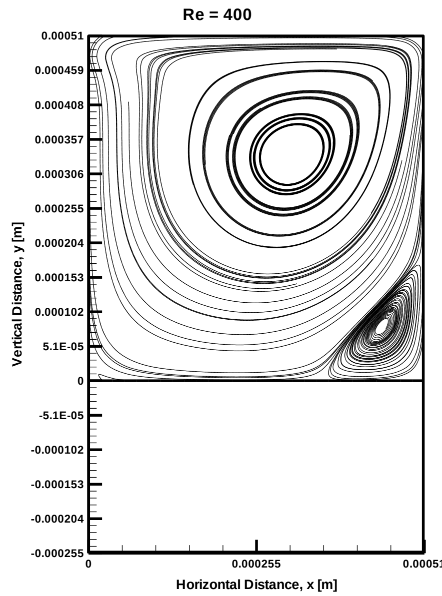

Figure 79 – Streamline plot of velocity magnitude at *t* = 0.0002555 sec and *AR* 1.0

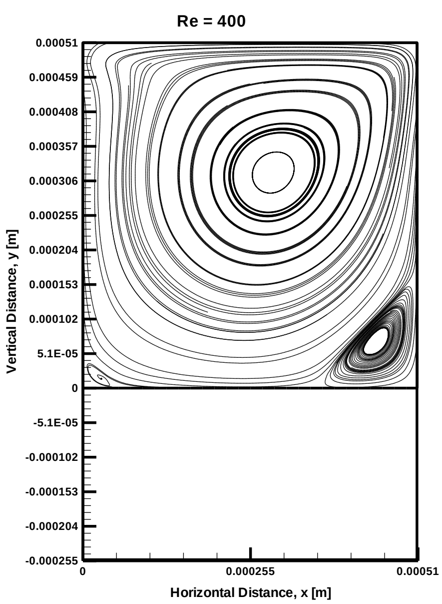

Figure 80 – Streamline plot of velocity magnitude at *t* = 0.0005005 sec and *AR* 1.0

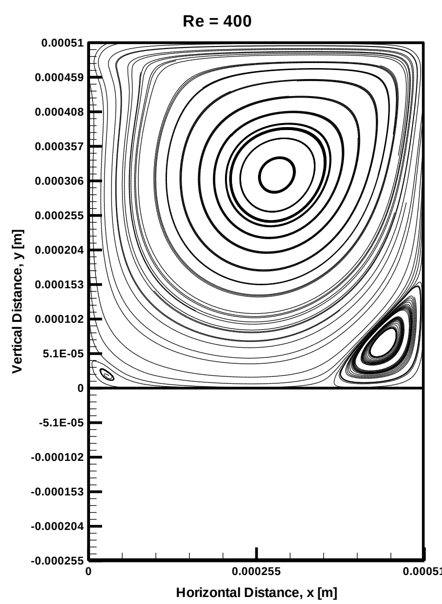

Figure 81 – Streamline plot of velocity magnitude at *t* = 0.00106 sec and *AR* 1.0

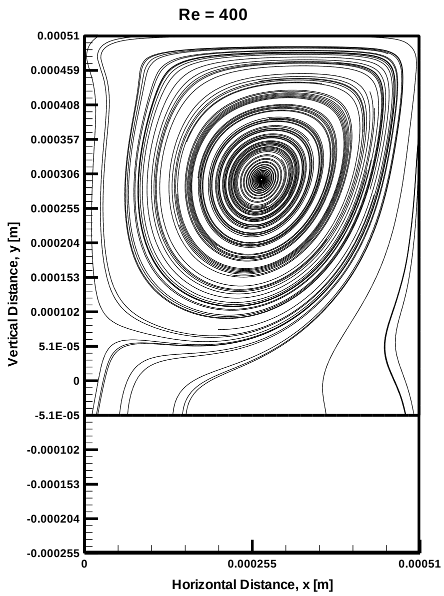

Figure 82 – Streamline plot of velocity magnitude at *t* = 0.001119 sec and *AR* 1.1

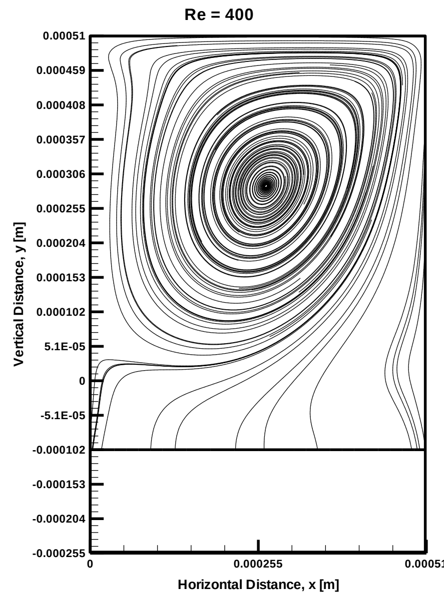

Figure 83 – Streamline plot of velocity magnitude at *t* = 0.001178 sec and *AR* 1.2

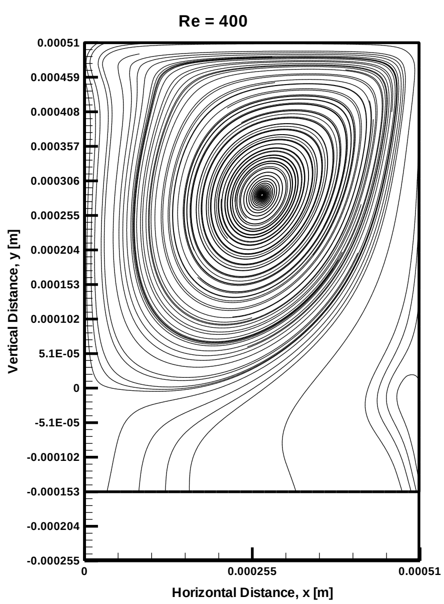

Figure 84 – Streamline plot of velocity magnitude at *t* = 0.001237 sec and *AR* 1.3

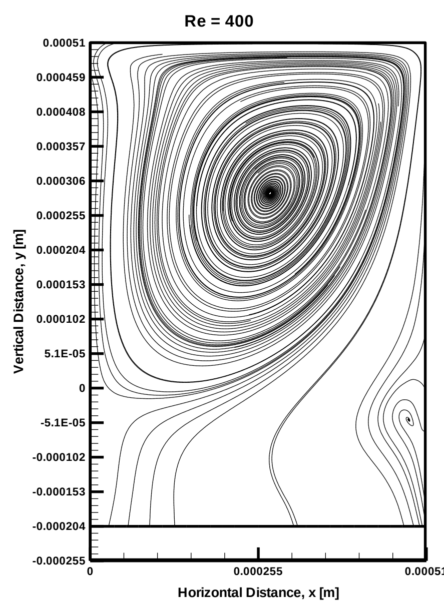

Figure 85 – Streamline plot of velocity magnitude at *t* = 0.001295 sec and *AR* 1.4

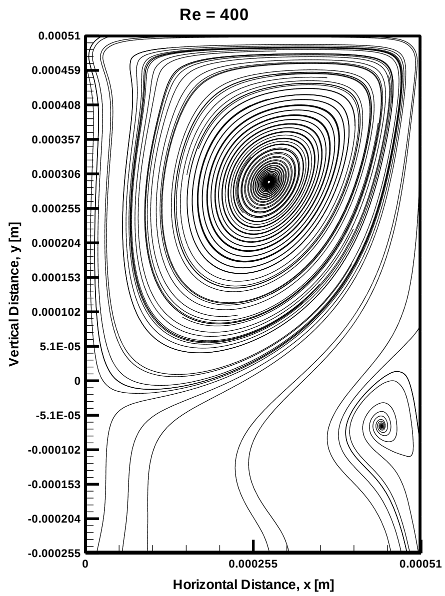

Figure 86 – Streamline plot of velocity magnitude at *t* = 0.001354 sec and *AR* 1.5

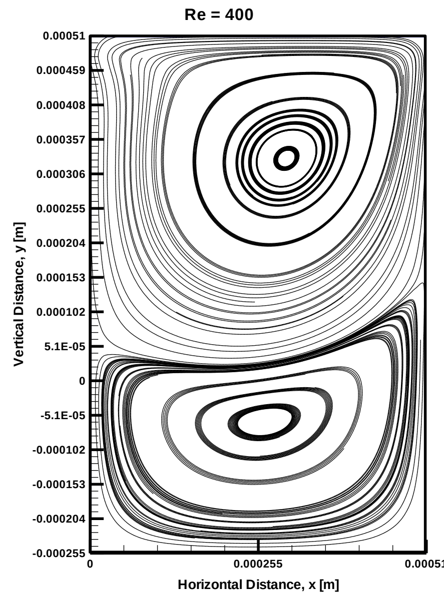

Figure 87 – Streamline plot of velocity magnitude at *t* = 0.0020611 sec and *AR* 1.5

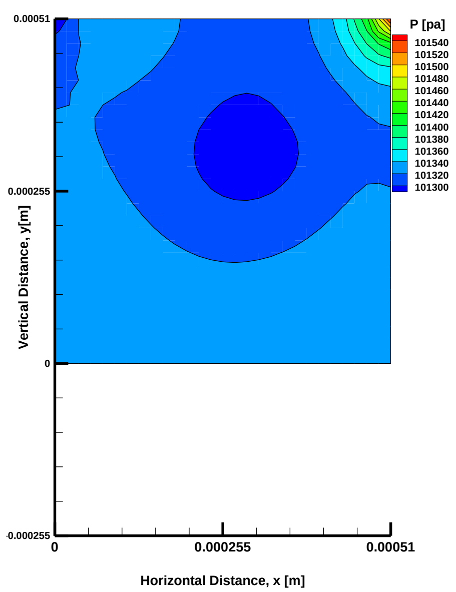

Figure 88 – Pressure Contour at *t* = 0.00106 sec and *AR* 1.0

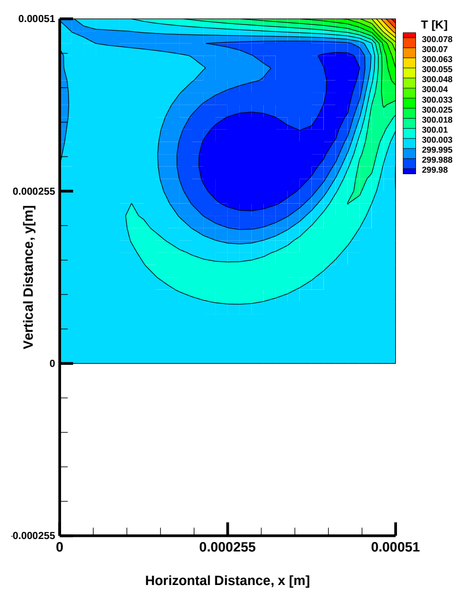

Figure 89 – Temperature Contour at *t* = 0.00106 sec and *AR* 1.0

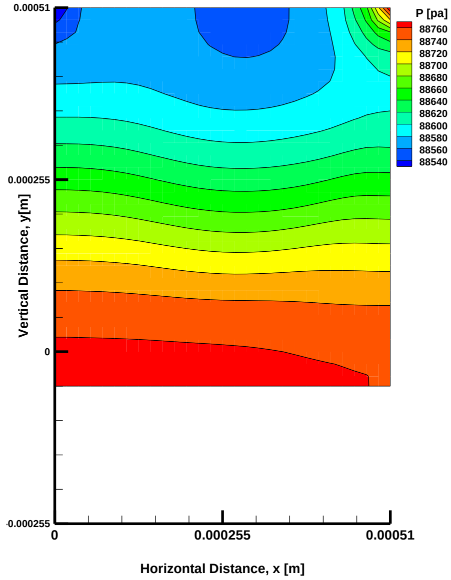

Figure 90 – Pressure Contour at
t = 0.001119 sec and *AR* 1.1

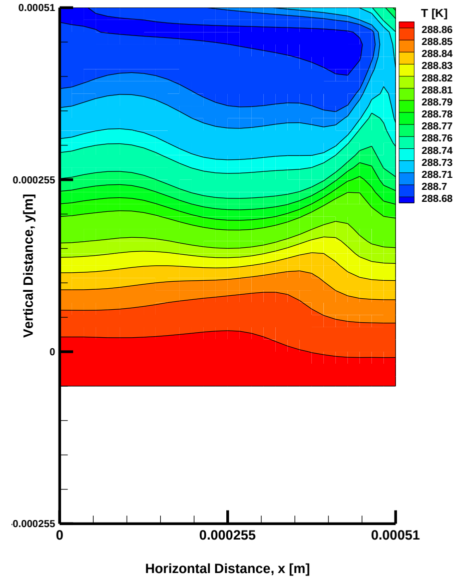

Figure 91 – Temperature Contour at
t = 0.001119 sec and *AR* 1.1

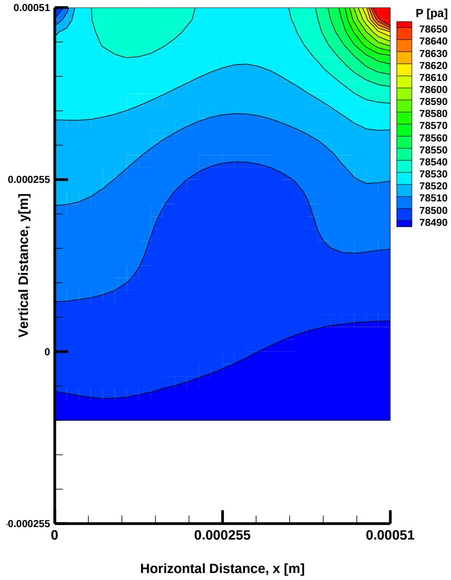

Figure 92 – Pressure Contour at
t = 0.001178 sec and *AR* 1.2

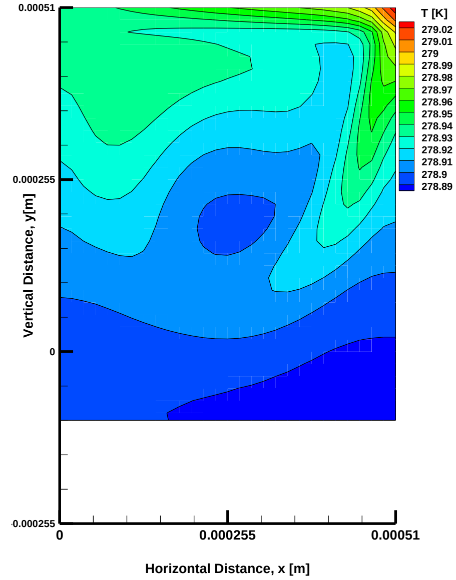

Figure 93 – Temperature Contour at
t = 0.001178 sec and *AR* 1.2

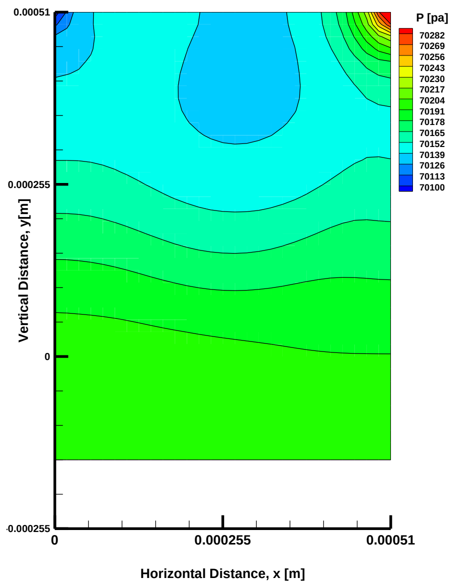

Figure 94 – Pressure Contour at
t = 0.001237 sec and *AR* 1.3

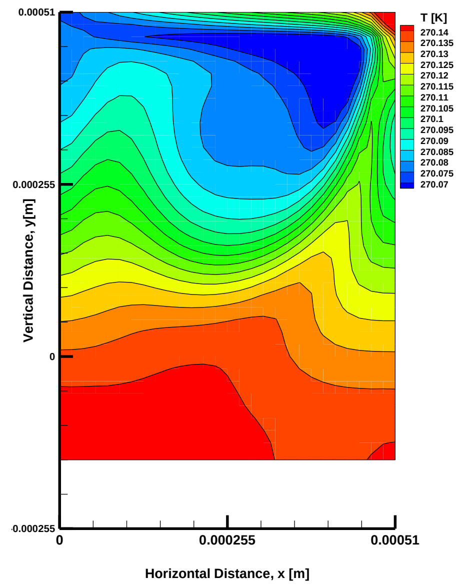

Figure 95 – Temperature Contour at
t = 0.001237 sec and *AR* 1.3

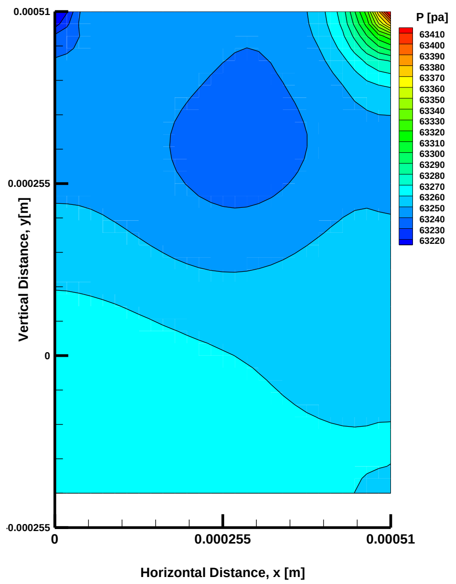

Figure 96 – Pressure Contour at
t = 0.001295 sec and *AR* 1.4

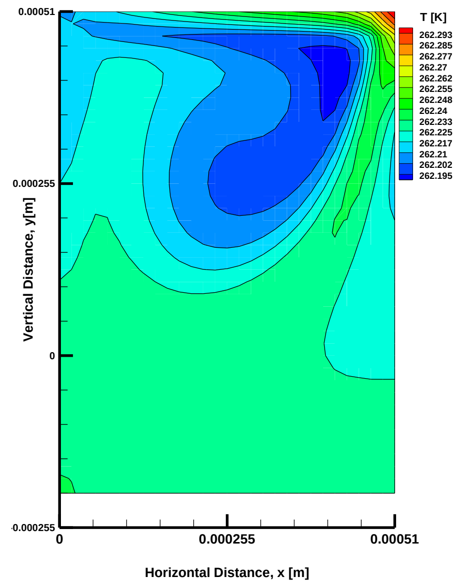

Figure 97 – Temperature Contour at
t = 0.001295 sec and *AR* 1.4

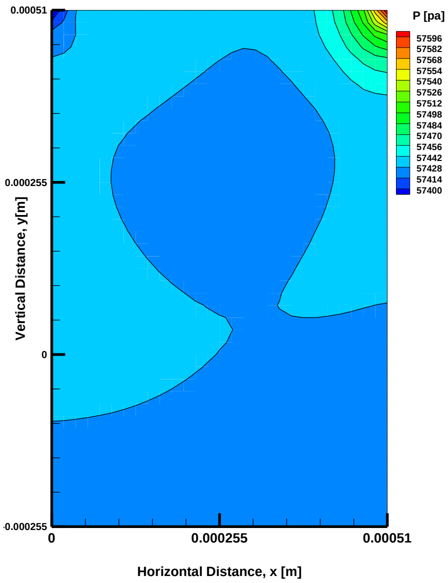

Figure 98 – Pressure Contour at
t = 0.001354 sec and *AR* 1.5

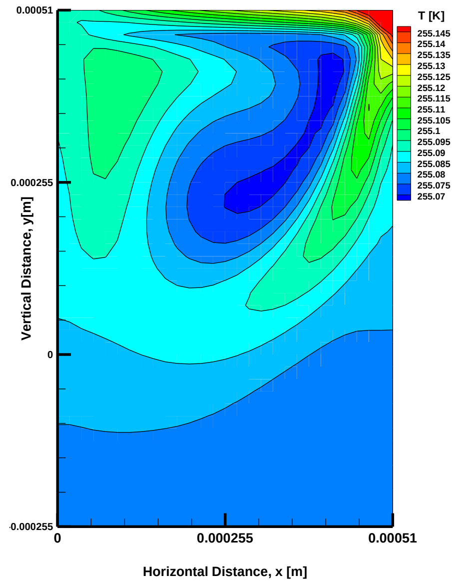

Figure 99 – Temperature Contour at
t = 0.001354 sec and *AR* 1.5

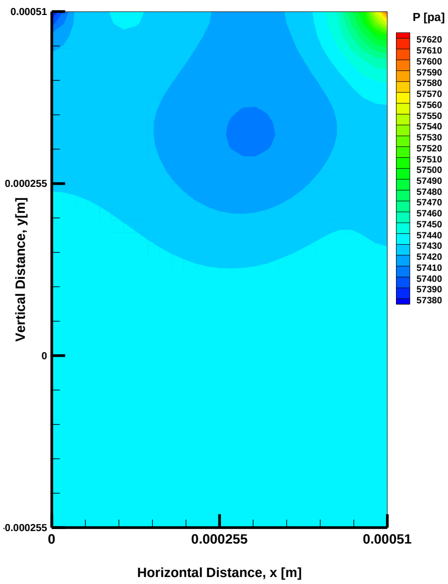

Figure 100 – Pressure Contour at
t = 0.0020611 sec and *AR* 1.5

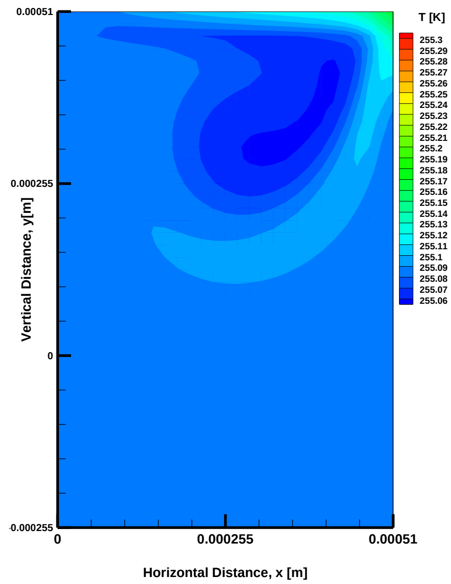

Figure 101 – Temperature Contour at
t = 0.0020611 sec and *AR* 1.5

8.2 Time Increment Independence Study

A time increment study is done for the present study (FLUENT) which is second order accurate in time. A computational time increment of $\Delta t = 0.1 \times 10^{-7}$ is considered. It can be observed that the time increment did not result in any significant changes in qualitative and quantitative results. To proof this the distribution of non-dimensional horizontal velocity ($\bar{u}$) and vertical velocity ($\bar{v}$) are plotted along non-dimensional centerline vertical distance ($\bar{y}$) and centerline horizontal distance ($\bar{x}$) respectively for comparing the results at different aspect ratios using the time increments such as $\Delta t = 0.5 \times 10^{-7}$, $\Delta t = 0.1 \times 10^{-7}$ and $\Delta t = 0.5 \times 10^{-8}$. The quantitative comparison is presented in table 9 and the comparison of horizontal velocity ($\bar{u}$) and vertical velocity ($\bar{v}$) distributions are presented in figure 89 to 92.

Table 9 – Comparison of $\bar{u}$ and $\bar{v}$ velocities for different time increments

Results							
Aspect Ratio	Value	$\Delta t = 0.5 \times 10^{-7}$ $\bar{u}$	$\Delta t = 0.1 \times 10^{-7}$ $\bar{u}$	$\Delta t = 0.5 \times 10^{-8}$ $\bar{u}$	$\Delta t = 0.5 \times 10^{-7}$ $\bar{v}$	$\Delta t = 0.1 \times 10^{-7}$ $\bar{v}$	$\Delta t = 0.5 \times 10^{-8}$ $\bar{v}$
A.R 1.0	max	1.00000	1.00000	1.00000	0.27200	0.27175	0.27163
($\bar{t}$ = 36)	min	-0.30150	-0.30165	-0.30171	-0.39680	-0.39669	-0.39637
A.R 1.1	max	1.00000	1.00000	1.00000	0.24347	0.23492	0.25549
($\bar{t}$ = 38)	min	-0.27705	-0.27716	-0.27719	-0.39765	-0.40603	-0.38506
A.R 1.2	max	1.00000	1.00000	1.00000	0.23991	0.23064	0.23973
($\bar{t}$ = 40)	min	-0.25649	-0.25682	-0.25672	-0.36762	-0.37620	-0.36711
A.R 1.3	max	1.00000	1.00000	1.00000	0.22745	0.22373	0.23511
($\bar{t}$ = 42)	min	-0.24265	-0.24279	-0.24294	-0.32871	-0.33185	-0.32001
A.R 1.4	max	1.00000	1.00000	1.00000	0.20263	0.19873	0.20761
($\bar{t}$ = 44)	min	-0.23434	-0.23448	-0.23449	-0.28223	-0.28543	-0.27614
A.R 1.5	max	1.00000	1.00000	1.00000	0.17122	0.16787	0.17034
($\bar{t}$ = 46)	min	-0.23108	-0.23121	-0.23112	-0.22903	-0.23139	-0.22871
A.R 1.5	max	1.00000	1.00000	1.00000	0.08228	0.08165	0.08193
($\bar{t}$ = 70)	min	-0.27852	-0.27825	-0.27807	-0.10354	-0.10299	-0.10282

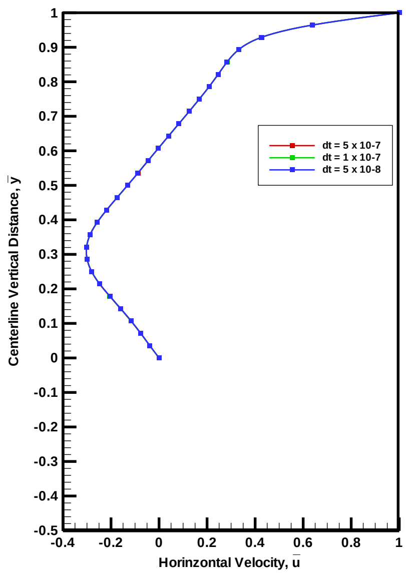

Figure 102 - $\bar{u}$ velocity comparison at $\bar{t} = 35$ and AR 1.0 for different time increments

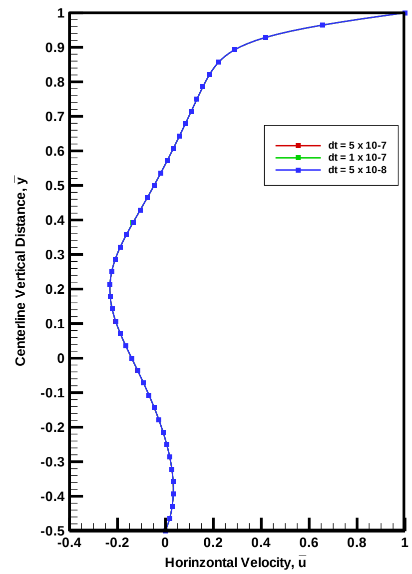

Figure 103 - $\bar{u}$ velocity comparison at $\bar{t} = 46$ and AR 1.5 for different time increments

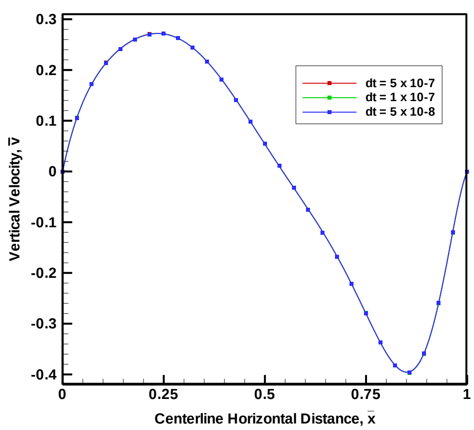

Figure 104 - $\bar{v}$ velocity comparison at $\bar{t} = 35$ and AR 1.0 for different time increments

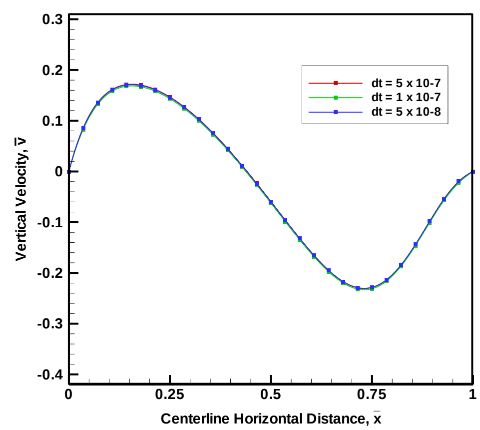

Figure 105 - $\bar{v}$ velocity comparison at $\bar{t} = 46$ and AR 1.5 for different time increments

8.3 Grid Independence Study

In order to validate the accuracy and convergence of the numerical simulation, a grid independence study for the present study (*Re* = 400, M = 0.05, T_i = 300 K, P_o = 101325 Pa and $\bar{v}_b = 0.05$) is also conducted. The grid size chosen for the present study is 29 x 29. To verify that the converged solutions were independent of the grid chosen two more studies were carried out with grid size of 19 x 19, 29 x 29, 41 x 41 , 61 x 61 and 81 x 81. Unsteady state results using uniform, orthogonal 19 x 19, 29 x 29, 41 x 41 , 61 x 61 and 81 x 81 meshes were obtained using the present CFD code (FLUENT).

The distribution of non-dimensional horizontal velocity ($\bar{u}$) and vertical velocity ($\bar{v}$) are plotted along non-dimensional centerline vertical distance ($\bar{y}$) and centerline horizontal distance ($\bar{x}$) respectively for comparing the results at different aspect ratios presented in figure 93 to 96 and the quantitative comparison is presented in table 10 a and b.

Table 10.a – Comparison of $\bar{u}$ velocities for different grid sizes at A.R 1.0 and 1.5

Results						
Aspect Ratio	Value	Mesh Size 19 x 19 $\bar{u}$	Mesh Size 29 x 29 $\bar{u}$	Mesh Size 41 x 41 $\bar{u}$	Mesh Size 61 x 61 $\bar{u}$	Mesh Size 81 x 81 $\bar{u}$
A.R 1.0 ($\bar{t}$ = 36)	max	1.00000	1.00000	1.00000	0.27200	0.27175
	min	-0.26837	-0.29675	-0.30358	-0.30520	-0.30637
A.R 1.5 ($\bar{t}$ = 46)	max	1.00000	1.00000	1.00000	0.17122	0.16787
	min	-0.21326	-0.22966	-0.23493	-0.23726	-0.23874

Table 10.b - Comparison of $\bar{v}$ velocities for different grid sizes at A.R 1.0 and 1.5

Results						
Aspect Ratio	Value	Mesh Size 19 x 19 $\bar{v}$	Mesh Size 29 x 29 $\bar{v}$	Mesh Size 41 x 41 $\bar{v}$	Mesh Size 61 x 61 $\bar{v}$	Mesh Size 81 x 81 $\bar{v}$
A.R 1.0 ($\bar{t}$ = 36)	max	0.23378	0.27067	0.28853	0.29624	0.30015
	min	-0.33454	-0.38722	-0.41296	-0.42395	-0.42912
A.R 1.5 ($\bar{t}$ = 46)	max	0.13992	0.16735	0.18308	0.19079	0.19364
	min	-0.20029	-0.23178	-0.24847	-0.25541	-0.25934

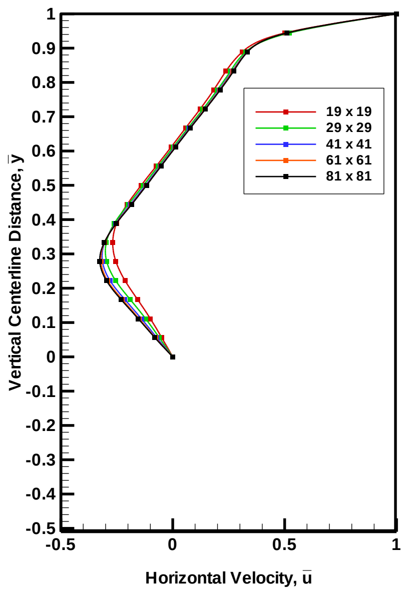

Figure 106 - $\bar{u}$ velocity comparison at $\bar{t} = 35$ and AR 1.0 for different grid sizes

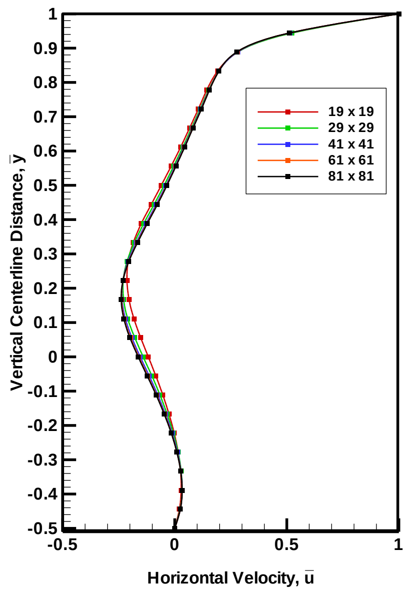

Figure 107 - $\bar{u}$ velocity comparison at $\bar{t} = 46$ and AR 1.5 for different grid sizes

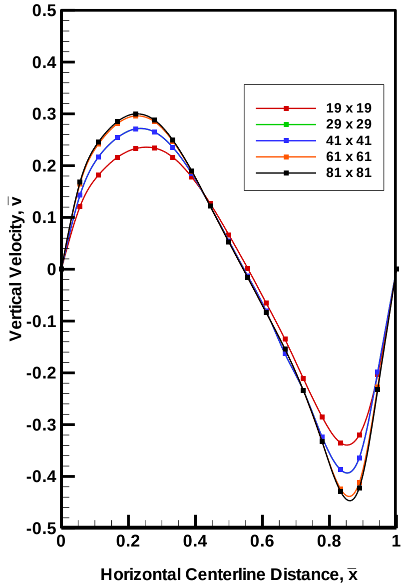

Figure 108 - $\bar{v}$ velocity comparison at $\bar{t} = 35$ and AR 1.0 for different grid sizes

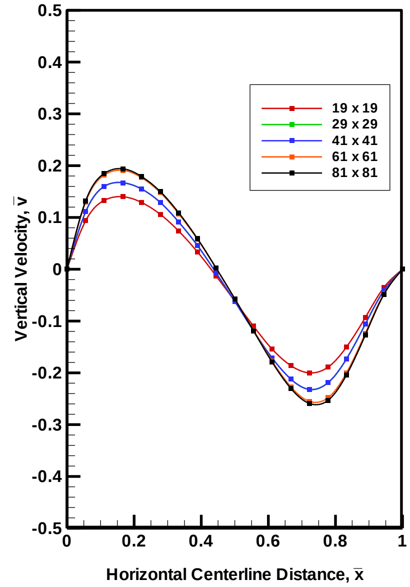

Figure 109 - $\bar{v}$ velocity comparison at $\bar{t} = 46$ and AR 1.5 for different grid sizes

8.4 Comparison of Present Results (FLUENT) with CMSIP Results

The results obtained from FLUENT for the present case with mesh size Δx = 29 x 29 and time increment of $\Delta t = 1 \times 10^{-7}$ is compared with the results of CMSIP [1] for the distribution of non-dimensional horizontal velocity ($\bar{u}$) and vertical velocity ($\bar{v}$) are plotted along non-dimensional centerline vertical distance ($\bar{y}$) and centerline horizontal distance ($\bar{x}$) respectively at different aspect ratios presented in figure 97 to 104 and the quantitative comparison is presented in table 11 to 14 . Also contours of pressure and temperature, vector, and streamline plot of velocity magnitude are compared at different aspect ratios. It is observed that the results are in good agreement with each other and captures all the circulation of fluid inside the cavity perfectly.

The results indicate the formation of a primary circulation cell developing at the center of the cavity with secondary (small) circulation patterns (vortices) developing at the bottom corners of the cavity. During the downward displacement of the bottom (of the cavity), the lower right vortex moves to the center while growing in strength and size resulting in a secondary circulation cell just below the primary one shown in figure 112.

Table 11 – Comparison of distribution of $\bar{u}$ velocity at AR 1.0 and 1.1 for FLUENT and CMSIP.

AR 1.0				AR 1.1			
$\bar{y}$	CMSIP $\bar{u}$	FLUENT $\bar{u}$	dev %	$\bar{y}$	CMSIP $\bar{u}$	FLUENT $\bar{u}$	dev %
1.0000	1.00000	1.00000	0.00	1.0000	1.00000	1.00000	0.00
0.9644	0.62288	0.63894	2.58	0.9607	0.59289	0.61320	3.43
0.9287	0.40666	0.42663	4.91	0.9214	0.37037	0.39413	6.42
0.8930	0.30899	0.33132	7.23	0.8821	0.27391	0.29698	8.42
0.8572	0.26345	0.28318	7.49	0.8429	0.23089	0.24921	7.93
0.8215	0.22990	0.24606	7.03	0.8036	0.19983	0.21403	7.11
0.7858	0.19538	0.20834	6.64	0.7643	0.16835	0.17934	6.53
0.7501	0.15773	0.16796	6.49	0.7250	0.13407	0.14276	6.48
0.7143	0.11850	0.12570	6.08	0.6857	0.09879	0.10469	5.97
0.6786	0.07794	0.08258	5.96	0.6464	0.06224	0.06603	6.08
0.6429	0.03766	0.03959	5.11	0.6071	0.02626	0.02742	4.42
0.6072	-0.00288	-0.00306	6.07	0.5679	-0.01010	-0.01075	6.46
0.5714	-0.04285	-0.04559	6.40	0.5286	-0.04577	-0.04867	6.33
0.5357	-0.08339	-0.08812	5.68	0.4893	-0.08208	-0.08676	5.70
0.5000	-0.12393	-0.13124	5.91	0.4500	-0.11830	-0.12547	6.06
0.4643	-0.16488	-0.17510	6.20	0.4107	-0.15499	-0.16468	6.26
0.4286	-0.20416	-0.21820	6.88	0.3714	-0.19008	-0.20310	6.85
0.3928	-0.23948	-0.25726	7.42	0.3321	-0.22155	-0.23768	7.28
0.3571	-0.26612	-0.28699	7.85	0.2929	-0.24492	-0.26371	7.67
0.3214	-0.28033	-0.30165	7.60	0.2536	-0.25674	-0.27623	7.59
0.2857	-0.27906	-0.29928	7.25	0.2143	-0.25405	-0.27310	7.50
0.2499	-0.26296	-0.28046	6.66	0.1750	-0.23746	-0.25337	6.70
0.2142	-0.23457	-0.24708	5.33	0.1357	-0.20928	-0.22042	5.33
0.1785	-0.19881	-0.20472	2.97	0.0964	-0.17410	-0.17934	3.01
0.1428	-0.15980	-0.15971	0.06	0.0571	-0.13602	-0.13584	0.13
0.1070	-0.12099	-0.11641	3.79	0.0179	-0.09884	-0.09433	4.56
0.0713	-0.08260	-0.07636	7.56	-0.0214	-0.06385	-0.05722	10.38
0.0356	-0.04358	-0.03850	11.65	-0.0607	-0.03160	-0.02659	15.87
0.0000	0.00000	0.00000	0.00	-0.1000	0.00000	0.00000	0.00

Table 12 – Comparison of distribution of $\bar{u}$ velocity at *AR* 1.5 and 1.5 (steady state) for FLUENT and CMSIP.

AR 1.5				*AR* 1.5 (Steady State)			
$\bar{y}$	CMSIP $\bar{u}$	FLUENT $\bar{u}$	dev %	$\bar{y}$	CMSIP $\bar{u}$	FLUENT $\bar{u}$	dev %
1.0000	1.00000	1.00000	0.00	1.0000	1.00000	1.00000	0.00
0.9464	0.51626	0.53616	0.04	0.9464	0.54318	0.55208	0.02
0.8929	0.28053	0.28899	0.03	0.8929	0.31911	0.30182	0.05
0.8393	0.18706	0.20351	0.09	0.8393	0.22587	0.24826	0.10
0.7857	0.14538	0.15657	0.08	0.7857	0.17219	0.16443	0.05
0.7321	0.11223	0.11967	0.07	0.7321	0.11884	0.12211	0.03
0.6786	0.08021	0.08312	0.04	0.6786	0.06198	0.03275	0.47
0.6250	0.04525	0.04565	0.01	0.6250	-0.00053	-0.01387	25.08
0.5714	0.01033	0.00705	0.32	0.5714	-0.06420	-0.10917	0.70
0.5179	-0.02781	-0.03354	0.21	0.5179	-0.12919	-0.15639	0.21
0.4643	-0.06640	-0.07607	0.15	0.4643	-0.18628	-0.19124	0.03
0.4107	-0.10687	-0.12014	0.12	0.4107	-0.22775	-0.25548	0.12
0.3571	-0.14452	-0.16314	0.13	0.3571	-0.24381	-0.27096	0.11
0.3036	-0.17674	-0.19923	0.13	0.3036	-0.23583	-0.26225	0.11
0.2500	-0.19746	-0.22428	0.14	0.2500	-0.20858	-0.24079	0.15
0.1964	-0.20479	-0.23083	0.13	0.1964	-0.17184	-0.17930	0.04
0.1429	-0.19776	-0.22243	0.12	0.1429	-0.13248	-0.14657	0.11
0.0893	-0.17960	-0.19812	0.10	0.0893	-0.09637	-0.08877	0.08
0.0357	-0.15355	-0.16544	0.08	0.0357	-0.06559	-0.06547	0.00
-0.0179	-0.12381	-0.12844	0.04	-0.0179	-0.04119	-0.03004	0.27
-0.0714	-0.09306	-0.09164	0.02	-0.0714	-0.02250	-0.01716	0.24
-0.1250	-0.06360	-0.05768	0.09	-0.1250	-0.00891	0.00105	1.12
-0.1786	-0.03669	-0.02719	0.26	-0.1786	0.00061	0.00711	10.63
-0.2321	-0.01347	-0.00205	0.85	-0.2321	0.00673	0.01451	1.16
-0.2857	0.00500	0.01784	2.57	-0.2857	0.01007	0.01623	0.61
-0.3393	0.01751	0.02951	0.69	-0.3393	0.01100	0.01630	0.48
-0.3929	0.02235	0.03278	0.47	-0.3929	0.00967	0.01475	0.52
-0.4464	0.01748	0.02296	0.31	-0.4464	0.00611	0.00833	0.36
-0.5000	0.00000	0.00000	0.00	-0.5000	0.00000	0.00000	0.00

Table 13 – Comparison of distribution of $\bar{v}$ velocity at AR 1.0 and 1.1 for FLUENT and CMSIP.

AR 1.0				AR 1.1			
$\bar{x}$	CMSIP $\bar{v}$	FLUENT $\bar{v}$	dev %	$\bar{x}$	CMSIP $\bar{v}$	FLUENT $\bar{v}$	dev %
1.0000	0.00000	0.00000	0.00	1.0000	0.00000	0.00000	0.00
0.9643	-0.11144	-0.12048	-0.08	0.9643	-0.09057	-0.11774	-0.30
0.9286	-0.27436	-0.25975	0.05	0.9286	-0.23533	-0.24587	-0.04
0.8929	-0.37094	-0.35928	0.03	0.8929	-0.34254	-0.34850	-0.02
0.8571	-0.38957	-0.39669	-0.02	0.8571	-0.38360	-0.40138	-0.05
0.8214	-0.36189	-0.38253	-0.06	0.8214	-0.37457	-0.40603	-0.08
0.7857	-0.31267	-0.33706	-0.08	0.7857	-0.33805	-0.37593	-0.11
0.7500	-0.25813	-0.27900	-0.08	0.7500	-0.28996	-0.32728	-0.13
0.7143	-0.20494	-0.22118	-0.08	0.7143	-0.23962	-0.27309	-0.14
0.6786	-0.15620	-0.16839	-0.08	0.6786	-0.19133	-0.22065	-0.15
0.6429	-0.11065	-0.12044	-0.09	0.6429	-0.14574	-0.17201	-0.18
0.6071	-0.06789	-0.07556	-0.11	0.6071	-0.10255	-0.12645	-0.23
0.5714	-0.02593	-0.03198	-0.23	0.5714	-0.06052	-0.08262	-0.37
0.5357	0.01537	0.01128	0.27	0.5357	-0.01908	-0.03938	-1.06
0.5000	0.05682	0.05473	0.04	0.5000	0.02229	0.00386	0.83
0.4643	0.09774	0.09818	0.00	0.4643	0.06341	0.04712	0.26
0.4286	0.13747	0.14077	-0.02	0.4286	0.10347	0.08976	0.13
0.3929	0.17437	0.18084	-0.04	0.3929	0.14130	0.13041	0.08
0.3571	0.20643	0.21611	-0.05	0.3571	0.17480	0.16707	0.04
0.3214	0.23175	0.24420	-0.05	0.3214	0.20236	0.19749	0.02
0.2857	0.24841	0.26307	-0.06	0.2857	0.22184	0.21961	0.01
0.2500	0.25604	0.27175	-0.06	0.2500	0.23281	0.23214	0.00
0.2143	0.25435	0.27035	-0.06	0.2143	0.23468	0.23492	0.00
0.1786	0.24499	0.25981	-0.06	0.1786	0.22892	0.22863	0.00
0.1429	0.22820	0.24123	-0.06	0.1429	0.21571	0.21423	0.01
0.1071	0.20363	0.21382	-0.05	0.1071	0.19506	0.19110	0.02
0.0714	0.16521	0.17232	-0.04	0.0714	0.16141	0.15442	0.04
0.0357	0.10255	0.10561	-0.03	0.0357	0.10510	0.09372	0.11
0.0000	0.00000	0.00000	0.00	0.0000	0.00000	0.00000	0.00

Table 14 – Comparison of distribution of $\bar{v}$ velocity at AR 1.5 and 1.5 (steady state) for FLUENT and CMSIP.

AR 1.5				AR 1.5 (Steady State)			
$\bar{x}$	CMSIP $\bar{v}$	FLUENT $\bar{v}$	dev %	$\bar{x}$	CMSIP $\bar{v}$	FLUENT $\bar{v}$	dev %
1.0000	0.00000	0.00000	0.00	1.0000	0.00000	0.00000	0.00
0.9643	-0.02318	-0.02175	0.06	0.9643	-0.00131	0.00068	1.52
0.9286	-0.06123	-0.05683	0.07	0.9286	-0.01580	-0.00966	0.39
0.8929	-0.10876	-0.10058	0.08	0.8929	-0.03923	-0.02754	0.30
0.8571	-0.15693	-0.14607	0.07	0.8571	-0.06647	-0.04918	0.26
0.8214	-0.19578	-0.18633	0.05	0.8214	-0.09089	-0.07058	0.22
0.7857	-0.22015	-0.21577	0.02	0.7857	-0.10830	-0.08822	0.19
0.7500	-0.22862	-0.23115	-0.01	0.7500	-0.11615	-0.09948	0.14
0.7143	-0.22326	-0.23190	-0.04	0.7143	-0.11470	-0.10299	0.10
0.6786	-0.20682	-0.21965	-0.06	0.6786	-0.10495	-0.09859	0.06
0.6429	-0.18261	-0.19736	-0.08	0.6429	-0.08888	-0.08716	0.02
0.6071	-0.15317	-0.16810	-0.10	0.6071	-0.06828	-0.07024	-0.03
0.5714	-0.12074	-0.13451	-0.11	0.5714	-0.04514	-0.04962	-0.10
0.5357	-0.08677	-0.09875	-0.14	0.5357	-0.02099	-0.02710	-0.29
0.5000	-0.05251	-0.06227	-0.19	0.5000	0.00259	-0.00435	2.68
0.4643	-0.01867	-0.02610	-0.40	0.4643	0.02455	0.01720	0.30
0.4286	0.01391	0.00893	0.36	0.4286	0.04383	0.03644	0.17
0.3929	0.04477	0.04213	0.06	0.3929	0.05994	0.05262	0.12
0.3571	0.07309	0.07285	0.00	0.3571	0.07238	0.06528	0.10
0.3214	0.09848	0.10045	-0.02	0.3214	0.08125	0.07426	0.09
0.2857	0.12011	0.12428	-0.03	0.2857	0.08659	0.07963	0.08
0.2500	0.13769	0.14374	-0.04	0.2500	0.08885	0.08165	0.08
0.2143	0.15043	0.15823	-0.05	0.2143	0.08826	0.08070	0.09
0.1786	0.15781	0.16690	-0.06	0.1786	0.08512	0.07707	0.09
0.1429	0.15807	0.16815	-0.06	0.1429	0.07916	0.07080	0.11
0.1071	0.14859	0.15880	-0.07	0.1071	0.06957	0.06137	0.12
0.0714	0.12406	0.13316	-0.07	0.0714	0.05477	0.04753	0.13
0.0357	0.07753	0.08291	-0.07	0.0357	0.03234	0.02750	0.15
0.0000	0.00000	0.00000	0.00	0.0000	0.00000	0.00000	0.00

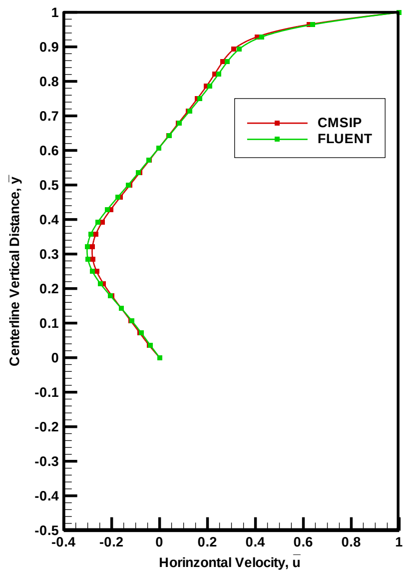

Figure 110– Comparison of $\bar{u}$ velocity between CMSIP and FLUENT at $\bar{t} = 35$ and *AR* 1.0

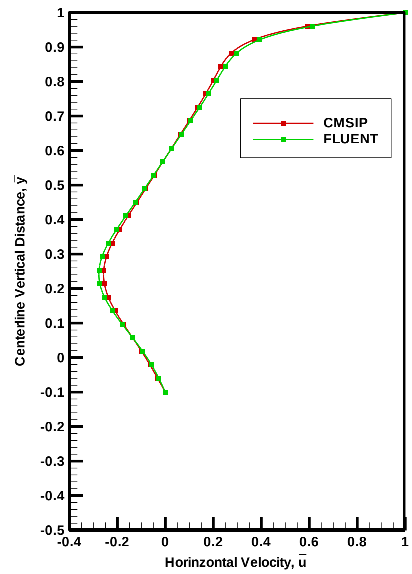

Figure 111– Comparison of $\bar{u}$ velocity between CMSIP and FLUENT at $\bar{t} = 38$ and *AR* 1.1

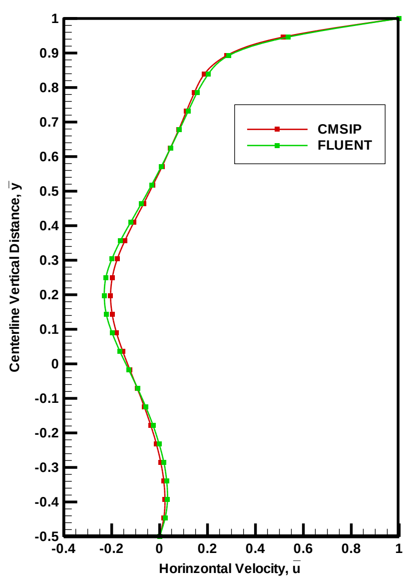

Figure 112– comparison of $\bar{u}$ velocity between CMSIP and FLUENT at $\bar{t} = 46$ and *AR* 1.5

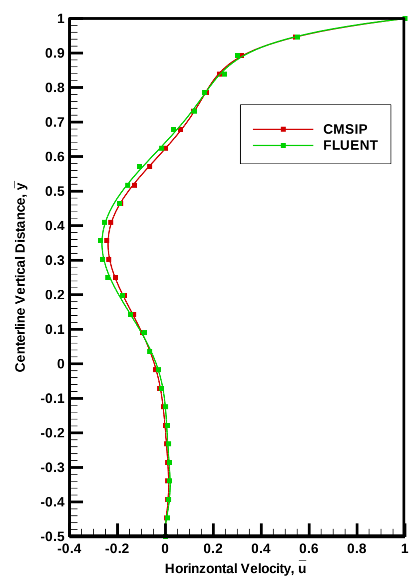

Figure 113 – comparison of $\bar{u}$ velocity between CMSIP and FLUENT at $\bar{t} = 70$ and *AR* 1.5

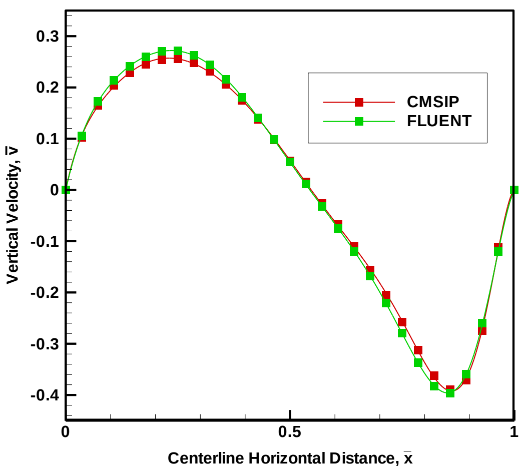

Figure 114 – Comparison of $\bar{v}$ velocity between CMSIP and FLUENT at $\bar{t} = 35$ and AR 1.0

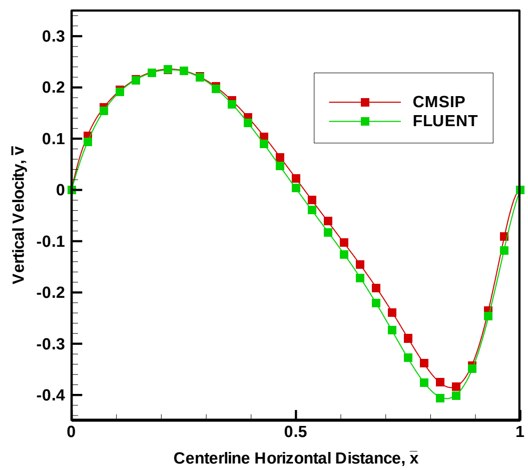

Figure 115 – Comparison of $\bar{v}$ velocity between CMSIP and FLUENT at $\bar{t} = 38$ and AR 1.1

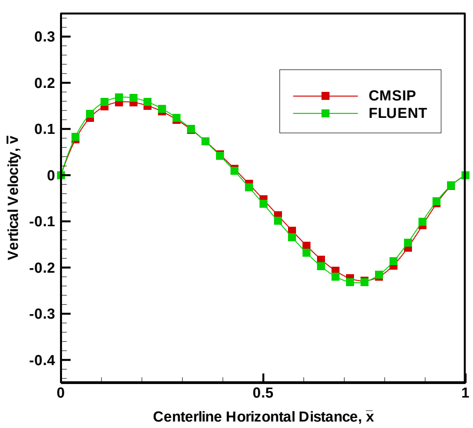

Figure 116 – comparison of $\bar{v}$ velocity between CMSIP and FLUENT at $\bar{t} = 46$ and AR 1.5

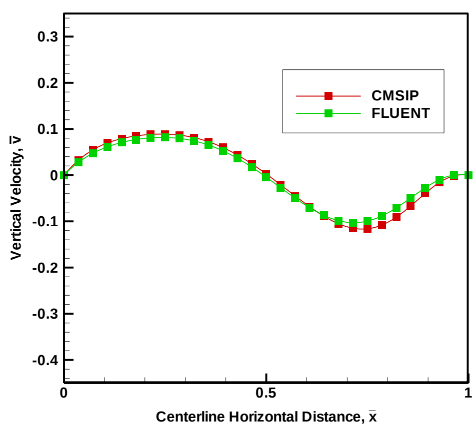

Figure 117 – comparison of $\bar{v}$ velocity between CMSIP and FLUENT at $\bar{t} = 70$ and AR 1.5

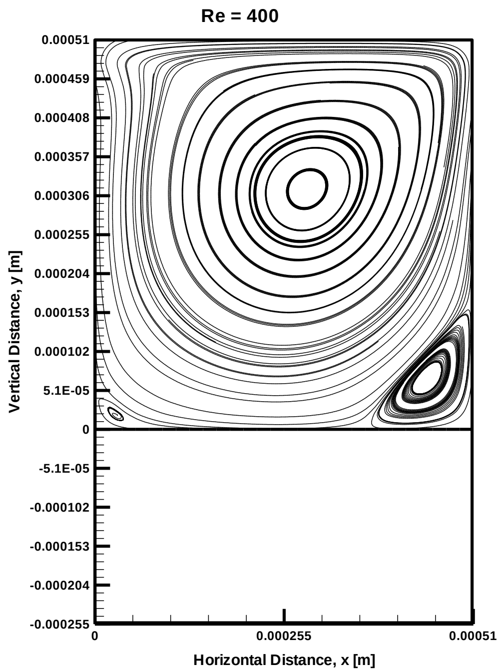

Figure 118 – Streamline plot for velocity magnitude at AR 1.0 (FLUENT)

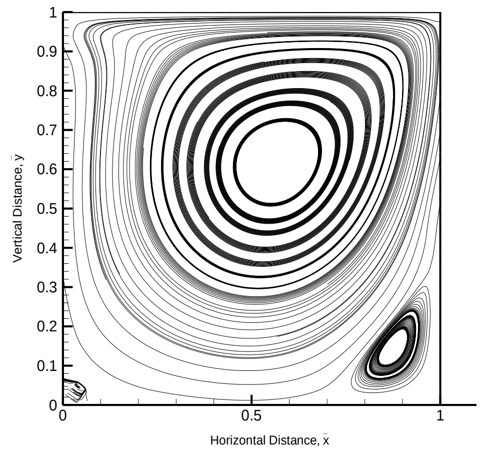

Figure 119 – Streamline plot for velocity magnitude at AR 1.0 (CMSIP)

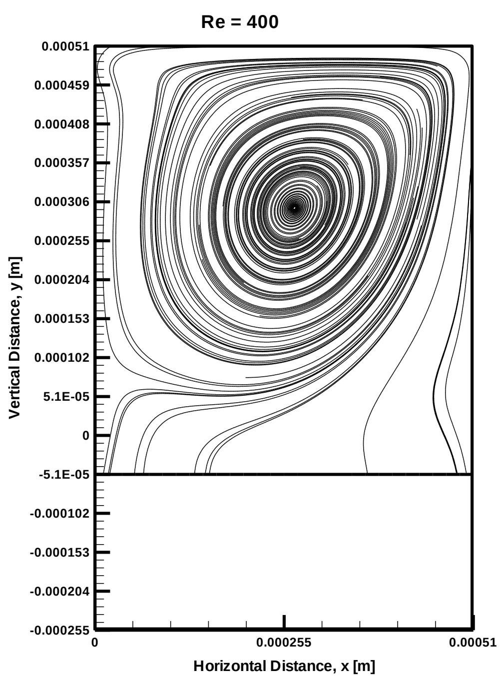

Figure 120 – Streamline plot for velocity magnitude at AR 1.1 (FLUENT)

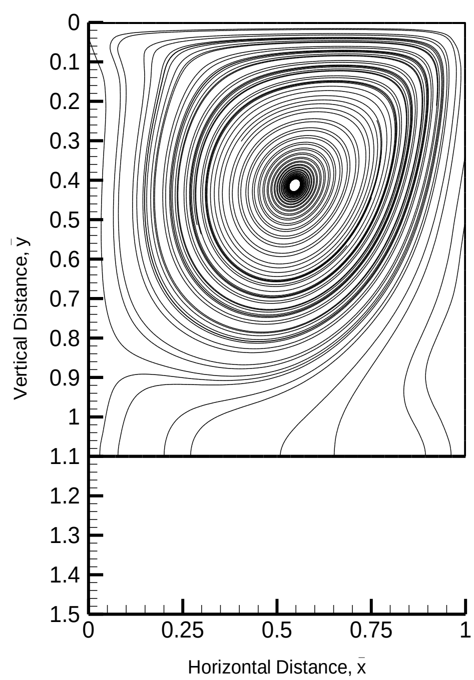

Figure 121 – Streamline plot for velocity magnitude at AR 1.1 (CMSIP)

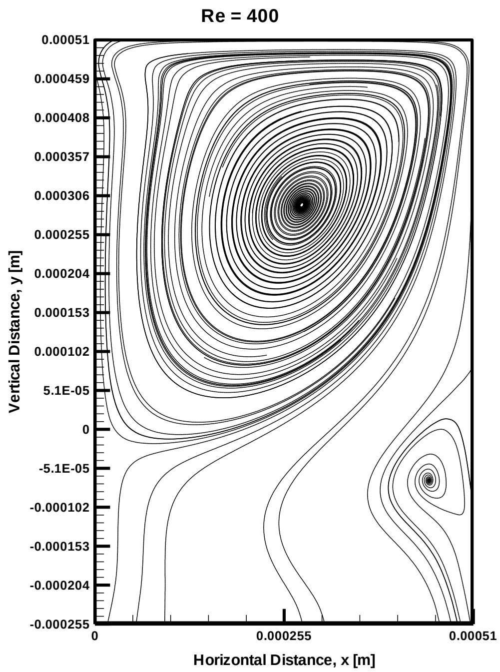

Figure 122 – Streamline plot for velocity magnitude at AR 1.5 (FLUENT)

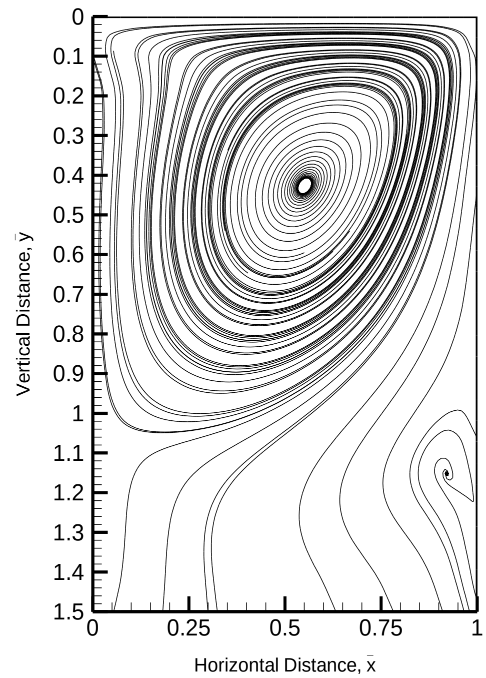

Figure 123 – Streamline plot for velocity magnitude at AR 1.5 (CMSIP)

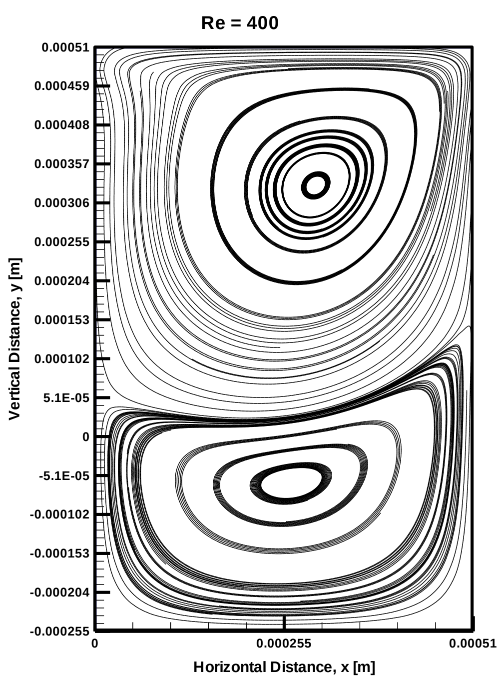

Figure 124 – Streamline plot for velocity magnitude at AR 1.5 Steady State (FLUENT)

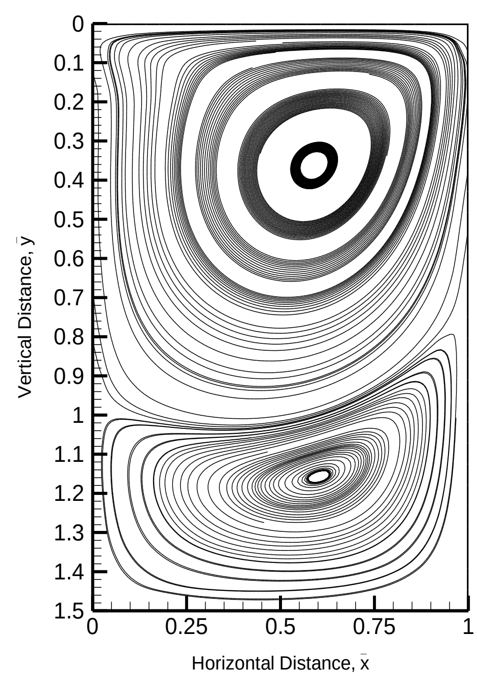

Figure 125 – Streamline plot for velocity magnitude at AR 1.5 Steady State (CMSIP)

9. Parametric Study for Unsteady Lid Driven Cavity Flow with a Moving Bottom Boundary

9.1 Effects of Different Bottom Boundary Velocities

In this study the bottom boundary of the cavity is moved with different velocities. In first case, the bottom is moved slowly with a constant velocity, $\bar{v}_b$ of -0.025 and later moved faster with a constant velocity $\bar{v}_b$ of $-$ 0.1. The figure 113 shows the bottom boundary velocity profile at different velocities.

It is observed that there is no significant changes in the location of the primary circulation (center) in all the three cases while the bottom boundary is moving except for the formation of secondary circulation (bottom). The formation of secondary circulation varies with speed. When the boundary is moving slowly, it gives enough time for the formation of secondary circulation (at *AR* 1.3) but when the bottom boundary is moved fast the secondary circulation forms only after the cavity reaches *AR* 1.5 and is illustrated in Figure 115 to 117.

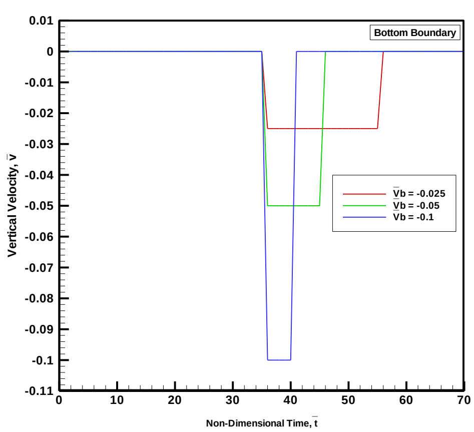

Figure 126 – Bottom velocity profiles

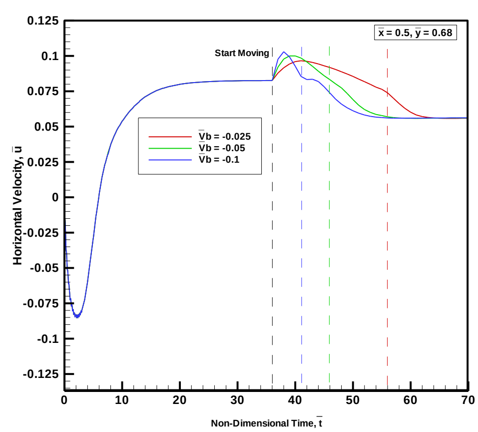

Figure 127 - $\bar{u}$ velocity histogram at node $\bar{x} = 0.5$, $\bar{y} = 0.68$

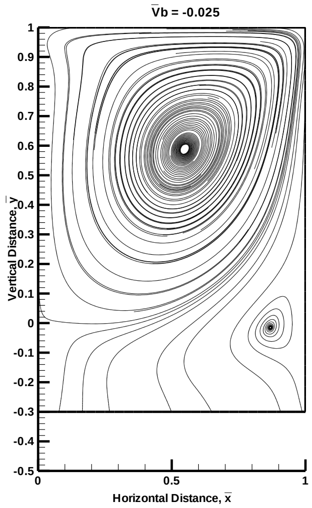

Figure 128 – Streamline plot of velocity magnitude at AR 1.3 with $\bar{v}_b = -0.025$

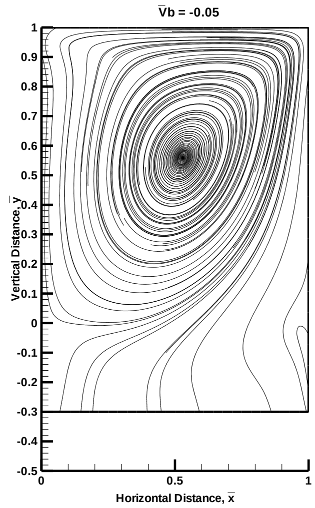

Figure 129 – Streamline plot of velocity magnitude at AR 1.3 with $\bar{v}_b = -0.05$

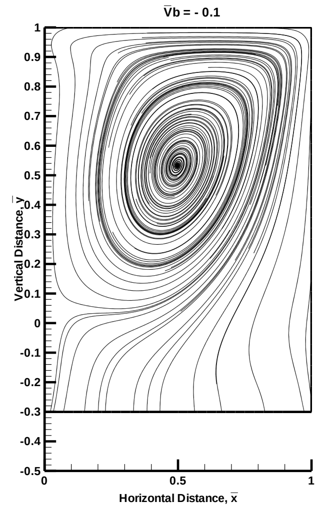

Figure 130 – Streamline plot of velocity magnitude at AR 1.3 with $\bar{v}_b = -0.1$

Table 15 – Comparison of the $\bar{u}$ velocities for different bottom boundary velocities at $\bar{t} = 42, AR\ 1.3$

43 grid pt .no.	$\bar{y}$	$\bar{t} = 42$, AR 1.3		
		$\bar{v}_b$ -0.025 $\bar{u}$	$\bar{v}_b$ -0.05 $\bar{u}$	$\bar{v}_b$ -0.1 $\bar{u}$
43	1.0000	1.00000	1.00000	1.00000
42	0.9644	0.63681	0.64121	0.65068
25	0.3571	-0.12226	-0.15616	-0.20838
24	0.3214	-0.14764	-0.18461	-0.23501
23	0.2857	-0.17217	-0.20975	-0.25304
22	0.2499	-0.19450	-0.22923	-0.26033
21	0.2142	-0.21292	-0.24057	-0.25666
20	0.1785	-0.22518	-0.24279	-0.24263
19	0.1428	-0.22991	-0.23621	-0.21970
18	0.1070	-0.22717	-0.22107	-0.19055
17	0.0713	-0.21681	-0.19858	-0.15821
9	-0.2144	-0.01575	0.00371	0.01639
8	-0.2501	-0.00285	0.00837	0.01476
7	-0.2858	0.00000	0.00000	0.00000
6	-0.3215			
5	-0.3573			
4	-0.3930			
3	-0.4287			
2	-0.4644			
1	-0.5002			

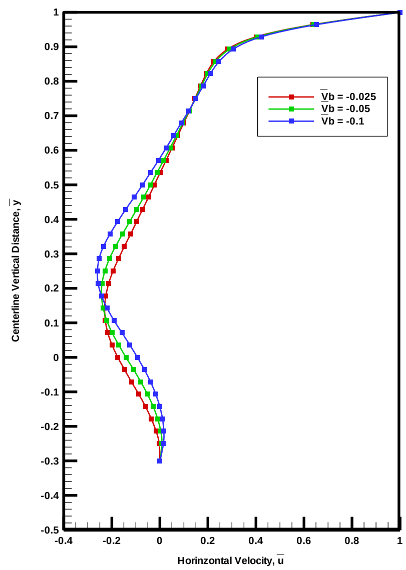

Figure 131 - Comparison of the $\bar{u}$ velocities for different bottom boundary velocities at $\bar{t} = 42, AR\ 1.3$

Table 16 – Comparison of the $\bar{v}$ velocities for different bottom boundary velocities at $\bar{t} = 42, AR\ 1.3$

29 grid pt .no.	$\bar{x}$	$\bar{t}$ = 42, AR 1.3		
		$\bar{v}_b$ -0.025	$\bar{v}_b$ -0.05	$\bar{v}_b$ -0.1
		$\bar{v}$	$\bar{v}$	$\bar{v}$
29	1.0000	0.00000	0.00000	0.00000
28	0.9644	-0.09494	-0.06109	-0.04064
27	0.9287	-0.18898	-0.13831	-0.10193
26	0.8930	-0.28087	-0.21808	-0.17037
25	0.8572	-0.34946	-0.28299	-0.23059
24	0.8215	-0.38456	-0.32171	-0.27121
23	0.7858	-0.38738	-0.33185	-0.28752
22	0.7501	-0.36519	-0.31768	-0.28108
21	0.7143	-0.32712	-0.28645	-0.25721
9	0.2857	0.16054	0.18316	0.18467
8	0.2499	0.18077	0.20403	0.20020
7	0.2142	0.19243	0.21783	0.20919
6	0.1785	0.19523	0.22373	0.21136
5	0.1428	0.18908	0.22037	0.20592
4	0.1070	0.17252	0.20446	0.19009
3	0.0713	0.14048	0.16933	0.15767
2	0.0356	0.08187	0.10446	0.09826
1	0.0000	0.00000	0.00000	0.00000

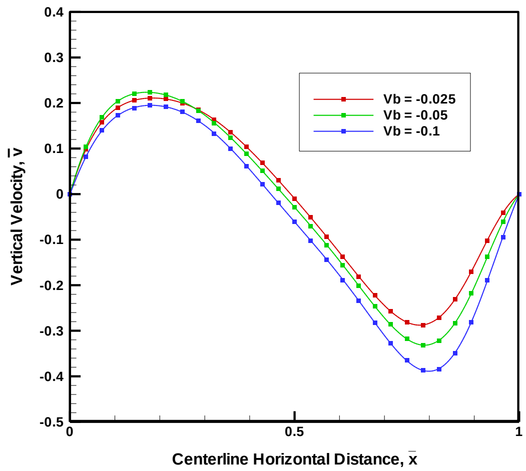

Figure 132 - Comparison of the $\bar{v}$ velocities for different bottom boundary velocities at $\bar{t} = 42, AR\ 1.3$

9.2 Effects of Different Reynolds Number

The location of primary circulation varies with Re number. For low Re the primary circulation form at the upper part of the cavity and as Re number increases it moves towards the center of cavity at *AR* 1.0. The instant the cavity reaches *AR* 1.5 the secondary circulation is increases in size in case of *Re* 1000. A small size of secondary circulation can be seen at *AR* 1.5 and no secondary circulation in case of *Re* 100.

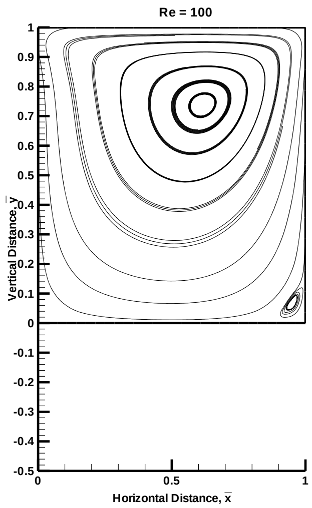

Figure 133 – Streamline plot of velocity magnitude at *AR* 1.0 for *Re* 100

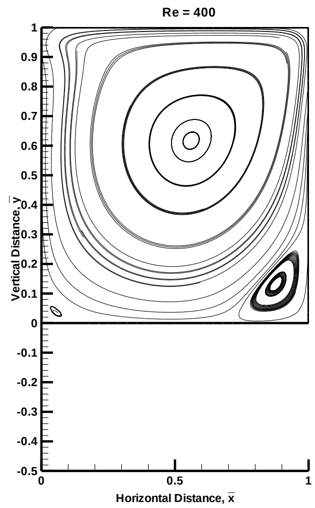

Figure 134 – Streamline plot of velocity magnitude at *AR* 1.0 for *Re* 400

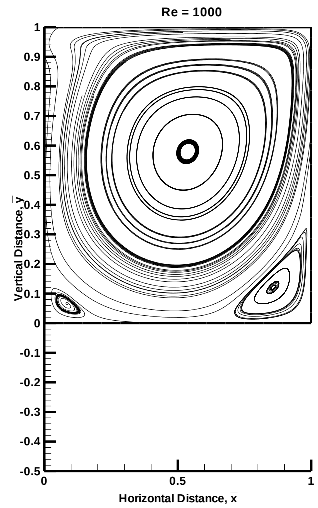

Figure 135 – Streamline plot of velocity magnitude at *AR* 1.0 for *Re* 1000

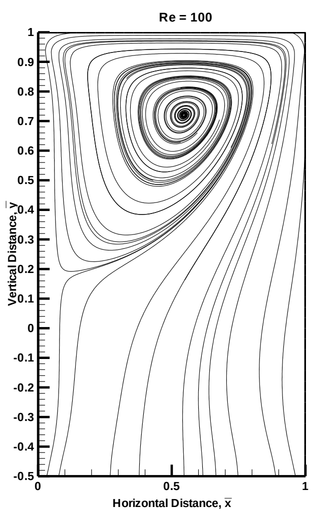

Figure 136 – Streamline plot of velocity magnitude at *AR* 1.5 for *Re* 100

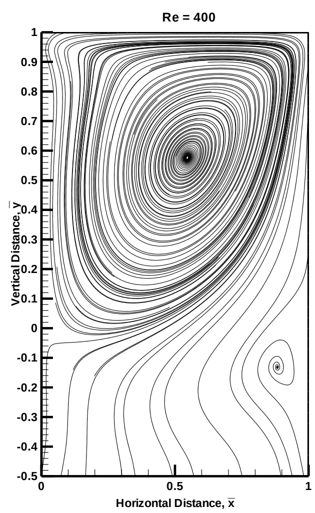

Figure 137 – Streamline plot of velocity magnitude at *AR* 1.5 for *Re* 400

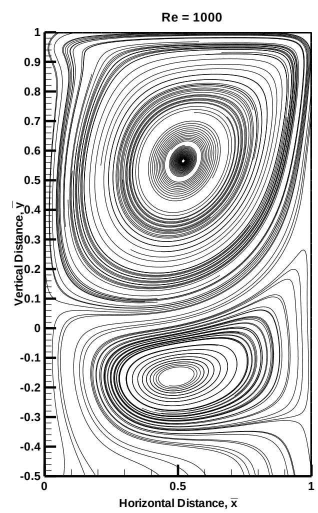

Figure 138 – Streamline plot of velocity magnitude at *AR* 1.5 for *Re* 1000

Table 17 – Comparison of the results (maximum velocities) of the unsteady lid driven cavity flow with different Re = 100, 400 and 1000 at different aspect ratios

43 grid pt .no.	$\bar{y}$	$\bar{t} = 36$, AR 1.0			$\bar{t} = 46$, AR 1.5		
		Re = 100	Re = 400	Re = 1000	Re = 100	Re = 400	Re = 1000
43	1.0000	1.00000	1.00000	1.00000	1.00000	1.00000	1.00000
42	0.9644	0.75841	0.63894	0.53489	0.77928	0.65561	0.55035
29	0.5000	-0.20415	-0.13124	-0.07263	-0.15839	-0.04741	-0.04180
28	0.4643	-0.20814	-0.17510	-0.10623	-0.16671	-0.07609	-0.06680
27	0.4286	-0.20555	-0.21820	-0.13945	-0.17099	-0.10547	-0.09322
26	0.3928	-0.19758	-0.25726	-0.17306	-0.17171	-0.13489	-0.12235
25	0.3571	-0.18549	-0.28699	-0.20884	-0.16933	-0.16319	-0.15548
24	0.3214	-0.17061	-0.30165	-0.24762	-0.16438	-0.18877	-0.19295
23	0.2857	-0.15402	-0.29928	-0.28694	-0.15734	-0.20978	-0.23277
22	0.2499	-0.13661	-0.28046	-0.31715	-0.14871	-0.22432	-0.26988
21	0.2142	-0.11888	-0.24708	-0.32642	-0.13892	-0.23121	-0.29597
20	0.1785	-0.10107	-0.20472	-0.31040	-0.12837	-0.23045	-0.30409
19	0.1428	-0.08313	-0.15971	-0.26863	-0.11739	-0.22241	-0.29359
18	0.1070	-0.06472	-0.11641	-0.20680	-0.10623	-0.20786	-0.26587
17	0.0713	-0.04529	-0.07636	-0.13828	-0.09512	-0.18825	-0.22539
16	0.0356	-0.02405	-0.03850	-0.07077	-0.08422	-0.16535	-0.18066
15	-0.0001	0.00000	0.00000	0.00000	-0.07364	-0.14080	-0.13828
14	-0.0358				-0.06350	-0.11590	-0.10109
13	-0.0715				-0.05386	-0.09156	-0.06892
12	-0.1073				-0.04477	-0.06841	-0.04033
11	-0.1430				-0.03628	-0.04684	-0.01406
10	-0.1787				-0.02845	-0.02714	0.01037
9	-0.2144				-0.02132	-0.00958	0.03272
8	-0.2501				-0.01494	0.00555	0.05229
7	-0.2858				-0.00941	0.01787	0.06795
6	-0.3215				-0.00478	0.02693	0.07827
5	-0.3573				-0.00120	0.03212	0.08150
4	-0.3930				0.00123	0.03280	0.07602
3	-0.4287				0.00234	0.02828	0.06056
2	-0.4644				0.00198	0.01764	0.03481
1	-0.5002				0.00000	0.00000	0.00000

Table 18 – Comparison of the results (maximum velocities) of the unsteady lid driven cavity flow with different *Re* = 100, 400 and 1000 at different aspect ratios

29 grid pt .no.	$\bar{x}$	$\bar{t} = 36$, AR 1.0			$\bar{t} = 46$, AR 1.5		
		Re = 100	*Re* = 400	*Re* = 1000	*Re* = 100	*Re* = 400	*Re* = 1000
29	1.0000	0.00000	0.00000	0.00000	0.00000	0.00000	0.00000
28	0.9644	-0.06915	-0.12048	-0.21083	-0.04846	-0.02200	0.00208
27	0.9287	-0.13552	-0.25975	-0.37766	-0.09286	-0.05708	-0.02188
26	0.8930	-0.19013	-0.35928	-0.41747	-0.13479	-0.10083	-0.06555
25	0.8572	-0.22677	-0.39669	-0.38562	-0.17182	-0.14631	-0.11813
24	0.8215	-0.24275	-0.38253	-0.32863	-0.20227	-0.18657	-0.16637
23	0.7858	-0.23886	-0.33706	-0.27409	-0.22492	-0.21601	-0.20000
22	0.7501	-0.21837	-0.27900	-0.22984	-0.23913	-0.23139	-0.21470
21	0.7143	-0.18579	-0.22118	-0.19146	-0.24480	-0.23214	-0.21164
9	0.2857	0.16836	0.26307	0.25005	-0.01353	0.12399	0.12035
8	0.2499	0.17206	0.27175	0.28377	0.00081	0.14345	0.14135
7	0.2142	0.17111	0.27035	0.30660	0.01203	0.15795	0.15773
6	0.1785	0.16479	0.25981	0.31368	0.01996	0.16661	0.16843
5	0.1428	0.15191	0.24123	0.30299	0.02435	0.16787	0.17276
4	0.1070	0.13092	0.21382	0.27547	0.02486	0.15852	0.16991
3	0.0713	0.09988	0.17232	0.23065	0.02097	0.13288	0.15573
2	0.0356	0.05677	0.10561	0.15187	0.01161	0.08264	0.11242
1	0.0000	0.00000	0.00000	0.00000	0.00000	0.00000	0.00000

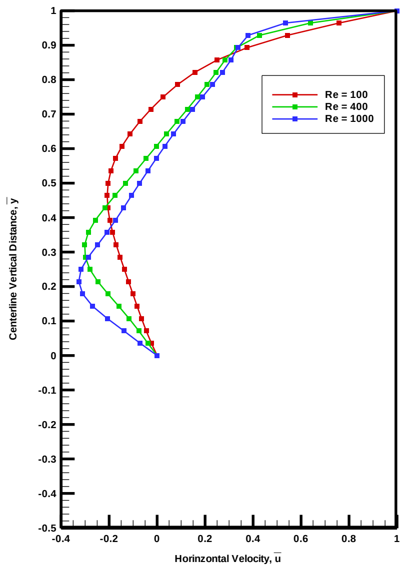

Figure 139 - Comparison of the $\bar{u}$ velocities for different Re number $\bar{t} = 36, AR\ 1.0$

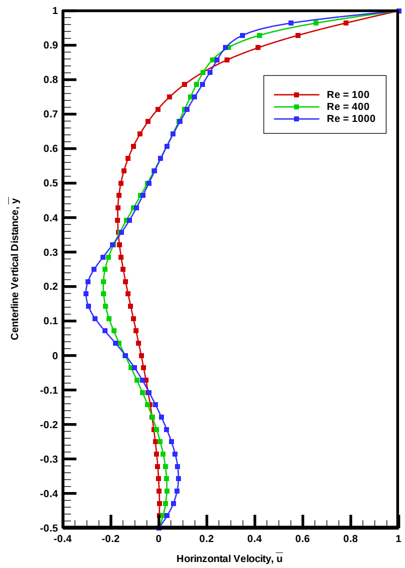

Figure 140 - Comparison of the $\bar{u}$ velocities for different Re number $\bar{t} = 46, AR\ 1.5$

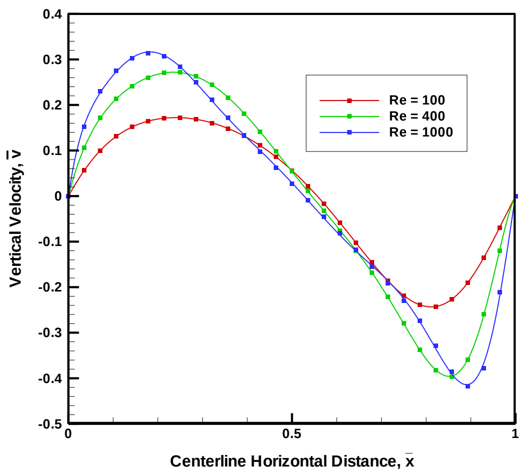

Figure 141 - Comparison of the $\bar{v}$ velocities for different Re number $\bar{t} = 36, AR\ 1.0$

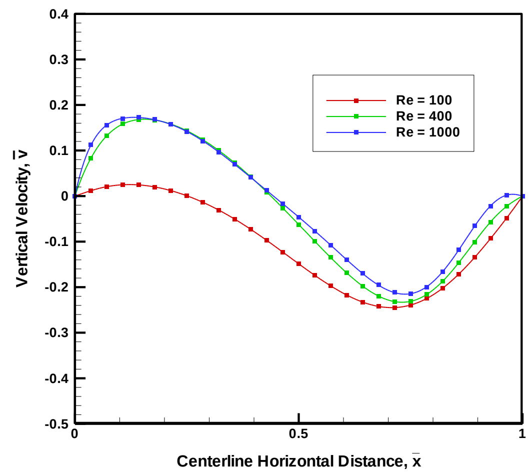

Figure 142 - Comparison of the $\bar{v}$ velocities for different Re number $\bar{t} = 46, AR\ 1.5$

9.3 Effect of Different Mach-Number

There is no effect either in circulation patterns or velocity profiles for M = 0.01, 0.03 and 0.05 as the range of *M* number is too small. The $\bar{u}$ velocity profiles are illustrated in figure 130 and 131 at *AR* 1.0 and *AR* 1.5 and quantified in table 19.

Table 19– Comparison of the $\bar{u}$ velocities for Ma = 0.01, 0.03 and 0.05 at different aspect ratios

43 grid pt .no.	$\bar{y}$	$\bar{t} = 36$, AR 1.0			$\bar{t} = 46$, AR 1.5		
		Ma = 0.01	Ma = 0.03	Ma = 0.05	Ma = 0.01	Ma = 0.03	Ma = 0.05
43	1.0000	1.00000	1.00000	1.00000	1.00000	1.00000	1.00000
42	0.9644	0.63915	0.63894	0.63913	0.65593	0.65593	0.65593
25	0.3571	-0.28663	-0.28699	-0.28666	-0.16267	-0.16267	-0.16267
24	0.3214	-0.30149	-0.30165	-0.30150	-0.18828	-0.18828	-0.18828
23	0.2857	-0.29937	-0.29928	-0.29935	-0.20935	-0.20935	-0.20935
22	0.2499	-0.28081	-0.28046	-0.28076	-0.22400	-0.22400	-0.22400
21	0.2142	-0.24765	-0.24708	-0.24759	-0.23103	-0.23103	-0.23103
20	0.1785	-0.20542	-0.20472	-0.20535	-0.23042	-0.23042	-0.23042
19	0.1428	-0.16046	-0.15971	-0.16038	-0.22252	-0.22252	-0.22252
18	0.1070	-0.11711	-0.11641	-0.11704	-0.20811	-0.20811	-0.20811
17	0.0713	-0.07692	-0.07636	-0.07686	-0.18860	-0.18860	-0.18860
16	0.0356	-0.03883	-0.03850	-0.03880	-0.16578	-0.16578	-0.16578
15	-0.0001	0.00000	0.00000	0.00000	-0.14127	-0.14127	-0.14127
14	-0.0358				-0.11637	-0.11637	-0.11637
13	-0.0715				-0.09201	-0.09201	-0.09201
12	-0.1073				-0.06883	-0.06883	-0.06883
11	-0.1430				-0.04722	-0.04722	-0.04722
10	-0.1787				-0.02749	-0.02749	-0.02749
9	-0.2144				-0.00989	-0.00989	-0.00989
8	-0.2501				0.00528	0.00528	0.00528
7	-0.2858				0.01764	0.01764	0.01764
6	-0.3215				0.02672	0.02672	0.02672
5	-0.3573				0.03194	0.03194	0.03194
4	-0.3930				0.03262	0.03262	0.03262
3	-0.4287				0.02810	0.02810	0.02810
2	-0.4644				0.01746	0.01746	0.01746
1	-0.5002				0.00000	0.00000	0.00000

Table 20 – Comparison of the $\bar{v}$ velocities for Ma = 0.01, 0.03 and 0.05 at different aspect ratios

29 grid pt .no.	$\bar{x}$	$\bar{t}$ = 36, AR 1.0					
		Ma = 0.01	Ma = 0.03	Ma = 0.05	Ma = 0.01	Ma = 0.01	Ma = 0.01
29	1.0000	0.00000	0.00000	0.00000	0.00000	0.00000	0.00000
28	0.9644	-0.12062	-0.12048	-0.12059	-0.02128	-0.02128	-0.02128
27	0.9287	-0.25988	-0.25975	-0.25986	-0.05668	-0.05668	-0.05668
26	0.8930	-0.35954	-0.35928	-0.35951	-0.10061	-0.10061	-0.10061
25	0.8572	-0.39683	-0.39669	-0.39681	-0.14625	-0.14625	-0.14625
24	0.8215	-0.38258	-0.38253	-0.38258	-0.18660	-0.18660	-0.18660
23	0.7858	-0.33705	-0.33706	-0.33705	-0.21602	-0.21602	-0.21602
22	0.7501	-0.27898	-0.27900	-0.27898	-0.23131	-0.23131	-0.23131
21	0.7143	-0.22117	-0.22118	-0.22117	-0.23191	-0.23191	-0.23191
8	0.2499	0.27196	0.27175	0.27193	0.14475	0.14475	0.14475
7	0.2142	0.27063	0.27035	0.27059	0.15927	0.15927	0.15927
6	0.1785	0.26012	0.25981	0.26009	0.16796	0.16796	0.16796
5	0.1428	0.24156	0.24123	0.24153	0.16921	0.16921	0.16921
4	0.1070	0.21413	0.21382	0.21410	0.15981	0.15981	0.15981
3	0.0713	0.17257	0.17232	0.17254	0.13410	0.13410	0.13410
2	0.0356	0.10571	0.10561	0.10570	0.08380	0.08380	0.08380
1	0.0000	0.00000	0.00000	0.00000	0.00000	0.00000	0.00000

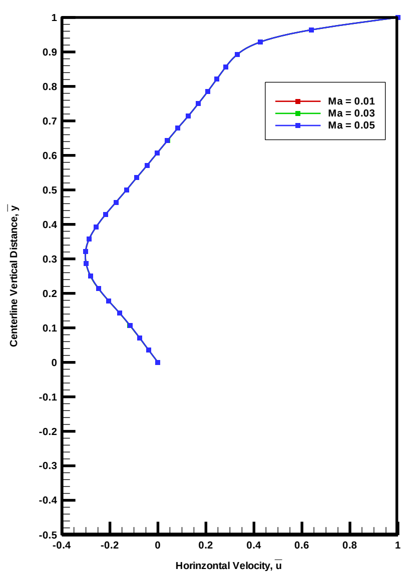

Figure 143 - Comparison of the $\bar{v}$ velocities for different M number $\bar{t} = 36, AR\ 1.0$

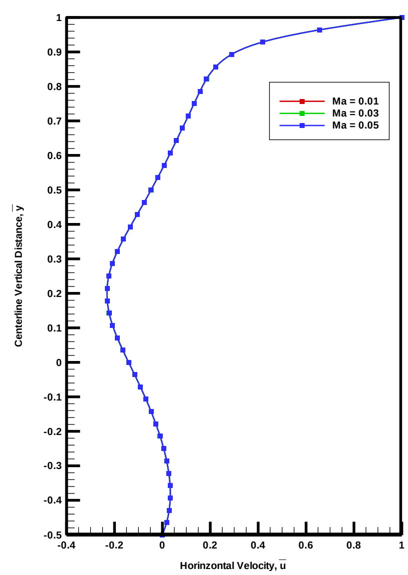

Figure 144 - Comparison of the $\bar{v}$ velocities for different M number $\bar{t} = 46, AR\ 1.5$

9.4 Effects of Different Temperature and Pressure.

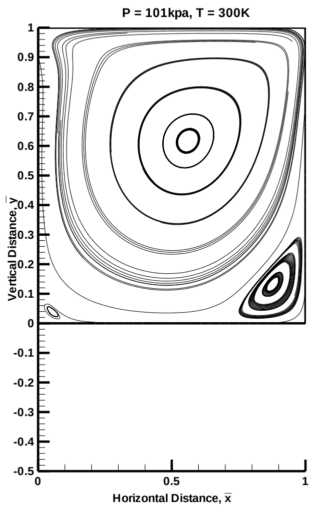

Figure 145 – Streamline plot of velocity magnitude at *AR* 1.0 for P = 100kpa,T = 300K

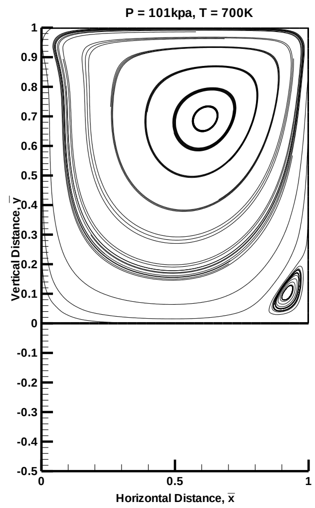

Figure 146 – Streamline plot of velocity magnitude at *AR* 1.0 for for P = 100kpa, T = 700K

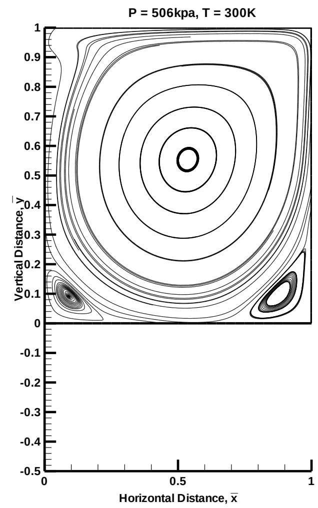

Figure 147 – Streamline plot of velocity magnitude at *AR* 1.0 for for P = 506kpa, T = 300K

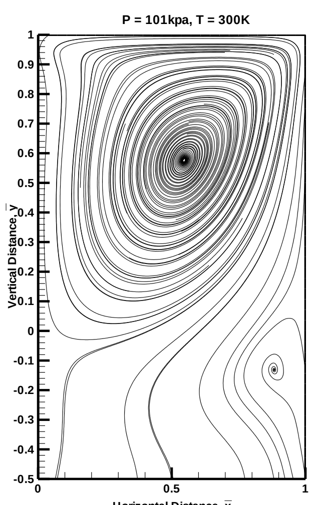

Figure 148 – Streamline plot of velocity magnitude at *AR* 1.5 for for P = 100kpa,T = 300K

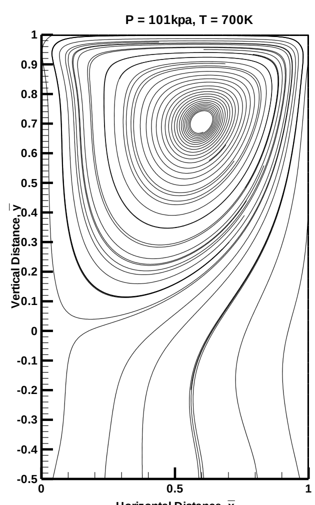

Figure 149 – Streamline plot of velocity magnitude at *AR* 1.5 for for P = 100kpa,T = 700K

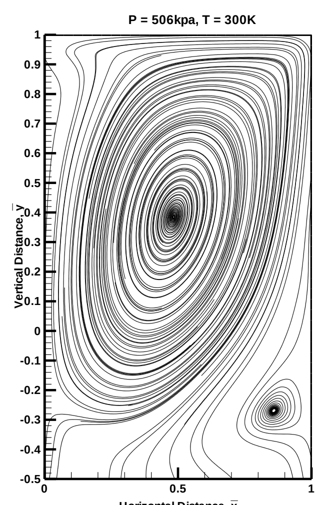

Figure 150 – Streamline plot of velocity magnitude at *AR* 1.5 for for P = 506kpa,T = 300K

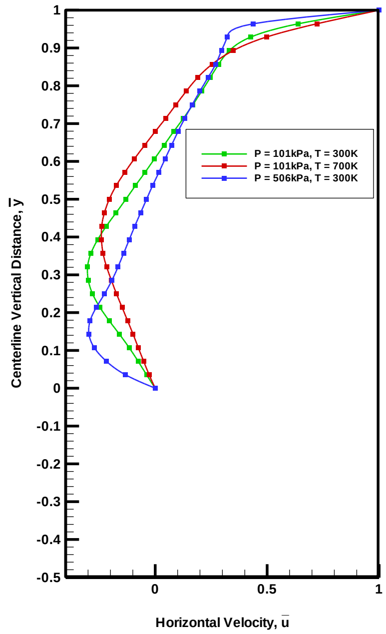

Figure 151 - Comparison of the $\bar{u}$ velocities for different P,T at $\bar{t} = 35$ and AR 1.0

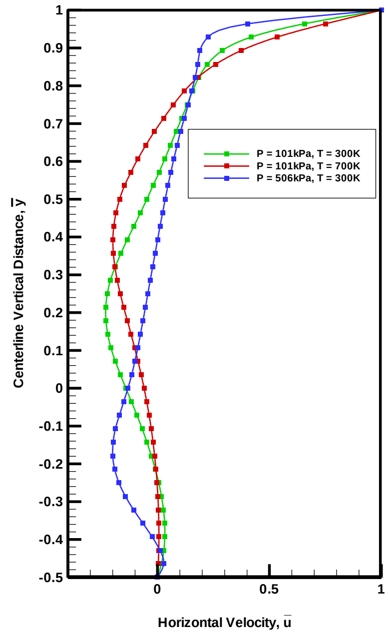

Figure 152 - Comparison of the $\bar{u}$ velocities for different P,T $\bar{t} = 46$ and AR 1.5

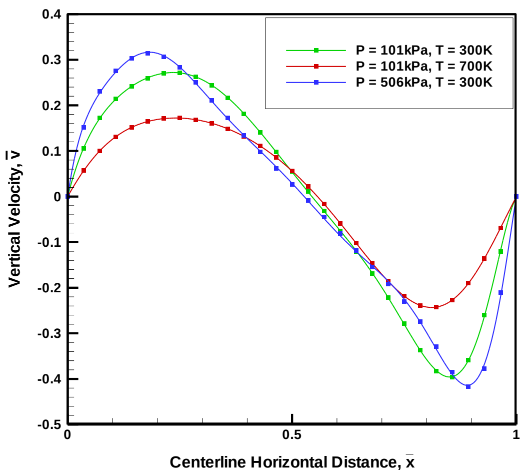

Figure 153 - Comparison of the $\bar{v}$ velocities for different P,T at $\bar{t} = 35$ and AR 1.0

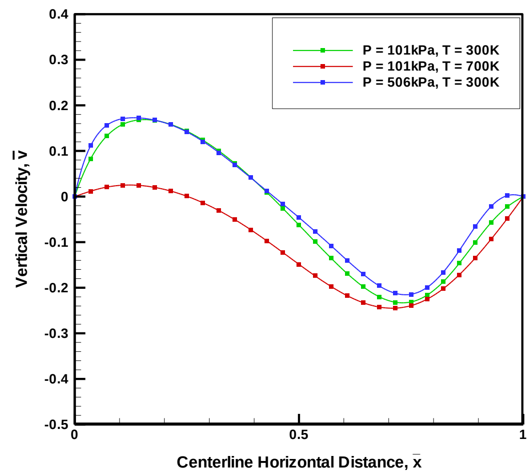

Figure 154 - Comparison of the $\bar{v}$ velocities for different P,T at $\bar{t} = 46$ and AR 1.5

Table 21 – Comparison of $\bar{u}$ velocities for different P and T at different aspect ratios

43 grid pt .no.	$\bar{y}$	$\bar{t} = 36$, AR 1.0			$\bar{t} = 46$, AR 1.5		
		P = 101kPa, T = 300K	P = 101kPa, T = 300K	P = 101kPa, T = 300K	P = 101kPa, T = 300K	P = 101kPa, T = 700K	P = 506kPa, T = 300K
43	1.0000	1.00000	1.00000	1.00000	1.00000	1.00000	1.00000
42	0.9644	0.63894	0.72156	0.43785	0.65561	0.75085	0.40275
28	0.4643	-0.17510	-0.22732	-0.06524	-0.07609	-0.18542	0.02293
27	0.4286	-0.21820	-0.23898	-0.09119	-0.10547	-0.19531	0.01159
26	0.3928	-0.25726	-0.24037	-0.11647	-0.13489	-0.19902	0.00046
25	0.3571	-0.28699	-0.23251	-0.14103	-0.16319	-0.19706	-0.01048
24	0.3214	-0.30165	-0.21715	-0.16592	-0.18877	-0.19024	-0.02136
23	0.2857	-0.29928	-0.19650	-0.19343	-0.20978	-0.17954	-0.03219
22	0.2499	-0.28046	-0.17280	-0.22631	-0.22432	-0.16601	-0.04306
21	0.2142	-0.24708	-0.14792	-0.26276	-0.23121	-0.15069	-0.05395
20	0.1785	-0.20472	-0.12310	-0.29079	-0.23045	-0.13448	-0.06493
19	0.1428	-0.15971	-0.09890	-0.29610	-0.22241	-0.11811	-0.07610
18	0.1070	-0.11641	-0.07527	-0.27209	-0.20786	-0.10212	-0.08778
17	0.0713	-0.07636	-0.05163	-0.21768	-0.18825	-0.08691	-0.10051
16	0.0356	-0.03850	-0.02699	-0.13258	-0.16535	-0.07271	-0.11501
15	-0.0001	0.00000	0.00000	0.00000	-0.14080	-0.05968	-0.13174
14	-0.0358				-0.11590	-0.04787	-0.15053
13	-0.0715				-0.09156	-0.03729	-0.17025
12	-0.1073				-0.06841	-0.02792	-0.18765
11	-0.1430				-0.04684	-0.01974	-0.19829
10	-0.1787				-0.02714	-0.01271	-0.19979
9	-0.2144				-0.00958	-0.00679	-0.19144
1	-0.5002				0.00000	0.00000	0.00000

Table 22 – Comparison of $\bar{v}$ velocities for different P and T at different aspect ratios

43 grid pt .no.	$\bar{x}$	$\bar{t} = 36$, AR 1.0			$\bar{t} = 46$, AR 1.5		
		P = 101kPa, T = 300K	P = 101kPa, T = 700K	P = 506kPa, T = 300K	P = 101kPa, T = 300K	P = 101kPa, T = 700K	P = 506kPa, T = 300K
29	1.0000	0.00000	0.00000	0.00000	0.00000	0.00000	0.00000
28	0.9644	-0.12048	-0.08173	-0.32965	-0.02200	-0.01898	-0.10630
27	0.9287	-0.25975	-0.16861	-0.38096	-0.05708	-0.04197	-0.24171
26	0.8930	-0.35928	-0.24255	-0.33860	-0.10083	-0.06646	-0.32310
25	0.8572	-0.39669	-0.29044	-0.28272	-0.14631	-0.09000	-0.33743
24	0.8215	-0.38253	-0.30760	-0.24064	-0.18657	-0.11034	-0.31215
23	0.7858	-0.33706	-0.29644	-0.20866	-0.21601	-0.12567	-0.26972
22	0.7501	-0.27900	-0.26398	-0.17858	-0.23139	-0.13476	-0.22729
21	0.7143	-0.22118	-0.21812	-0.14834	-0.23214	-0.13713	-0.19244
9	0.2857	0.26307	0.19970	0.19690	0.12399	0.06195	0.12628
8	0.2499	0.27175	0.20140	0.23058	0.14345	0.07154	0.15743
7	0.2142	0.27035	0.19837	0.26217	0.15795	0.07758	0.18930
6	0.1785	0.25981	0.19026	0.28359	0.16661	0.07954	0.21870
5	0.1428	0.24123	0.17592	0.28729	0.16787	0.07670	0.24048
4	0.1070	0.21382	0.15322	0.26978	0.15852	0.06820	0.24770
1	0.0000	0.00000	0.00000	0.00000	0.00000	0.00000	0.00000

10. Conclusions

A benchmark case, driven cavity flow with a moving bottom, is proposed to study the accuracy of numerical solution methods to solve unsteady compressible Navier-Stokes equations for flows with moving boundaries. A numerical simulation has been done using ANSYS FLUENT and compared the results with CMSIP. The accuracy of the numerical simulations were verified using the accepted benchmark case for incompressible flow problems, that is, the classical problem of driven cavity flow.

The numerical simulations were carried out for the proposed unsteady, moving boundary cavity where the aspect ratio of the cavity is changed from 1 to 1.5 at a constant speed. Following conclusions were drawn from the results of these simulations:

1. The results obtained using FLUENT and CMSIP solution algorithms for unsteady lid driven cavity flow with moving boundary indicate that the proposed mathematical model and the solution procedure are in good agreement.

3. Three different mesh motion techniques has been used and each technique has their own advantages and disadvantages. For the present study, it is concluded that layering technique is suitable to the current moving boundary problem.

4. It is also concluded that there is no addition or reduction of mass in the cavity and thus mass is conserved when layering technique is used (see Appendix IV.)

5. There is a considerable change in pressure, temperature and density when the bottom boundary is moving which can be seen in histogram and contour plots (see section 9.1). Thus the current problem is compressible. The primary circulation moves a little upwards then its previous location at *AR* 1.0 when it attains steady state after reaching AR 1.5. The secondary

circulation disappears when the bottom boundary starts moving and appears again in larger size at the bottom of the cavity when it reaches *AR* 1.5.

6. It is observed that when the bottom boundary is moved slow the secondary circulation forms at when the cavity reaches *AR* 1.3. When it is moving fast there is no formation of secondary circulation until the cavity reaches *AR* 1.5.

7. There is very little change in circulation formation and velocity profiles for M = 0.01, 0.03 and 0.05.

8. At Re = 100 there is no formation of secondary circulation at the bottom of the cavity and has only primary circulation towards the upward direction of the cavity at the instant AR 1.5 is achieved. There is a formation of small secondary circulation at Re = 400 and large secondary circulation at Re = 1000 at *AR* 1.5. So higher the lid velocity, faster is the formation of secondary circulation.

9. The increase in temperature and pressure effects the location and size of primary and secondary circulation.

11. Recommendations

Following studies are recommended to improve the understanding of characteristics of unsteady circulation patterns inside lid driven cavities with moving boundaries:

1. Higher lid velocities should be tried to see more effect in temperature and pressure inside the cavity and capture the acoustic oscillations.

2. A more wide range of Mach number should be tried to see its effects in the circulation pattern and compressibility of the fluid.

3. Motion of higher different aspect ratios should be studied.

REFERENCES

[1] Ghia, U., Ghia, K.N., and Shin, C.T., 1982, "High-Re Solutions for Incompressible Flow Using the Navier-Stokes Equations and a Multigrid Method," Journal of Computational Physics, **48**, pp. 387-411.

[2] Goodrich, J. W., and Soh, W.Y., 1989, "Time-Dependent Viscous Incompressible Navier-Stokes Equations: The Finite Difference Galerkin Formulation and Streamfunction Algorithms," Journal of Computational Physics, **84**, pp. 207-241.

[3] Burggraf, O.F., 1966, "Analytical and Numerical Studies of the Structures of Steady Separated Flows," Journal of Fluid Mechanics, **24**, pp. 113-151.

[4] Bozeman, J.D. and Dalton, C., 1973, "Numerical Study of Viscous Flows in a Cavity," Journal of Computational Physics, **12**, pp. 348-363.

[5] Rubin, S. G. and Harris, J.E., 1975, "Numerical Studies of Incompressible Viscous Flow in a Driven Cavity," NASA SP-378.

[6] Iwatsu, R., Hyun, J. M., and Kuwahara, K.,1993, "Numerical Simulations of Three-Dimensional Flows in a Cubic Cavity with an Oscillating Lid," Journal of Fluids Engineering, **115**, pp. 680-686.

[7] Freitas C. J., et al,, 1985, "Numerical Simulation of Three Dimensional Flow in a Cavity," Int. J. Numerical Methods Fluids, **5**, pp. 561-575.

[8] Agarwal, R. K., 1981, "A Third Order Accurate Upwind Scheme for Navier-Stokes Solutions at High Reynolds Numbers," AIAA Paper No. 81-0112.

[9] Chen, K.H., and Pletcher, R. H., 1991, "Primitive Variable, Strongly Implicit Calculation Procedure for Viscous Flows at All Speeds," AIAA Journal, **29**, No. 8, pp. 1241-1249.

[10] Mills, R.D., 1965, "Numerical Solutions of the Viscous Flow Equations for a Class of Closed Flows," J. R. Aeronaut. Soc., **69**, pp. 714-718.

[11] Pan, F., and Acrivos, A., 1967, "Steady Flows in Rectangular Cavities," J. Fluid Mech., **28**, pp. 643-655.

[12] Koseff, J. R. and Street, R. L., 1984, "Visualization Studies of a Shear Driven Three-Dimensional Recirculation Flow," J. Fluid Eng., **106**, pp. 21-29.

[13] Manalo, L. and, Akyuzlu, K. M., 2003, " A Study of Unsteady Natural Convection in Cryogenic Storage Tanks for Densified Propellants," *Proceedings of the IMECE2003,* Paper No.41810.

[14] Akyuzlu, K. M., and Antoniou, A., 2002, " Determination of Regression Rate in an Ablating Hybrid Rocket Solid Fuel Using a Physics Based Comprehensive Mathematical Model," *Proceeding of the AIAA 38th Joint Propulsion Conference*, Paper No. 2002-3577.

[15] Akyuzlu, K.M., Antoniou, A., Pavri, Y., 2004, "A Case Study for Compressible Flow Benchmarking-Simulation of Unsteady Driven Cavity Flow with Moving Boundaries Using CMSIP" *Proceedings of ASME HTFED Conference,* Paper No 2004-56642.

[16] ANSYS FLUENT User's Guide. ANSYS Inc., Canonsburg, PA, release 13.0 edition, 2010.

[17] ANSYS FLUENT Theory Guide. ANSYS Inc., Canonsburg, PA, release 14.0 edition, 2011.

[18] FLUENT 6.3 User's Guide. FLUENT Inc., Lebanon, NH, 2006.

Appendix I

Vector Form of Governing Differential Equations

Continuity equation:

$$\frac{D\rho}{Dt} + \rho(\nabla.\vec{u}) = 0 \tag{I.1}$$

Momentum equation:

$$\rho\frac{D\vec{u}}{Dt} = \rho\vec{g} - \nabla P + \nabla.\tau'_{ij} \tag{I.2}$$

where, shear stress term can be given by

$$\tau'_{ij} = \mu\left(\frac{\partial u_i}{\partial x_j} + \frac{\partial u_j}{\partial x_i}\right) - \frac{2}{3}\mu(\frac{\partial u_k}{\partial x_k})\delta_{ij}$$

The Kronecker Delta is defined as,

$$\delta_{ij} = \begin{cases} 1 & if\ i = j \\ 0 & if\ i \neq j \end{cases}$$

Energy equation:

$$\rho C_p\frac{DT}{Dt} - \frac{DP}{Dt} = \nabla.(k\nabla T) + \phi + Q^{\cdot}_{gen} \tag{I.3}$$

where,

$$\phi = \tau'_{ij}\frac{\partial u_i}{\partial x_j} = \nabla.\left(\tau'_{ij} - \vec{u}\right) - (\nabla.\tau'_{ij})\vec{u}$$

APPENDIX – II

Couple Modified Strongly Implicit Procedure (CMSIP)

The above block matrix [A] needs to be decomposed into upper and lower triangular matrices and to make this easier an auxiliary matrix [P] is added to both sides of the Eq. (5.13) which takes the form (where superscript k is the index for the number of iterations)

$$[A+P]\,x^{k+1} = b + [P]x^k \qquad \text{(II.1)}$$

Setting $\delta^{k+1} = x^{k+1} - x^k$ and $R^k = b - [A]x^k$ Eq. (II.1) becomes

$$[A+P]\,\delta^{k+1} = R^k \qquad \text{(II.2)}$$

Replacing the matrix [A+P] with the product of lower-block triangular matrix [L] and upper-block triangular matrix [U] in Eq. (II.2), one gets

$$[L][U]\,\delta^{k+1} = R^k \qquad \text{(II.3)}$$

Defining vector W by

$$W^{k+1} = [U]\delta^{k+1} \qquad \text{(II.4)}$$

the equation (II.4) can be written as

$$[L]\,W^{k+1} = R^k \qquad \text{(II.5)}$$

The solution procedure then is as follows [16]: Compute the vector W from Eq. (II.5) by forward substitution procedure and then compute the vector δ from Eq. (II.4) by backward substitution. This procedure is repeated for the calculation of the new residual vector R followed by direct calculation of W and δ until the solution vector x converges according to a convergence criterion.

Appendix – III

Run Matrix for the case study

<table>
<tr><th>Problem Setup</th><th colspan="5">Options</th></tr>
<tr><td rowspan="11">General</td><td rowspan="4">Mesh</td><td colspan="4">Scale</td></tr>
<tr><td colspan="4">Check</td></tr>
<tr><td colspan="4">Report Quality</td></tr>
<tr><td colspan="4">Display</td></tr>
<tr><td rowspan="6">Solver</td><td rowspan="2">Type</td><td colspan="3">Pressure-Based</td></tr>
<tr><td colspan="3">Density-Based</td></tr>
<tr><td rowspan="2">Velocity Formulation</td><td colspan="3">Absolute</td></tr>
<tr><td colspan="3">Relative</td></tr>
<tr><td rowspan="2">Time</td><td colspan="3">Steady</td></tr>
<tr><td colspan="3">Transient</td></tr>
<tr><td colspan="5">Gravity: uncheck</td></tr>
<tr><td rowspan="9">Models</td><td colspan="5">Multiphase: Off</td></tr>
<tr><td colspan="5">Energy: ON</td></tr>
<tr><td colspan="5">Viscous: Standard, k-e, Standard Wall Fn, Viscous Heating</td></tr>
<tr><td colspan="5">Radiation: Off</td></tr>
<tr><td colspan="5">Heat Exchanger: Off</td></tr>
<tr><td colspan="5">Species: Off</td></tr>
<tr><td colspan="5">Discrete Phase: Off</td></tr>
<tr><td colspan="5">Solidification & Melting: Off</td></tr>
<tr><td colspan="5">Acoustics: Off</td></tr>
<tr><td rowspan="2">Materials</td><td>Fluid</td><td colspan="4">Water</td></tr>
<tr><td colspan="5">Solid: Aluminum</td></tr>
<tr><td>Cell Zone Conditions</td><td>Working Fluid</td><td>Material name</td><td colspan="3">Air (Ideal Gas)</td></tr>
<tr><td rowspan="14">Boundary Conditions</td><td rowspan="14">Zone</td><td rowspan="9">Lid
Type: Wall</td><td>Wall Motion</td><td colspan="2">Moving Wall</td></tr>
<tr><td rowspan="2">Motion</td><td colspan="2">Absolute</td></tr>
<tr><td colspan="2">Translation</td></tr>
<tr><td>Speed (m/s)</td><td colspan="2">17.3205</td></tr>
<tr><td>Direction</td><td colspan="2">x = 1</td></tr>
<tr><td>Shear Condition</td><td colspan="2">No Slip</td></tr>
<tr><td rowspan="2">Wall Roughness</td><td colspan="2">Roughness Height (m) = 0</td></tr>
<tr><td colspan="2">Roughness Constant = 0.5</td></tr>
<tr><td colspan="3">Interior-Surface-Body</td></tr>
<tr><td rowspan="4">Walls
Type: Wall</td><td>Wall Motion</td><td colspan="2">Stationary wall</td></tr>
<tr><td>Shear Condition</td><td colspan="2">No Slip</td></tr>
<tr><td rowspan="2">Wall Roughness</td><td colspan="2">Roughness Height (m) = 0</td></tr>
<tr><td colspan="2">Roughness Constant = 0.5</td></tr>
</table>

Dynamic Mesh	Dynamic Mesh : check (Layering)		
Reference Values	Compute Form	Inner Fluid	
		Inlet	
		Interior-Inner Fluid	
		Outlet	
		Surface	
	Reference Values	All calculated with the boundary conditions provided.	
Solution			
Solution Methods	Pressure- Velocity Coupling	Scheme	SIMPLE
			SIMPLEC
			PISO
			Coupled
	Spatial Discretization	Gradient	Green-Gauss Cell Based
			Green-Gauss Node Based
			Least Squares Cell Based
		Pressure	Standard
			PRESTO!
			Linear
			Second Order
			Body Force Weighted
		Density	First Order Upwind
			Second Order Upwind
			QUICK
			Third-Order MUSCL
		Momentum	First Order Upwind
			Second Order Upwind
			Power Law
			QUICK
			Third-Order MUSCL
		Turbulent Kinetic Energy	First Order Upwind
			Second Order Upwind
			Power Law
			QUICK
			Third-Order MUSCL
		Turbulent Dissipation Rate	First Order Upwind
			Second Order Upwind
			Power Law
			QUICK
			Third-Order MUSCL

		Energy	First Order Upwind
			Second Order Upwind
			Power Law
			QUICK
			Third-Order MUSCL
Solution Control	Courant Number: 200		
	Explicit Relaxation Factors	Momentum: 0.75	
		Pressure: 0.75	
	Under Relaxation Factors	Density:1	
		Body Forces: 1	
		Turbulent Kinetic Energy: 1	
		Turbulent Dissipation Rate: 1	
		Turbulent Viscosity: 1	
		Energy: 1	
Monitors	Residuals, Statistics and Force Monitors	Residuals- Prints, Plots: 1e-15	
Solution Initializations	Compute form	All-Zones	
		Inlet	
		Outlet	
		Surface	
	Initial Values	Gauge Pressure(Pascal): 0 Other values for initial velocity, temperature are calculated according to the given boundary conditions.	
Calculation Activities	Auto save every iteration = 35		
Run Calculations	Check case Number if Iterations:20612 Calculate		

APPENDIX – IV

User-Defined Function for mesh motion technique

```
/*********************************************************
   Uniform node motion UDF in the 2D cartesion grid
   Model should be in the 1st quadrant(x,y positive axis)
   User input are,
         cell_division = ?????;
  cavity_depth_increment = ????;

*********************************************************/
#include "udf.h"   /*header file*/
#include "dynamesh_tools.h"

DEFINE_GRID_MOTION(Uniform_node,domain,dt,time,dtime)
 /* defines header file*/
 {
          Thread *tc = DT_THREAD((Dynamic_Thread *)dt);
/* defines Dynamic thread pointer*/

    cell_t c;
 /*defines cell index*/
    Node *v;
    int n;
/*defines integer for nodes */
    int cell_division = 28;
/*user input: Need to define cell division considered while meshing
*/
    real cavity_depth_increment = 0.8661684782608696;
/*user input: Need to define the cavity increment in depth*/
    real Y_increment;
 /*declaring a real variable*/
           /*It calculates the cell size y increment for every time step */
          Y_increment=(((cavity_depth_increment)/ cell_division)* dtime);
          /* set deforming flag on adjacent cell zone */
    SET_DEFORMING_THREAD_FLAG (tc);
if (time > 0.0002943 && time < 0.0005889)
{

          begin_c_loop(c, tc)
/*defines cell loop by using the defined thread */
    {

                    int i = 0;
```

```
 /*It initiate i as 0 for every cell loop increment*/

           c_node_loop(c, tc, n)
 /*defines node loop by using the defined thread for the cell c */
       {
         v = C_NODE(c, tc, n);
/*C_NODE gives global cartesion coordiante node position  */

         if (NODE_POS_NEED_UPDATE(v))
/*It updates the current node only if it has not been previously visited*/
            {


/* Set flag to indicate that the current node's         */
                                /* position has been updated, so that it will not be   */
                      /* updated during a future pass through the loop:      */
          NODE_POS_UPDATED(v);

                 i=i+1;                  /*i increment */

                if (c == 0
                    {
                       if (i==1 || i==2)
                         {
                           NODE_Y(v)= NODE_Y(v)-(Y_increment*(cell_division-1));

                         }
                      else
                        {

                           NODE_Y(v)= NODE_Y(v)-(Y_increment*cell_division);
                        }

                    }

                if (c%cell_division == 0 && c != 0)
                    {

                       if (i==1)
                         {

                           NODE_Y(v)= NODE_Y(v)-(Y_increment*(cell_division-1));
                         }
                      else
                        {
```

```
                                NODE_Y(v)= NODE_Y(v)-(Y_increment*cell_division);
                            }

                        }

                    if (c > 0 && c < (cell_division-1))
                        {

                                NODE_Y(v)= NODE_Y(v)-(Y_increment*(cell_division-
((c%cell_division)+1)));
                        }

                    if (c%cell_division != 0 && c != 0 && c > (cell_division-1))
                        {

                                NODE_Y(v)= NODE_Y(v)-(Y_increment*(cell_division-
((c%cell_division)+1)));

                        }

              }
          }
       Update_Cell_Metrics (c, tc);
     }

  end_c_loop (c, tc);

}
}
```

VITA

The author was born in the city of Jeddah, Saudi Arabia and passed his early school and college years in Hyderabad, India. He obtained his Bachelor's degree in Mechanical Engineering in 2014 from Jawaharlal Nehru Technological University. After graduation, he joined University of New Orleans in Fall 2014 to pursue a Master's degree in Mechanical Engineering.